Combined solid-state NMR, FT-IR and computational studies on layered and porous materials

Geo Paul,[a,b] Chiara Bisio,[a,b] Ilaria Braschi,[b,c] Maurizio Cossi,[a,b] Giorgio Gatti,[a,b] Enrica Gianotti,[a,b] Leonardo Marchese*[a,b]

[a]*Department of Science and Technological Innovation and* [b]*Centro Interdisciplinare Nano-SiSTeMI, Università del Piemonte Orientale, Viale T. Michel 11, 15121 Alessandria, Italy.*

[c]*Department of Agricultural and food Sciences, University of Bologna, Viale G. Fanin 44, 40127 Bologna, Italy.*

Graphical abstract and TOC

This review covers comprehensively the 2D layered and 3D porous materials that have been reported in the past 5 years where combined solid-state NMR, FT-IR and computational methods have been employed for their characterization.

Abstract

Understanding the structure-property relationship of solids is of utmost relevance for efficient chemical processes and technological applications in industries. This contribution reviews the concept of coupling three well-known characterization techniques (solid-state NMR, FT-IR and computational methods) for the study of solid state materials which possess 2D and 3D architectures and discusses the way it will benefit the scientific communities. It highlights the most fundamental and applied aspects of the proactive combined approach strategies to gather information at a molecular level. The integrated approach involving multiple spectroscopic and computational methods allows achieving an in-depth understanding of the surface, interfacial and confined space processes that are beneficial for the establishment of structure-properties relationships. The role of ssNMR/FT-IR spectroscopic properties of probe molecules in monitoring the strength and distribution of catalytic active sites and their accessibility at the porous/layered surface is discussed. Both experimental and theoretical aspects will be considered by reporting relevant examples. This review also identifies and discusses the progress, challenges and future prospects in the field of synthesis and applications of layered and porous solids.

1. Introduction

The rational design of 3D porous and 2D layered materials as well as the understanding of their structure-property relationship is of utmost relevance for efficient chemical process and technological applications. There has been a significant increase in their synthesis as well as applications and as a result there has been an increase in the scientific publications being done across chemistry, physics and materials science. In the past few years, we have witnessed an increase in the multi-technique approaches, which stimulate the collection of information on solids with growing structural and compositional complexity. Each approach offers distinct advantages and can provide different information about bulk and surface properties. Though the principles of combined approach for characterisation were in use long since, the application of solid-state NMR (ssNMR), FT-IR spectroscopy and modelling to investigate weaker interactions in porous matter has merely emerged recently. In this review, we provide an overview of the combined approach of using ssNMR and FT-IR spectroscopy together with computational methods to gather information at a molecular level for materials with 2D as well as 3D porous architectures. Finally, special attention will be given to the use of molecular probes to determine the strength, type, concentration, nature and the accessibility of active sites.[1–5]

The scope of this review is to cover comprehensively the 2D and 3D porous materials that have been reported in the past 5 years where a combined approach has been employed for their characterization. The physico-chemical characterization of porous or layered solids, for technological applications, is an integral aspect of the research and development process. A number of considerations need to be made when one selects the spectroscopic technique of choice for solid state characterization of porous/layered solids. Theoretically, each technique is based upon a unique phenomenon: FT-IR, infrared energy absorption; ssNMR, radiofrequency absorption while the sample is located in a magnetic field, etc. Because of the unique nature of each technique and the various objectives of solid state characterization, one technique may be better suited than another. It is also very important to understand the limitations of each technique. However, a complete and detailed theoretical discussion of each technique is beyond the scope of this review. Instead, the reader is referred to a number of publications outlining the theory[6–10] and general usage[11,12] as well as references cited therein.

First of all, the review will give a brief background to the advantages of coupling techniques and special emphasis will be given to show how the information obtained from one technique would complement that obtained from other techniques. After that, a section addressing the need to use probe molecules with different chemical nature to monitor the surface of porous/layered solids (i.e. polarity, catalytic active sites, pore size, etc.) will be discussed. Finally, two sections will give an overview of 2D layered materials and 3D porous materials. Properties of such materials depend on the nature of layered or porous architecture and the presence of active sites, which are finely characterized by the multi-technique approach reviewed in this work. It is unattractive and almost impossible to cite every article related to these topics, therefore, the authors have adopted a balanced approach in identifying and including only the most relevant scientific papers in this review. The acronyms used in this review are shortly described in a glossary found in the ESI.

2. Advantages of coupling techniques

Multi-techniques approach can allow collecting both structural and surface information of solids. Among the characterisation techniques, the huge advantage of ssNMR and FT-IR spectroscopy over other traditional solid-state techniques, such as diffraction, is that they can be applied not only to crystalline samples but also to amorphous, disordered or inhomogeneous systems. Therefore, NMR spectroscopy can be used, for instance, to measure atomic coordinates, lattice parameters, interatomic distances, occupancy of atomic positions, whereas FT-IR can be exploited to collect fundamental information on structural and surface features of solids. On the other hand, utmost information related to the interactions between organic and inorganic components as well as hybrid materials can also be easily acquired by ssNMR and FT-IR methods. Moreover, ssNMR can also give important information on molecular dynamics or transport properties of such types of solids.

Very often, single experimental data is not sufficient to solve the complexity related to solid-state systems. Several experimental tools are used to study porous solids, but they all are limited in their spatial and temporal resolution. Different philosophies exist behind the choice of an experimental approach that usually is associated with the time scale of spectroscopic processes (Fig. 1). Solid-state NMR is able to provide different spectral insights through the observation of multiple nuclei in the same sample. However, one is limited to the observation of events that are significantly slower than the resonance frequencies of nuclei in question. Nevertheless, using FT-IR spectroscopy one can observe processes that occur at frequencies of the order of 10^{13} and 10^{15} Hz at room temperature. Experimental ssNMR spectroscopy measures the time and ensemble averaged values of chemical shifts in such cases. However, FT-IR spectroscopy and molecular dynamics (MD) simulations are capable of yielding data on single molecule.

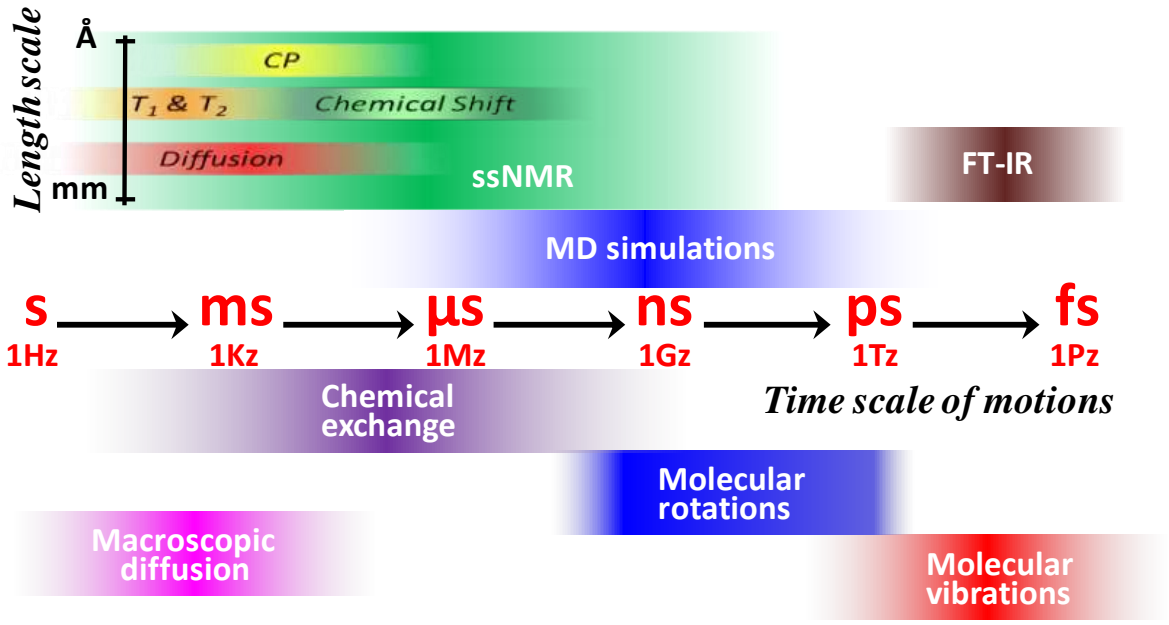

Fig. 1 Time scale of some fundamental molecular motions and different experimental approaches to probe them. Figure in part inspired and adapted from M. Levitt's webpage (http://www.southampton.ac.uk/~mhl/publications/books/SpinDynamics/SD1/index.html)

Solid-state NMR spectroscopy is largely used to give important information on structural properties of solids. For instance, naturally abundant aluminium is important in the study of porous solids and is a favourable nucleus for ssNMR study. The Al-O environments and coordination sphere in porous and layered solids can easily be determined from the ^{27}Al chemical shifts; 4, 5 and 6-coordinated aluminium resonances are well separated and are in the range 80 - 50, 40 - 30 and 15 - -10 ppm, respectively. ^{27}Al MAS NMR chemical shift scale of porous aluminosilicates, aluminophosphates (AlPO) and silicoaluminophosphates (SAPO) are given in Fig. 2.

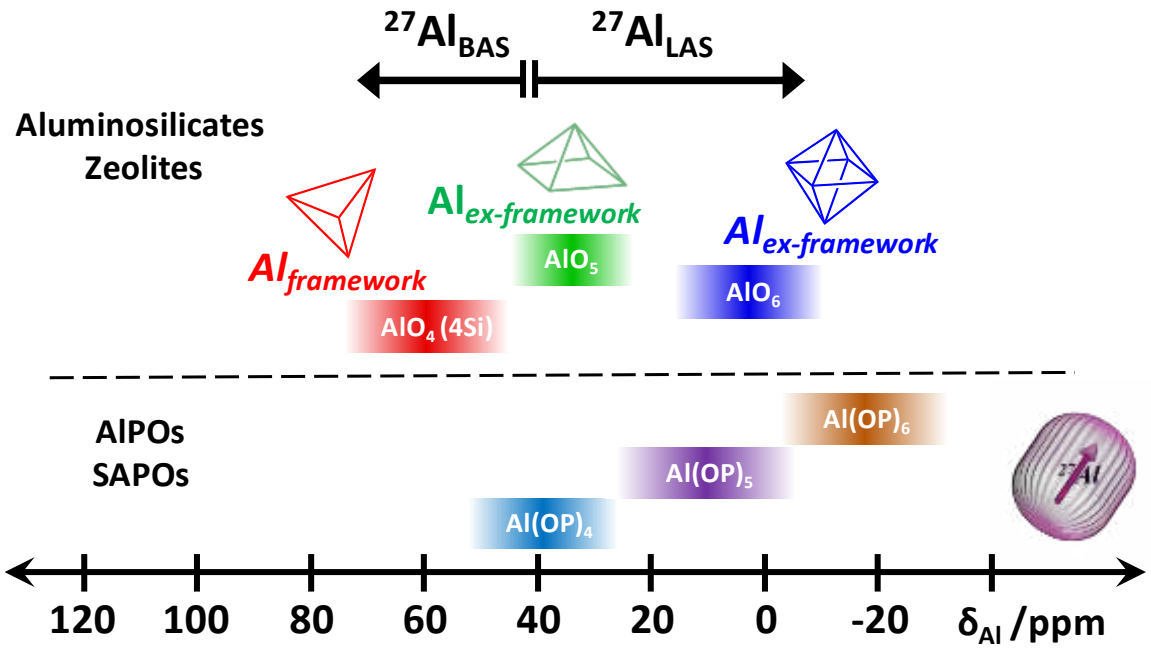

Fig. 2 ^{27}Al MAS NMR chemical shift scale of aluminium environments in selected porous solids. $^{27}Al_{BAS}$, aluminium at Brønsted acid site; $^{27}Al_{LAS}$, Lewis acidic aluminium site.

Another frequent example is the investigation of the isotropic chemical shifts of ^{29}Si sites that can give direct information about the structure, coordination and neighbour environments in porous and layered solids. In silicates and aluminosilicates, ^{29}Si chemical shift ranges associated with coordination and environments are well established (Fig. 3). Most information on silicates, aluminosilicates and silicoaluminophosphates can be obtained from ^{29}Si isotropic chemical shifts of tetrahedrally coordinated silicon atoms. Systematic changes in the chemical shift values are observed when the second coordination sphere (first being oxygens) is changed from Si to other atoms.[13] ^{29}Si MAS NMR chemical shift scale of selected silicon environments are shown in Fig. 3. As it can be derived from Fig. 3, from the analysis of ^{29}Si MAS NMR, information concerning structural species and surface OH groups of solid samples can be obtained.

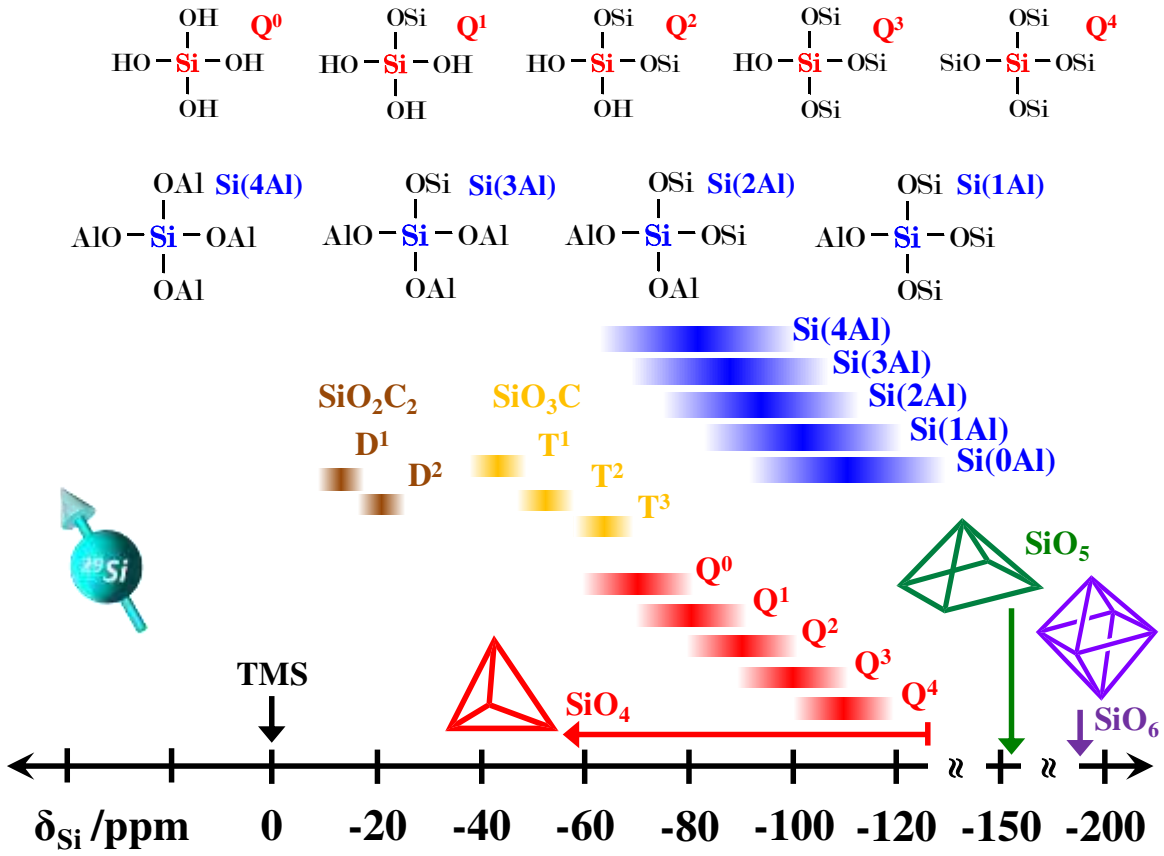

Fig. 3 ^{29}Si MAS NMR chemical shift scale of selected silicon environments.

In addition, ^{1}H MAS NMR chemical shifts can distinguish resonances due to acidic and non-acidic protons present in a porous solid. A chart showing the chemical shift scale of various protons that can be found in porous and layered solids is given in Fig. 4.

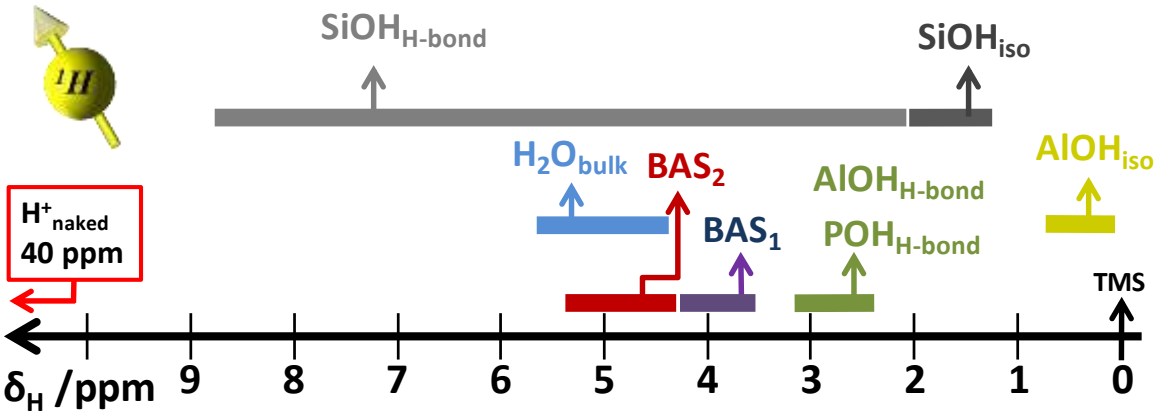

Fig. 4 ^{1}H MAS NMR chemical shift scale of various protons in porous solids. $AlOH_{iso}$, isolated aluminol; $SiOH_{iso}$, isolated silanol; $AlOH_{H\text{-}bond}$, hydrogen bonded aluminol; BAS_1, Brønsted acid site in large cavities; BAS_2, Brønsted acid site in confined environments; $SiOH_{H\text{-}bond}$, hydrogen bonded silanols.

FT-IR spectroscopy is also widely used to have information on solid samples: in the literature, there are an exceedingly high number of papers dealing with the use of this technique (and related methods such as Attenuated Total reflections, ATR and Diffuse Reflectance IR, DRIFT) to have information on hydroxyl groups and other surface species as well as to draw some considerations on the framework properties of materials. Nevertheless, FT-IR spectroscopy suffers from some limitations: for instance, the IR spectrum of the sample is "blind" with respect to the presence of ions with unsaturated coordination, which have a pivotal role in determining the catalytic properties of a solid and it cannot give complete information about the acidity of surface species (both hydroxyl groups, Brønsted or Lewis sites). Furthermore, no discrimination between bulk and surface species can be made. For this reason, most of the applications of FT-IR spectroscopy to study the surface properties of materials are linked to the use of probe molecules (*see Chapter 3*).

In Fig. 5, a schematic representation of frequency range scale of the most common IR signals that are used to study both the structure (typically the bands below 1000 cm^{-1}) and the surface species of solids are given.

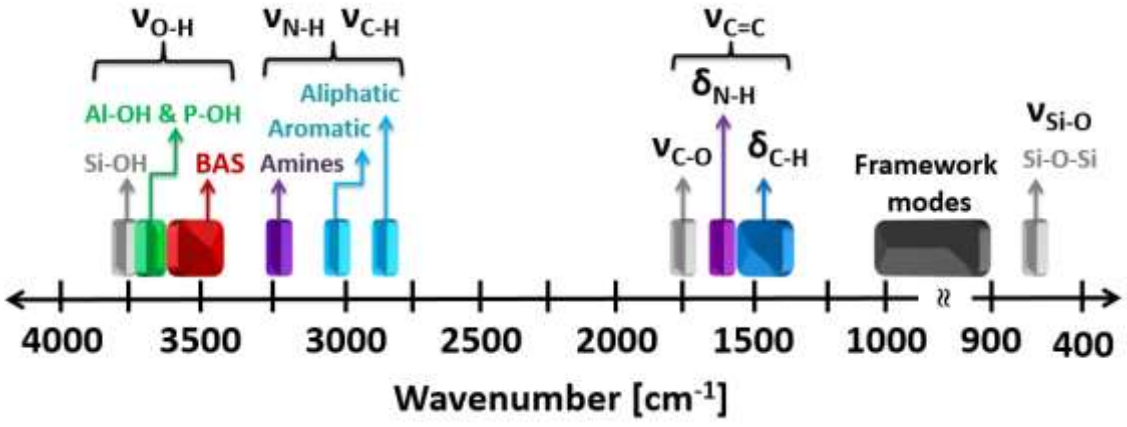

Fig. 5 FT-IR correlation chart reporting the most common IR signals typically used for the analysis of solid systems.

As a matter of fact, the combination of ^{1}H MAS NMR and FT-IR spectroscopy is essential in order to have a deeper insight in the evaluation of the nature of the surface protons in porous and layered materials. In this sense, a direct investigation of surface hydroxyls with different acidic strength in solids can be achieved by coupling FT-IR (also of adsorbed probe molecules, *see Chapter 3*) and ^{1}H ssNMR spectroscopy.

The concentration of protons (n_H) of a sample can be indeed estimated by using NMR data by using the following equation:

$$n_H = \frac{m^{ref}}{m}\frac{I}{I^{ref}}n_H^{ref}$$

where, m and m^{ref} denotes the masses of the sample and a standard reference (a solid with known concentration of acid sites (n_H^{ref})), respectively; whereas I and I^{ref} are the intensity (integral area) of the sample and reference signal, respectively.

There is an empirical and linear correlation between proton chemical shift $\delta_H(ppm)$ and stretching vibration of hydroxyl groups in solids:[14]

$$\delta_H(ppm) = 57.1 - 0.0147\nu_{OH}(cm^{-1})$$

However, for estimating hydrogen bonded protons, the following correlation should be adopted:

$$\delta_H(ppm) = 37.9 - 0.0092\nu_{OH}(cm^{-1})$$

It has to be noted that cationic hydroxyls will significantly deviate from these equations because NMR data are quantitative, whereas, stretching frequencies of IR absorption bands are dependent on the extinction coefficients of each species.

Similarly, the stretching vibration of bridging Si(OH)Al groups in aluminosilicates can be estimated from the δ_H measured at 298 K by using an empirically derived relationship, as expressed by[15]

$$\nu_{OH}(cm^{-1}) = 3906 - 74.5\,\delta_H(ppm)$$

In Scheme 1, ^{1}H MAS NMR and FT-IR spectra related to the OH groups of a silicoaluminophosphate material are reported.

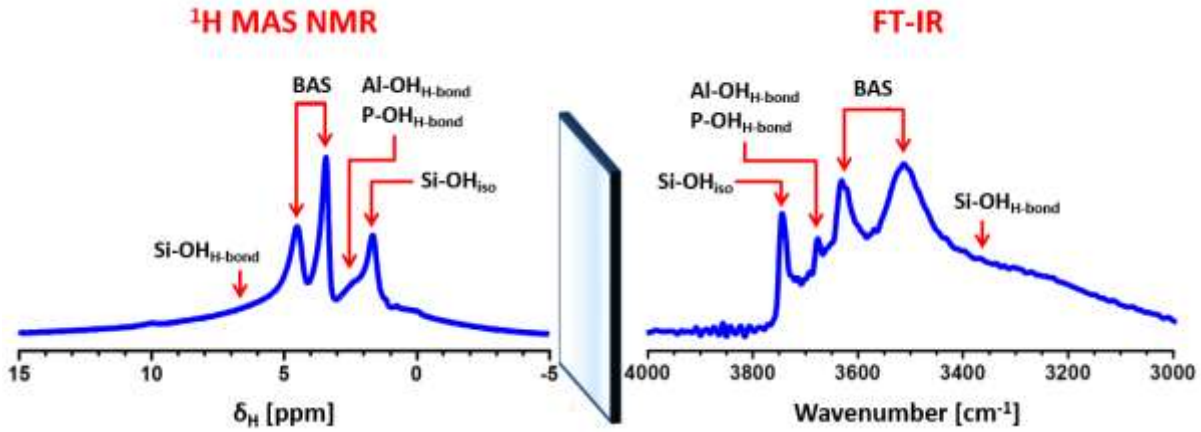

Scheme 1 An effective mirror image assembly between ^{1}H MAS NMR and FT-IR spectroscopy associated with the linear relationship of ^{1}H chemical shift and the frequency of OH stretching vibration as seen in a dehydrated zeo-type (SAPO) material. The assignments of most common isolated OH surface sites are highlighted: Si-OH$_{iso}$, isolated silanols; Si-OH$_{H\text{-}bond}$, hydrogen bonded silanols; BAS, Brønsted acid sites.

Owing to wide accessibility of general utility quantum chemistry programs, theoretical calculations of spectral parameters have provided an alternative, flexible, relatively easy, and sometimes more detailed approach, also aiding in the assignment of complex spectra. Molecular vibrations are computed in the harmonic approximation by numerous programs, either at *ab initio* or at semi-empirical level: almost all the codes providing geometry optimizations (Turbomole,[16] Gaussian,[17] Dalton,[18] ADF,[19] MOLPRO,[20] to cite some of the most used) also provide Hessian matrices and simulated vibrational spectra. In some cases anharmonic corrections are available as well,[21,22] though their high computational cost limits such applications severely; some codes provide vibrational frequencies at the DFT level also for periodic solids.[23]

There are many examples of studies combining IR or Raman (either absorbance or diffuse reflectance) spectra and theoretical simulations, often to support the assignment of peaks in difficult cases, or to model the intra- and inter-molecular interactions underlying the vibrational patterns. Some of these applications[24] are described in the following: an example of DFT and experimental vibrational spectra, compared to deduce the structure of different sulfonamide antibiotics embedded in a zeolite framework, is shown in Fig. 6.

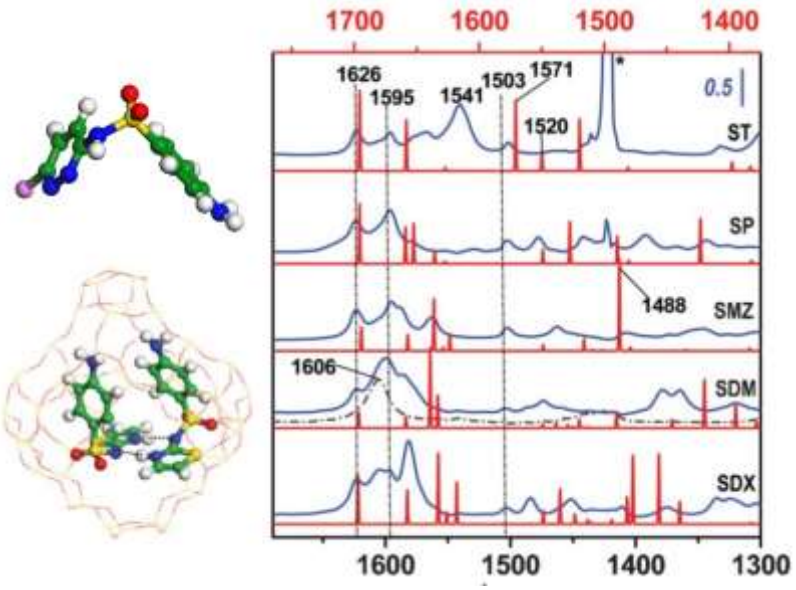

Fig. 6 Right side: Simulated (red) and experimental (blue) vibrational frequencies of some sulphonamide antibiotic molecules embedded in zeolite Y (examples shown on the left). Note the different scale due to harmonic approximation in the theoretical spectra. Left side: The optimized structure of sulfachloropyridazine (top) and sulfadiazine dimer embedded in the supercages of zeolite Y (bottom). Adapted with permission from ref. 24. Copyright 2013 The Royal Society of Chemistry.

Solid-state NMR calculation methods and modelling have kept pace with the rapid extension of experiments.[25,26] Calculation of NMR parameters, such as quadrupolar coupling constants, by WIEN codes has been in use for decades.[27] Similarly, SIMPSON, another authoritative program for fast and accurate numerical simulation of ssNMR experiments was described by Nielsen and coworkers.[28] Application of first-principles calculations using the gauge including projector augmented wave method (utilizing the framework of density functional theory) has revolutionized the ability to compute NMR tensors in periodic solid systems with all-electron accuracy.[29] The applications of this highly innovative approach in chemistry and materials science were recently reviewed by Bonhomme *et al.*[30]

3. Probe molecules

The adsorption of probe molecule allows a fine characterization of the surface nature of 2D and 3D porous solids: molecules with particular properties (*i.e.* acidic or basic) can interact with the surface active sites present inside the pores or between the layers.[31,32] By considering the electronic or geometrical distortion of the molecules induced by the adsorption, or eventually its chemical modification, it is possible to achieve information on the nature, location, accessibility and reactivity of the active sites. An ideal probe molecule should not cause any chemical modification of the surface and should occupy the same kind of sites during adsorption on different materials forming complexes stable enough to be characterised.[32] However, a proton transfer may occur between a solid acid and a basic probe molecule, and this process is also studied to get insights into the nature and concentration of catalytic acid sites as described below. Probe molecules may be classified according to their abilities to interact with acidic, basic or redox centres or, more generally, with surface defects (i.e. uncoordinated surface centers).[32]

FT-IR spectroscopy in the Mid-IR region (4200-400 cm^{-1}) allows monitoring the solid surface through the perturbation inferred to the probe molecules, that means changes in vibrational frequency and intensity of their IR modes. To be active in the IR range, a molecule has to change its dipole moment: molecules such as CO, NO, NH_3, CH_3CN are IR active. Nevertheless, IR inactive molecules, such as H_2 and N_2, can became IR active as a result of the interaction with the surface active sites. Some research groups have revised the use of probe molecules by FT-IR spectroscopy for 3D porous materials describing the most accurate methodologies to obtain information on physico–chemical properties of the active sites, as well as on their concentration and strength.[12,33,34]

The adsorption of probe molecules can be also followed by MAS NMR spectroscopy. Probe molecules with different basicity have been used, for instance, to study the acidity of solid catalysts with industrial relevance for the production of fine chemicals.[1] Three types of acid sites are in general recognized in heterogeneous catalysts, namely Brønsted, Lewis and silanols, which dictate the fate of a chemical reaction. In porous solid acids, bridging OH groups (Al-OH-Si) are considered the locus of Brønsted acid sites, which are able to donate the proton when interacting with strong basic molecule, while Lewis acid is only able to coordinate the probe.

The adsorption of weak bases are normally adopted to characterize Lewis and Brønsted acidity: upon interaction with an acidic OH group, these molecules form an H-bond adduct resulting in a downward shift of the O-H stretching modes. The magnitude of the shift is a measure of the acid strength of the hydroxyl group and is proportional to the proton affinity of the surface groups. The most frequently used probe molecules of this class are CO, N_2, O_2, and H_2 (normally adsorbed at temperature $\leq$ 100 K) along with acetonitrile, benzene, substituted benzenes, olefins (normally adsorbed at room temperature).[32] Strong bases such as ammonia and pyridine but also piperidine, trimethylamine and *n*-butylamine are also useful[35,36] When these molecules are adsorbed on Brønsted acid sites become protonated and display different spectroscopic features with respect the un-protonated probes. A list of the most common basic probe molecules suitable to study solid acids is reported in Table 1.

Table 1 List of selected probe molecules employed in FT-IR and ssNMR spectroscopic studies of the acidity and basicity of porous solids

PROBE MOLECULES [37] **BASIC**	**FT-IR** TYPE OF INTERACTION	**MAS NMR: METHODS AND COMMENTS**		**REFERENCES**
		BRØNSTED ACIDITY	***LEWIS ACIDITY***	
CO	H-bond with Brønsted & Lewis acid sites	^{1}H NMR acid concentration and strength	^{1}H NMR acid concentration and strength	12,32–34,38–42
CD_3CN	H-bond with Brønsted & Lewis acid sites	^{1}H NMR acid strength	^{1}H NMR acid strength	43–47
NH_3	Proton transfer with Brønsted acid sites	^{1}H NMR acid concentration and strength	^{1}H NMR acid concentration and strength	44,48–54
PYRIDINE & ALKILPYRIDINES	Proton transfer with Brønsted acid sites	^{1}H and ^{15}N NMR acid concentration and strength	^{15}N NMR acid concentration and strength	42,55–62
TRIMETHYL PHOSPHINE		^{31}P NMR acid concentration	^{31}P NMR acid concentration and strength	63–65
TRIALKYL PHOSPHINE OXIDE		^{31}P NMR acid location, concentration and strength	^{31}P NMR acid location and concentration	53,66–69
DIPHOSPHINES		^{31}P NMR acid location, concentration and strength	^{31}P NMR acid location and concentration	70,71
^{13}C-2-ACETONE		^{13}C NMR acid strength	^{13}C NMR acid strength	53,72–78
PERFLUOROTRIBUTYL AMINE		^{1}H NMR distinguish internal and external Brønsted acid sites		79,80

PROBE MOLECULES [81] **ACIDIC**	**METHODS AND COMMENTS**	**REFERENCES**
CO_2	**FT-IR**: Interaction with basic sites	12,82,83
PYRROLE	**FT-IR**: Intrinsic basicity; **^{1}H NMR**: intrinsic basicity	84–86
CHLORODIFLUOROMETHANE	**FT-IR**: Intrinsic basicity; **^{1}H and ^{13}C NMR**: intrinsic basicity	87,88
FLUOROFORM	**FT-IR**: Intrinsic basicity and strength	88,89
METHYLACETYLENE & TERT-BUTYLACETYLENE	**FT-IR**: Lewis basic sites and basicity strength	90
METHYL IODIDE	**^{13}C NMR**: base strength	91–93
TRICHLOROMETHANE TRIFLUOROMETHANE	**FT-IR**: Base strength; **^{1}H and ^{23}Na NMR**: intrinsic basicity	94
SO_2, SO_3, HCN, $CHCl_3$	**FT-IR**: Basic sites; **^{1}H, ^{13}C and ^{23}Na NMR**: intrinsic basicity	88,95–98

Fig. 7 shows a schematic representation of the different position of ^{1}H chemical shift (A) and the stretching and bending modes in FT-IR spectra (B) of *d*-acetonitrile, a weak basic molecule as well as ammonia and pyridine, strong bases (the classification is based on a massive number of results reported in the literature). The position of protonated species is also reported.

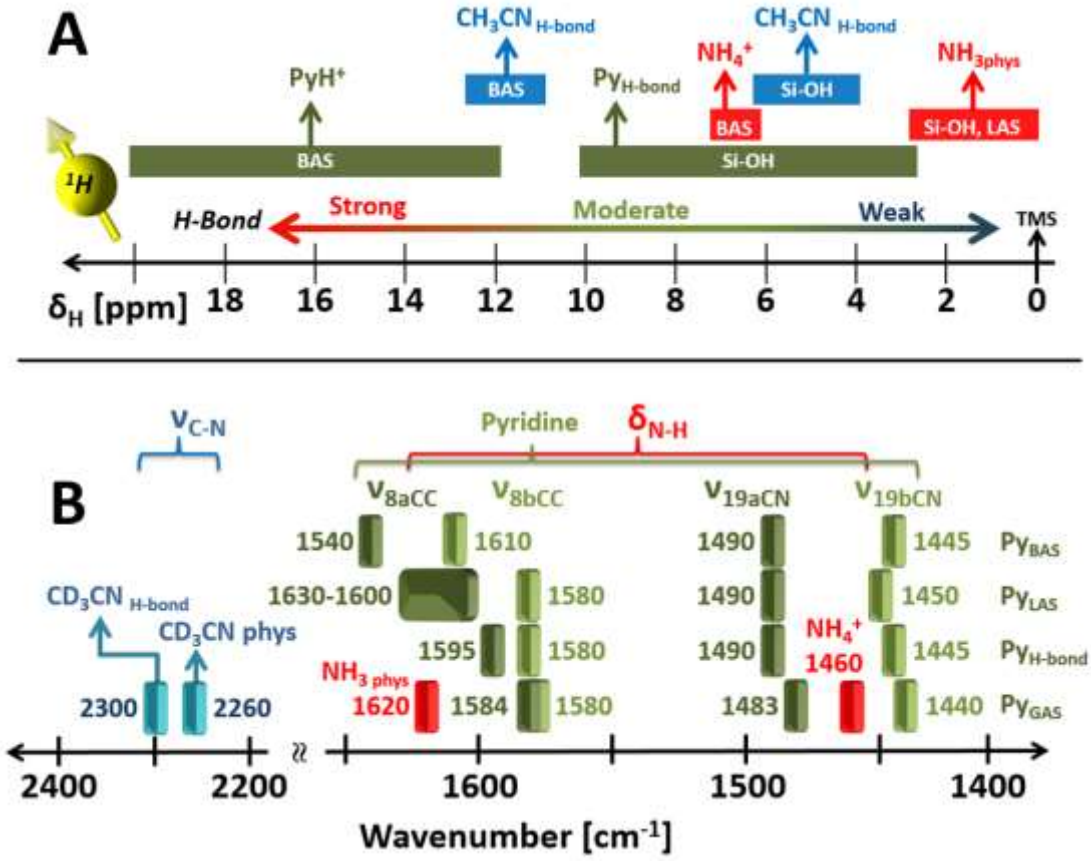

Fig. 7 Correlation chart related to selected probe molecules: A) ^{1}H MAS NMR chemical shift scale and B) FT-IR active frequencies. LAS, Lewis acid site; BAS, Brønsted acid site; H-bond, hydrogen bond.

FT-IR spectroscopy of adsorbed probe molecules also allowed the quantification of the total number of accessible Brønsted acid sites (N). It can be estimated using the Lambert–Beer law in the form $A = \varepsilon N \rho$, where A is the intensity of the specific IR band obtained after interaction with the probe molecule (*i.e.* pyridinium or ammonium ions), ε is the molar extinction coefficient (cm μmol^{-1}), N is the concentration of the vibrating species (mmol g^{-1}) and ρ is the density of the pellet (mass/area ratio expressed as mg cm^{-2}).

Besides solid acids, there is a strong interest in basic materials because of their interest in industrial catalysis.[85,89] The origin of materials basicity is very often associated with the negative charge density of the framework oxygen atoms, which further depends on the framework topology and chemical composition.[87] In the case of ion-exchanged zeolites, the framework negative charge can be for instance modulated by introducing different alkali-

metal cations thus leading to solids with variable basicity.[99] Spectroscopic studies of porous solids allow the determination of abundance and type of basic sites, which is mostly due to Lewis basicity, with the help of acidic probe molecules. A more comprehensive assessment of the basicity in zeolites could be given by ssNMR spectroscopy. Indeed, through identifying characteristic difference in the chemical shifts between before and after probe adsorption it is possible to follow the base strength of solid bases.[86] There are a variety of acidic probe molecules employed for these studies and few of them are listed in Table 1.[81]
As there are many magnetically active nuclei (^{1}H, ^{27}Al, ^{29}Si, ^{23}Na, ^{119}Sn etc.), may be present in a porous solid as well as in a probe molecule (^{1}H, ^{13}C, ^{15}N, and ^{31}P), ssNMR spectroscopy can be used as an ideal tool to study concentration, distribution, nature and strength of acid sites (Brønsted and Lewis). Alternatively, Lewis acidic sites can be directly detected by multinuclear (^{27}Al, ^{119}Sn and ^{47,49}Ti) NMR spectroscopy, which can distinguish between framework and extra-framework species.[100–102]Additional information on these specific applications is given in the ESI.

To monitor the adsorption of probe molecules on a surface, specific cells are needed; moreover, solid samples have to be outgassed in high vacuum conditions (and very often at high temperatures) in order to clean up the surface before the adsorption of molecules. Specific cells (very often designed, fabricated and home-made) are needed to study the adsorption of probe molecules by using both IR and ssNMR spectroscopy. An example is given in Fig. 8: a vacuum line is used to both clean up the sample surface and to uptake gases or vapours (in controlled doses) simultaneously on both the pellet used for IR measurement and the powder for ssNMR analysis. This allows the studies by FT-IR and ssNMR spectroscopy under strictly similar conditions, thus giving complementary insights on the surface sites and their interactions, which are otherwise not achievable.

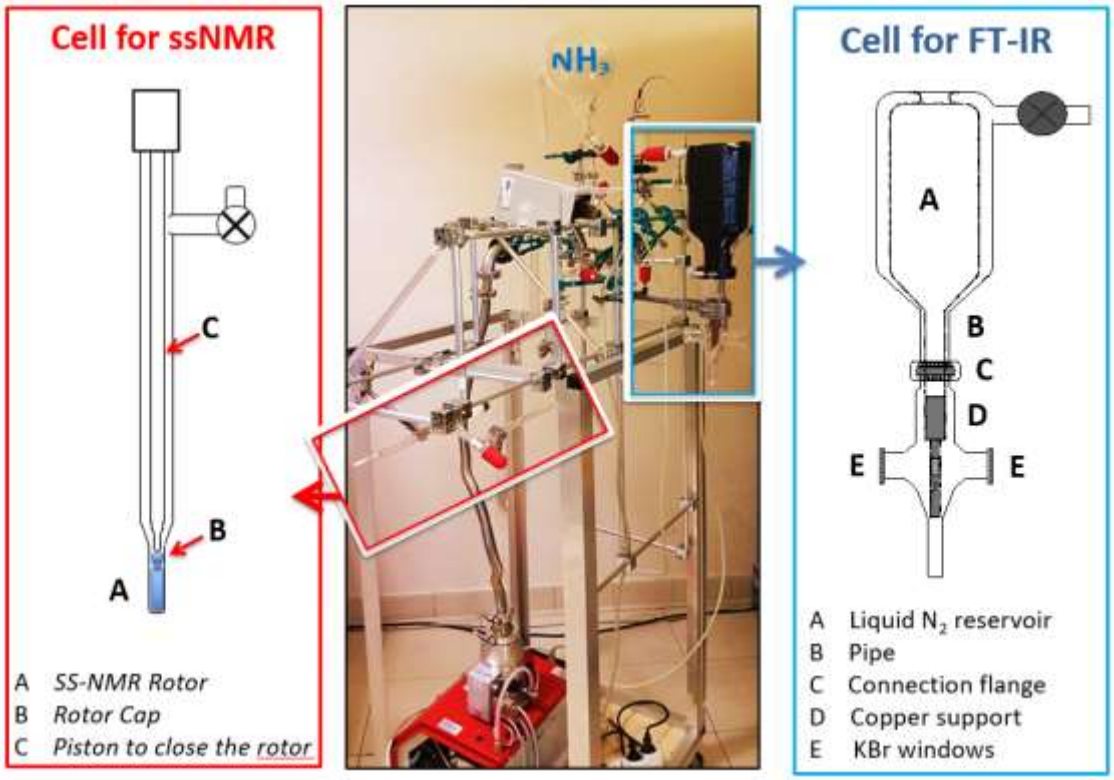

Fig. 8 Schematic view of the apparatus (vacuum line and cells) used for the simultaneous uptake of a probe molecule on samples that can be then studied (under similar conditions) by FT-IR and ssNMR spectroscopic techniques.

Deng *et al*., recently reviewed the application of combined approaches, in acquiring both qualitative and quantitative information on acidic sites using probe molecules, by employing ssNMR and DFT calculations.[103] DFT calculations can yield valuable information on the adsorption structure, deprotonation energy, and NMR parameters that can be correlated to the acid strength of solid acids. A recent review of Trujillo et al. describes the most applied spectroscopic and sorption based techniques in the investigation of acid property of porous solids.[40] The use of FT-IR spectroscopy for the characterization of layered and porous hierarchical materials has been reviewed by Roth *et al*.,[104] and some applications of *ab initio* calculations to support the experimental results have been mentioned.

4. 2D Layered materials

Among the vast class of advanced oxide materials, 2D layered solids have an important place because of their remarkable structure-properties relationships, which has been the subject of an increasing number of research papers and patents for different technological applications.[105]

Layered materials are formed by the packing of inorganic planar structures called layers or lamellae, interacting with each other through essentially weak bonds, typically of van der Waals (vdW) type, even if ionic interactions can be also found.[106] The strong chemical bonding in two rather than three crystallographic directions results in some of the interesting anisotropic properties of these compounds, like their mechanical strength, optical absorption, reflectivity, and the transport of electrons, holes and intercalated ions.

All along the years the layered materials have attracted an ever increasing attention as attested by the large number of published scientific papers, reviews and books. Many layered solids are from natural origin (for instance clay minerals) and have been good companions of the humanity through the ages having known the most widespread applications. Nevertheless, from few decades large attention was paid to synthetic layered materials especially for the possibility to tune their properties through a rational modification of the composition of the layers and/or interlayer space.[107–109] In relation to their controllable properties, this review is especially dedicated to synthetic solids.

The reversible inclusion of guest species (with variable chemical composition, from simple ions to complex organic moieties) in the layered host matrix (having either a crystalline or amorphous structure) leads to the so-called *intercalation compounds:* this is an interesting way to obtain new functional materials (not otherwise obtainable) in which the intercalated guests are accommodated, and in many cases protected from oxidation or photo-degradation. Since these materials very often do not fulfil the fixed stoichiometry required for a compound, the term hybrid is frequently used, especially when the guest species is an organic moiety.[110]

Intercalation compounds are a class of extremely flexible materials because the appropriate choice of host and guest species results in the possibility to tune their final properties, thus extending their potential applications to various technological fields such as heterogeneous catalysis, biomedicine, polymer science and environmental protection.[111–115]

The study of intercalation compounds started some ten years ago, and represents now an established specific domain of solid-state research and materials sciences. The knowledge of these solids have been largely widespread through the publication of several books, reviews and even through the organisation of specific meeting and conferences.[116–118] For instance, since 1977 the *International Symposium on Intercalation Compounds* (ISIC) is organised on biannual base, and the most recent advances were also collected in a themed issue of Dalton Transactions titled "*Recent developments in Intercalation Compounds: Chemistry and Applications*".[119]

In the frame of this Review, recent and significant examples attesting the importance of combining FT-IR, ssNMR and/or computational modelling techniques for the study of layered materials will be highlighted, with particular emphasis to solids that can be intercalated with different guest species. Our choice is based on the fact that the coupling of experimental and theoretical techniques is very often fundamental to give additional hints on intercalation phenomena and to the comprehension of structure/properties relationship of the derived materials.

Then, a survey on the combined use of techniques for the investigation of synthetic materials such as synthetic cationic clays, alkali layered silicates, phosphates/phosphonates and layered double hydroxides (Fig. 9) will be reported. Examples of perovskite-based solids will be also provided in relation to the increasing relevance that these materials have recently acquired in various fields such as optoelectronic or photocatalysis. It is relevant to note that hybrid organic-inorganic perovskites have recently acquired enormous interest for their outstanding performances in a new generation of photovoltaic devices.[120–123] Nevertheless, the solids used for this application have essentially 3D structure and they will not be treated in this section.

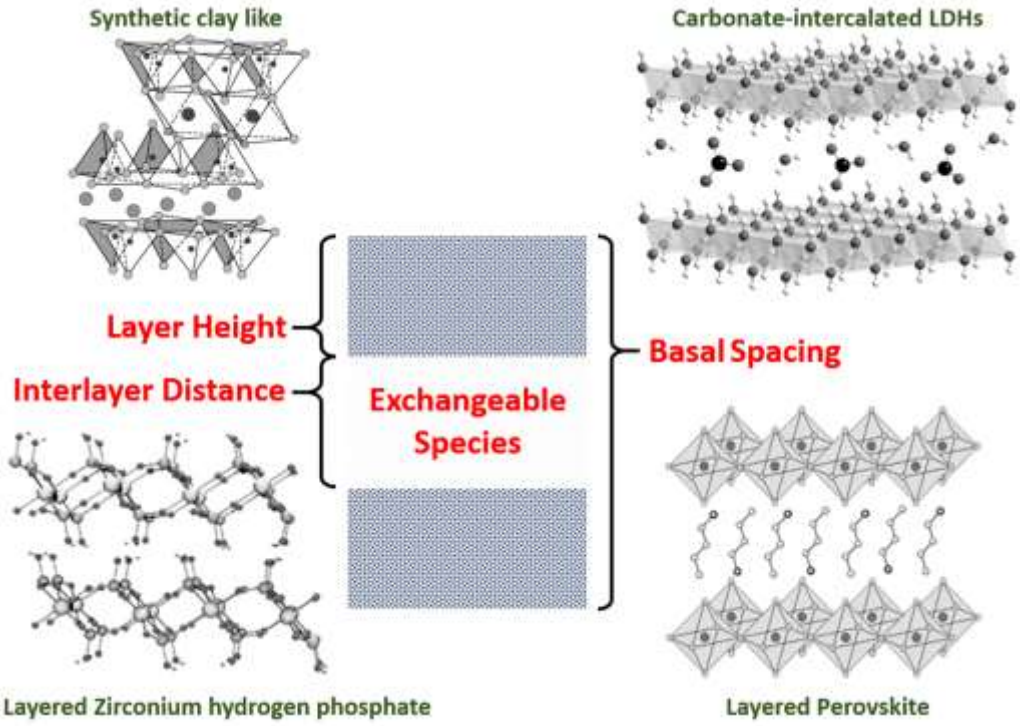

Fig. 9 Schematic view of the classes of synthetic layered materials treated in the review.

4.1. Synthetic clay-like materials

Clays of natural origin are largely available and very often inexpensive. Nevertheless, their chemical composition and physico-chemical properties are large variable depending on their site origin and this could limit their technological applications. In addition, the use of natural clays requires several extensive purification steps due to the presence of organic and/or inorganic impurities. For this reason, in this review the main attention is focused to the recent literature concerning synthetic clays with controlled and tuned properties.

Besides the classical uses as sorbents or ion exchangers, clays have been also employed as heterogeneous catalysts for fine chemicals production[124] or for the oxidative degradation of toxic molecules[125] and as additives for the preparation of polymer nanocomposites.[112,126] More recently, clays have also been used for optical and optoelectronic applications[127,128] or as additives for the stabilization of liquid electrolytes needed for the preparation of organic-based photovoltaic devices such as dye-sensitized solar cells.[129,130] An example of combined experimental study enlightening the influence of the adopted synthetic approaches, especially the effects of the dilution of the synthesis gel, on the physico-chemical properties of lamellar

solids is reported by our research group and is related to saponite clay of the smectite family.[131]This type of solid can be obtained by exploiting hydrothermal and microwave-assisted methods or sol-gel procedure (the latter method in general leads to poorly crystalline solids).[132]

The combination of FT-IR spectroscopy of adsorbed probe molecules (*i.e.* NH_3 at r.t. and CO at 100K) and ssNMR provided new insights on the coordination/distribution of aluminium in tetrahedral and octahedral sheets of the saponite in relation to the H_2O/Si ratio of synthesis gel. Besides an evident effect on the platelet dimension (Fig. 10, top), FT-IR data of NH_3 adsorption confirmed the presence of higher concentration of Brønsted acid sites in samples prepared with less diluted synthesis gel (as it can be seen from the intensity of the band at 1445 cm^{-1} due to ammonium ions, Fig. 10, bottom left), whereas the use of CO as a probe molecule allowed to make a scale of acidity of surface acid sites. Solid-state ^{27}Al NMR data involving 1D MAS (Fig. 10, bottom right) and 2D MQMAS, clearly demonstrated that the increase of synthesis gel dilution leads to a reduction of the Al^{IV}/Al^{VI} ratio, in agreement with the reduced cationic exchange capacity of these synthetic clays. It was thus inferred that a simple modification of the synthesis gel dilution resulted in the possibility to tune the acidity and ion exchange capacity of synthetic saponite samples.

Beside fully inorganic clays, in the last years large efforts have been devoted to the preparation of organic-inorganic hybrid materials, aiming to combine the advantages of organic functionalities and inorganic frameworks in solids for catalysis, drug delivery etc.[133,134] Organo-clays are generally prepared by post-synthesis ion-exchange intercalation of surfactant molecules.[135] However, other strategies have been recently explored to modify the surface of clay materials. Different hybrid organic-inorganic solids have been obtained, in fact, through one-pot synthesis by introducing organic alkoxides in the synthesis gel of phyllosilicates such as montmorillonite, saponite or laponite.[136,137]

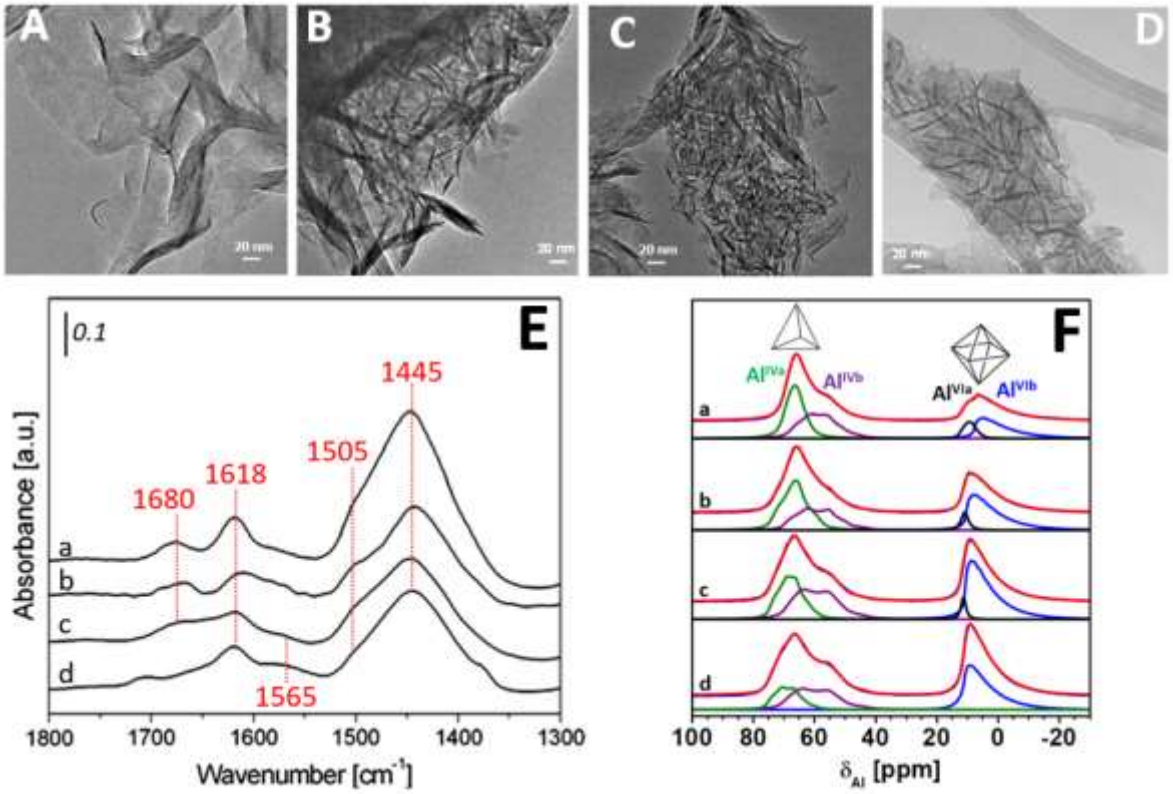

Fig. 10 top) TEM images of synthetic saponite samples prepared by using different H_2O/Si ratio (A: H_2O/Si=20, B=50, C=110, D=150); bottom left) FT-IR spectra, in the 1800–1300 cm^{-1} region, of NH_3 (100 mbar) adsorbed and subsequently evacuated at r.t. on saponites prepared using H_2O/Si ratio of (a) 20, (b) 50, (c) 110 and (d) 150 materials outgassed at 573 K; bottom right) ^{27}Al MAS NMR data recoded using a MAS rate of 15 kHz, each spectrum includes experimental and deconvoluted spectra with individual contributions from each ^{27}Al site. Adapted with permission from ref. 131. Copyright 2012 Elsevier Ltd.

Bisio et al. provided an example of the combination of ssNMR and FT-IR spectroscopy to give additional hints on the arrangement of cetyltrimethylammonium (CTA^+) cations intercalated in saponite clay.[111] An organo-saponite intercalated with CTA^+ (CTA-SAP_OP) was synthesized by one-step hydrothermal method and compared with an organo-saponite prepared by a classical post-synthesis exchange method (CTA-SAP_PS). FT-IR and ssNMR experiments demonstrated a different trans/gauche conformations ratio of the CTA^+ ions in the two hybrid clays. ^{27}Al and ^{29}Si MAS NMR experiments showed that the CTA-SAP_PS sample has higher concentration of tetrahedral aluminium than the CTA-SAP_OP. This means that the one-pot synthesis material has a lower charge density in the lamellae, which influences the surfactant organization in the saponite interlayer space.

As it can be seen in Fig. 11A, ^{13}C resonance peaks were considerably broadened and shifted in CTA-SAP_PS and CTA-SAP_OP compared to CTABr molecules and this suggests

conformational changes and distribution of environments for intercalated ions, together with a modification of mobility of the surfactant chains. The surfactant molecules in CTA-SAP_OP (Fig. 11A, curve c) predominantly adopted all-trans conformation, whereas CTA-SAP_PS (Fig. 11A, curve b) contained CTABr in both conformations in similar ratio. FT-IR data supported ssNMR ones, as it can be seen from the changes of the IR bands intensity in the hybrid systems (Fig. 1B) and this is a clear indication of the different organization of surfactant ions in the interlayer space of the two hybrids in relation to their preparation method.

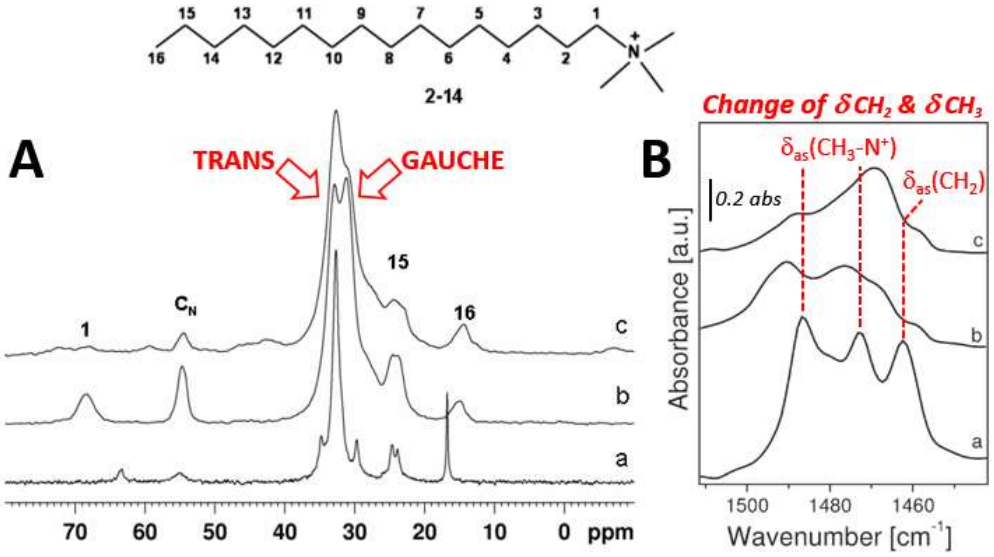

Fig. 11 (A) ^{13}C CPMAS NMR spectra of: pure CTABr (a), CTA-SAP_PS (b) and CTA-SAP_OP (c); (B) IR spectra of CTABr (a), CTA-SAP_PS (b) and CTA-SAP_OP (c) samples diluted in KBr. C_N denotes methyl carbons directly bound to nitrogen. Adapted with permission from ref. 111. Copyright 2011 American Chemical Society.

In 2011, Alba et al. reported a FT-IR and MAS NMR (both ^{29}Si and ^{13}C) spectroscopic study on the conformational (gauche to trans) changes of interlayer structure of mica intercalated with various *n*-alkylammonium cations ($R\text{-}NH_3^+$) with different alkyl chain lengths (R = C_{12}, C_{14}, C_{16}, and C_{18}).[138] The amount of intercalated surfactant and the *d*-spacing of the resulting solids increased with alkyl chain length, with the mica interlayer spaces expanding as needed to accommodate intercalated surfactants. The results indicated that the alkylammonium molecules packed tail-to-tail in a bimolecular arrangement, with the chain ends of two opposing molecules lying next to each other.

In 2016, Tao *et al.* proposed the sylilation of saponite clays to prepare organic-inorganic hybrid materials in which covalent links are present between the organic components and the surface. This enabled a durable immobilization of the organic species on the clay surface thus widening the possible uses of the derived materials.[139] In this study, saponite samples with fixed Si/Mg ratio were prepared by hydrothermal method and then grafted with 3-aminopropyltriethoxysilane (APTS). The sylilation mechanism of the clay mineral surfaces was described thanks to the coupling of FT-IR and ^{29}Si-NMR spectroscopy. In particular, FT-IR monitored the surface sylilation and the ^{29}Si MAS NMR clarified the occurrence of T^3 structures that increased with the silane content. T^1 structures were absent (these signals/sites *have been described in section 2*).

Expandable 2:1 clays are currently considered quite versatile materials for biomedical applications such as controlled drug release, gene delivery, and cancer therapy. In this context, dendrimeric-like assemblies based on organoclays were developed as multi-host systems for sustained drug delivery.[140] β-Cyclodextrin was modified by tosylation of its C6-hydroxyl groups whereas a synthetic Na-montmorillonite was grafted with 3-aminopropyltriethoxysilane to display amino groups. The two building blocks could covalently bind through a nucleophilic substitution reaction between the mono-6-(p-toluenesulfonyl)-6-deoxy-β-cyclodextrin and an amino group of the 3-aminopropyltriethoxysilane-functionalized montmorillonite. A combined IR and ^{1}H and ^{29}Si MAS NMR evaluation confirmed the occurrence of a nucleophilic substitution. From nano- to micro-scale dendrimeric supramolecular architecture structural features were observed owing to intermolecular H-bonding between the hydroxyl groups in β-cyclodextrin units and SiO_4 tetrahedrons oxygens of the montmorillonite surface. Several interesting biomedical features could be related to the dendrimeric structure of the organo-clay material (i.e. high drug loadings, prolonged low aggregation in cell-like media and low cytotoxicity), thus offering a promising approach toward the synthesis and the assembly of novel multifunctional materials with dendrimeric-like architecture.

The interlayer cations are of utmost importance to govern the sequence and route of reactions on the surface of the 2D expandable nanosheets during their assembly. The local state of sodium cations inside the interlayer spaces of synthetic saponite, hectorite and stevensite was systematically investigated by an experimental and simulated ^{23}Na MAS (MQMAS) NMR approach[141] and the tunability of the different interlayer cation states along with the local

structure of the 2D nanosheets was defined. Experimental and simulated NMR show two and three cation states in the stevensite and hectorite as a consequence of the different local electrostatic fields induced by the different charges of the corresponding octahedral layers.

An interesting example is related to the interaction of water with natural and organically modified montmorillonites.[142] Although natural clays are not included in the review, this study is described because of its relevance in showing the potential of combined IR and NMR spectroscopy The combination of the near-IR (9000–4000 cm^{-1}) together with ^{1}H and ^{13}C MAS NMR spectroscopy was adopted for a systematic study of water species adsorbed in a natural Na-montmorillonite exchanged with Li+ and two organic cations of different size (namely, tetramethylammonium - TMA - and hexadecyltrimethylammonium - HDTMA) exposed to different conditions of relative humidity at room temperature. According to the adsorption isotherms the amount of water decreased in order Li+ > TMA > HDTMA due to the increased hydrophobicity of the montmorillonite exchanged with organic cations. The intensities of the overtone (2ν) and combination (ν+δ) bands of H_2O vibrations, gradually increased in hydrated samples. The ^{13}C MAS NMR and near-IR of the hydrated organoclays confirmed the presence of water close to the head-group of the organic cations. Interestingly, NMR signals of inner -CH_2- groups in HDTMA were also affected by hydration and the contribution of disordered gauche conformers increased after water adsorption.

Few examples of combined theoretical/experimental studies appeared for the class of synthetic clays: *ab initio* (DFT) calculations with hybrid functionals, however, were used to help the interpretation of multinuclear ssNMR spectra in the characterization of montmorillonite[143] electron spin resonance (ESR) spectroscopy was applied to investigate polymer-clay nanocomposites,[144] and in this case DFT results provided insights on the weak coupling with various nuclei, notable ^{23}Na. On the other hand, a number of recent publications reported on the use of classical and *ab initio* molecular dynamics to support the structural determination of several clays with inelastic and quasi-elastic neutron scattering.[145–149]

Combination of DFT and IR spectroscopy have also been used to study a novel dielectric relaxation behavior under an applied alternating current electrical field originated from the dynamic orientation motion of ethanolamine or ethylene glycol intercalated into a montmorillonite ($Al_2Si_2O_5(OH)_4$·0.83ethanolamine and $Al_2Si_2O_5(OH)_4$·0.71ethylene glycol,

respectively).[150] IR analysis of the intercalated materials revealed that the characteristic and very sensitive IR active inner and inner-surface O–H stretching modes of the host were not significantly affected by the guests in full agreement with the DFT analysis of the single-crystal structures of the same materials. As a result, the intercalation expanded the kaolinite crystal along the c-axis, and did not significantly affect the atom arrangement within the aluminosilicate layer. These host-guest interactions were supposed to lead to the existence of a small energy barrier for the motion of ethanolamine or ethylene glycol from one orientation to another. The potential barrier associated to the thermal-assisted orientation alternation of the intercalated molecules could be overcome under an applied alternating current electrical field.

4.2. Alkali layered silicates

Aluminium-free layered hydrated silicates can be considered an extension of the groups of silicates and provide interesting alternatives to the different forms of silica. They are mainly prepared from common raw materials through hydrothermal processes. These materials have peculiar properties, including the possibility to be exchanged and intercalated, and applied *technological fields.*[151]

4.2.1. *Magadiite*

Magadiite is a member of the hydrous-layered alkali silicates that have attracted interest in relation to the possibility to easily modify their structure, texture and composition. In order to extend its use to thin film technologies and preparation of polymer nanocomposites many studies have been focused to the modification of the orientation and organization of the lamellae or by controlling the particle morphology (also through the disaggregation of the Magadiite particles).

In 2013, Pastore *et al*. reported an example of the preparation and characterization of Magadiite exchanged with cetyltrimethylammonium cations (CTA-Magadiite), and its disaggregation in separated plaques through ion-exchange in acidic media.[152] In this case, the combination of variable temperature IR and ssNMR spectroscopies provided additional hints to the comprehension of disaggregation process and enlightened the physico-chemical

properties of the produced materials. A comparison of the IR spectra of disaggregated Magadiite and of the parent CTA-Magadiite after evacuation at different temperature (*i.e.* 373 K and 573 K; Fig. 12A) enlightens the different nature of both intercalated and surface species of the two materials.

Indeed, the IR spectra at 373 K clearly shows that the disaggregation process leads to an almost complete removal of organic species (because of the negligible presence of the bands in the 3000-2800 and 1500-1450 cm^{-1} ranges), and to the formation of surface Si-OH species (broad and intense band at 3220 cm^{-1}). Moreover, the concentration of silanols is much lower in the CTA-Magadiite sample. After heating at higher temperature, the concentration of silanols becomes similar to that of the disaggregated Magadiite, though the distribution of species is different in the two materials as testified by the different shape and wavenumber of the band in the 3700-3000 cm^{-1} range. At this temperature a high concentration of silanols is present inside the Magadiite interlayer space and likely on the external surface of the silica particles. The coupling with ^{1}H ssNMR spectroscopy helped to clarify the nature of the surface species (schemes in Fig. 12).

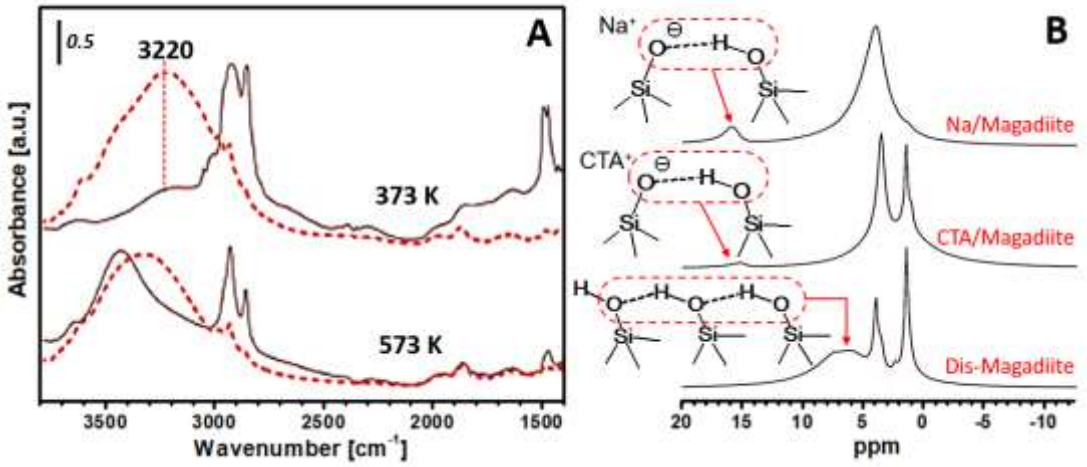

Fig. 12 A) IR spectra of CTA-Magadiite (solid line) and disaggregated Magadiite (dashed line) sample after outgassing at 373 and 573 K. B) ^{1}H MAS NMR spectra of Na-Magadiite, CTA-Magadiite and disaggregated Magadiite. Adapted with permission from ref. 152. Copyright 2013 The Royal Society of Chemistry.

In addition, the combination of 2D ^{1}H–^{29}Si HETCOR NMR with FT-IR spectroscopy provided a deeper insight on the nature of the surface/interface of inorganic–organic hybrid CTA-exchanged samples, along with that of the derived disaggregated material. 2D HETCOR NMR experiments, with different contact times, indicated that the samples have

distinct structural conformations and dynamics at the interface. These results, combined with those derived by variable temperature XRD and FT-IR, led to clarify that by thermal heating the CTA degradation influences the disaggregation of the structure with an increase of surface area. A condensation of silanol groups occurred during the disaggregation, with the formation of specific siloxane interlayer linkages. Moreover, disaggregated Magadiite shows a much higher concentration of H-bonded silanols nest typical of amorphous silica samples or highly defective silicalite[153] (Scheme 2).

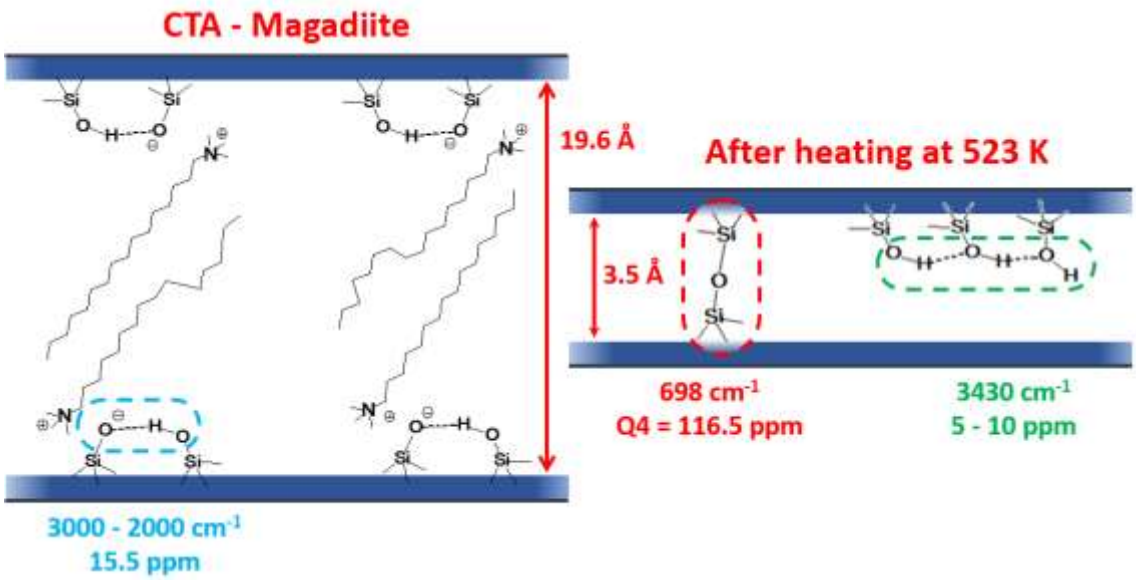

Scheme 2 Representation of the evolution of interlayer species after heating of CTA-Magadiite based on results coming from the coupling of variable temperature IR and XRD analyses and ssNMR spectroscopy. Adapted with permission from ref. 152. Copyright 2013 The Royal Society of Chemistry.

4.2.2. Na-RUB-18

The hydration-dependent structural changes of the layered silicate Na-RUB-18 ($Na_8Si_{32}O_{64}(OH)_8*32H_2O$)[154] were also studied by a combination of experimental (TG, XRPD, IR) and theoretical (semi-empirical and ab initio periodic calculations) techniques.[155] Such combined approach was particularly useful to describe the evolution of the Na-RUB-18 local structure as a function of the temperature and hydration degree.

A theoretical model of the hydrated, as-synthesized Na-RUB-18, optimized by DFT with periodic boundary conditions showed that two water molecules in each solvation shell (in apical position) are less strongly bound, and they are likely to be lost in the first de-hydration.

The coupling of modelling with variable temperature IR analysis gave more insights about the changes induced by the de-hydration (Fig. 13). The spectrum of the hydrated form reveals water molecules engaged in H-bonds of different strength as testified by the complex band in the 3700-3000 cm^{-1} band (Fig. 13, a), thus confirming the difference between apical and equatorial positions, while in the partially de-hydrated form the H-bonds appear stronger, in agreement with the structure optimized theoretically.

An important point concerns the nature of the H-bond between silanol and silanolate groups on the layer surface, which has been debated in the literature that is more evident upon heating at 100 °C (Fig. 13, curve d). The IR spectra analysis shows that the stretching of this H-bond is associated to a large feature in the 3200-1300 cm^{-1} range, showing Fermi resonance phenomena with the overtones (and/or combinations) of the bending modes of the same group. These frequencies are reproduced by ab initio calculations to reproduce the chemical environments of the silanol-silanolate bridge in the hydrated and de-hydrated forms. Experimental and theoretical findings agree in indicating a strong H-bond in the silanol-silanolate bridge, rather than shared hydrogen in a single-wall potential.

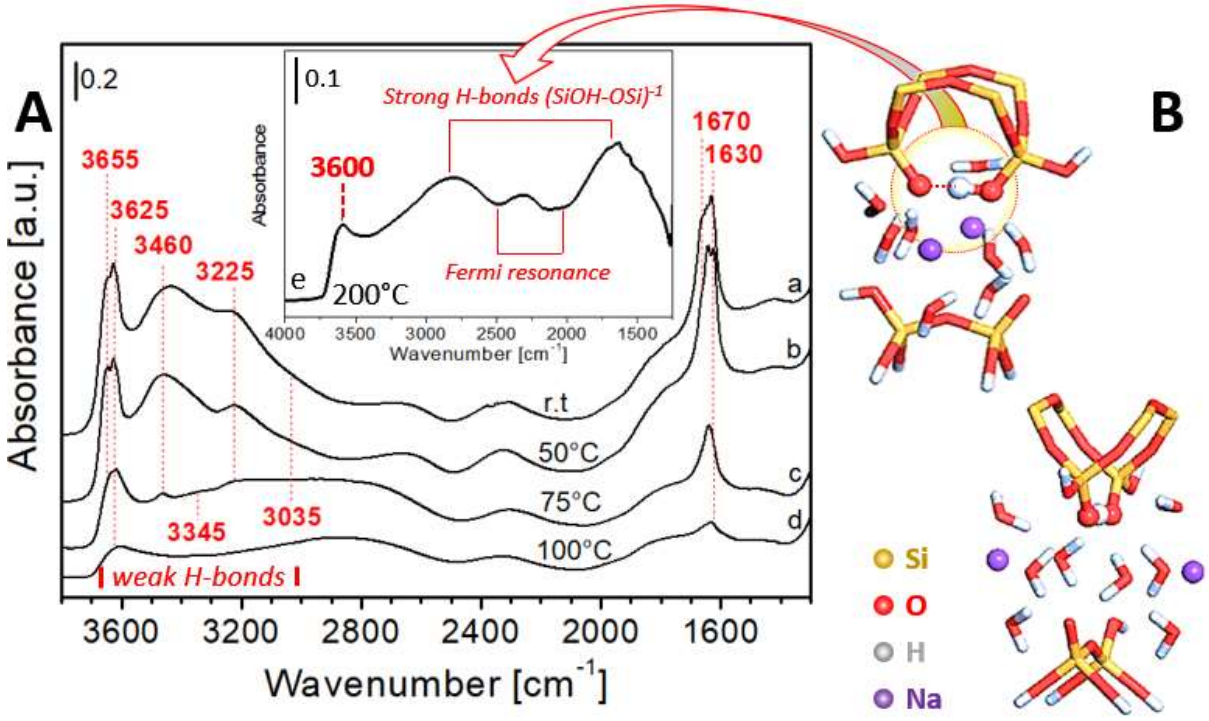

Fig. 13 A) Variable Temperature FT-IR spectra of Na-RUB-18 samples; B) $Na_2Si_8O_{16}H_7(OH)\cdot 8H_2O$ cluster used to model the silanol bridge in the hydrated structure. Adapted with permission from ref. 155. Copyright 2009 The Royal Society of Chemistry.

4.2.3. Kanemite

Kanemite, a framework of only tetrahedral $Si(Al)O_4$ units with both Si/Al-OH groups and hydrated alkali metals at the interlayer, deserves a special attention because of its ability to form ordered mesoporous silicas. Inorganic–organic nanostructures, used as mesostructured material precursors, can be constructed by the interlayer modification of inorganic layered materials with surfactants. In this context, the adsorption conditions of octadecyltrimethylammonium (ODTMA) in Kanemite were found to contribute to the design of novel layered materials with potential environmental and technological use.[156] In this study, the long and short range structural orders of Kanemite intercalated with ODTMA ions at interlayer under different conditions (i.e., different temperatures and clay: HDMA ratio, pH adjustment with HCl or HF) was investigated by a combined IR and multinuclear ssNMR investigations. An ordered lamellar structure was always obtained for all the hybrid mesophases whereas different all-trans and trans–gauche conformations were revealed for the adsorbed ODTMA at the specific loading conditions. The ODTMA adsorption decreased the water content at the interlayer space in Kanemite and induced changes in the silicate framework. When the adsorption was carried out in HCl or HF medium, it provoked a disruption of the intralayer H--O--H bridges accompanied by the formation of SiO_4 Q4 environments and five-member rings as revealed by FT-IR and ^{29}SiMAS NMR observations.

4.3. Layered phosphates and phosphonates

Smectite-type layered phosphates, phosphonates and phosphites received large attention in the past decades due to their potential applications in various domains such as catalysis, biological applications, biosensors etc.[151]

In particular, the structure of a-Zirconium phosphate, $Zr(O_3POH)_2 \cdot H_2O$, consists of planes of Zr(IV) atoms linked by phosphate groups above and below the plane, in a two-dimensional network.[157]

The three-dimensional structure is resulting from the two-dimensional layers stacking upon one another formed by hydrogen-bondings between the phosphate hydroxyl groups and the intercalated water molecules. Alberti *et al.*[158] and Dines and Di Giacomo[159] discovered a related family of compounds known as zirconium phosphonates, $Zr(O_3PR)_2$, which also possess a layered structure similar to that of zirconium phosphate, and that can be synthesized

using phosphonic acids instead of phosphoric acid. In these materials, it is now the attractive interactions of the organic (R) groups that project into the interlayer region that is responsible for stacking the zirconium planes. Zirconium phosph(on)ates are considered promising materials with applications that span from catalysis[160] to ion exchange[161,162] and photophysics.[163] Several reviews and books dealing with zirconium phosph(on)ates appeared in the literature.[164,165] However, few examples of the combination of experimental techniques and/or modelling aiming to determine the structure of these particular compounds have been given in the literature.

For instance, Casciola *et al*. used a combination of FT-IR and photoacoustic spectroscopies (FTIR-PAS) and ^{31}P ssNMR to study zirconium sulfophenylenphosphonates (SPP), with layered structure of the a-type and variable concentration of sulfonic groups, obtained by direct precipitation in the presence of HF. From the characterization they indicated that the solids have a layered structure built up by the packing of symmetric a-layers where SPP and HPO_4 groups are uniformly distributed on both layer faces.[166]

Clearfield *et al.* obtained α-zirconium phosphate organically surface-modified through the reaction of surface P−O−H groups of α-zirconium phosphate nanoparticles (α-ZrP) with octadecyltrichlorosilane (OTS) using a one-step synthesis. The formation of P−O−Si bonds arising from nucleophilic attack of POH to the silane was confirmed by ssNMR experiments whereas the surface coverage of the organic modifier was characterized by TGA, AFM, and FT-IR methods.[167]

Zhang recently reported a combined study of both experimental and modelling techniques.[168] Novel ZrPP-anchored heterogeneous methyltrioxorhenium (MTO) catalysts were prepared by a conventional impregnation method and several characterization techniques such as XRD, FT-IR, ICP-ES, HRTEM, XPS, and ^{1}H MAS NMR, as well as DFT calculations were employed to understand the structure feature of the obtained MTO/ZrPP catalyst. It was indicated that MTO is anchored on support surface by the favoured hydrogen-bondings between two oxo ligands of MTO and two H atoms from the adjacent phenyls of ZrPP.

A general recipe to decompose the NMR Fermi contact shifts of a number of oxides and phosphates, based on DFT calculations with hybrid density functionals, was proposed and the potential applications were described for several layered electrodes in Li batteries.[169] Electric field gradient (EFG) tensors computed at the ab initio level have been used to support the

interpretation of Na, Mg and Zr NMR spectra;[170–173] Marfa *et al.* described the structural characterization of a titanium phosphate with organic templating agents with a wealth of experimental techniques,[174] including X-ray diffraction, multinuclear MAS NMR and FT-IR spectroscopies, and showed how DFT calculations could be used for the assignment of NMR resonances (especially of ^{1}H spectra); in the same work the theoretical calculations provided information about the strength of H-bonding in phosphate moieties.

Theoretical IR spectra, obtained with 3D and 2D boundary conditions, were compared to experimental FT-IR results on a layered aluminophosphate (ALPO) intercalated with *n*-butylammonium ions, to support the assignment and the interpretation of the experimental peaks, also revealing the presence of Fermi resonances: also in this case, the comparison was used to estimate the interactions between the phosphate and the organic layers (Fig. 14).[175]

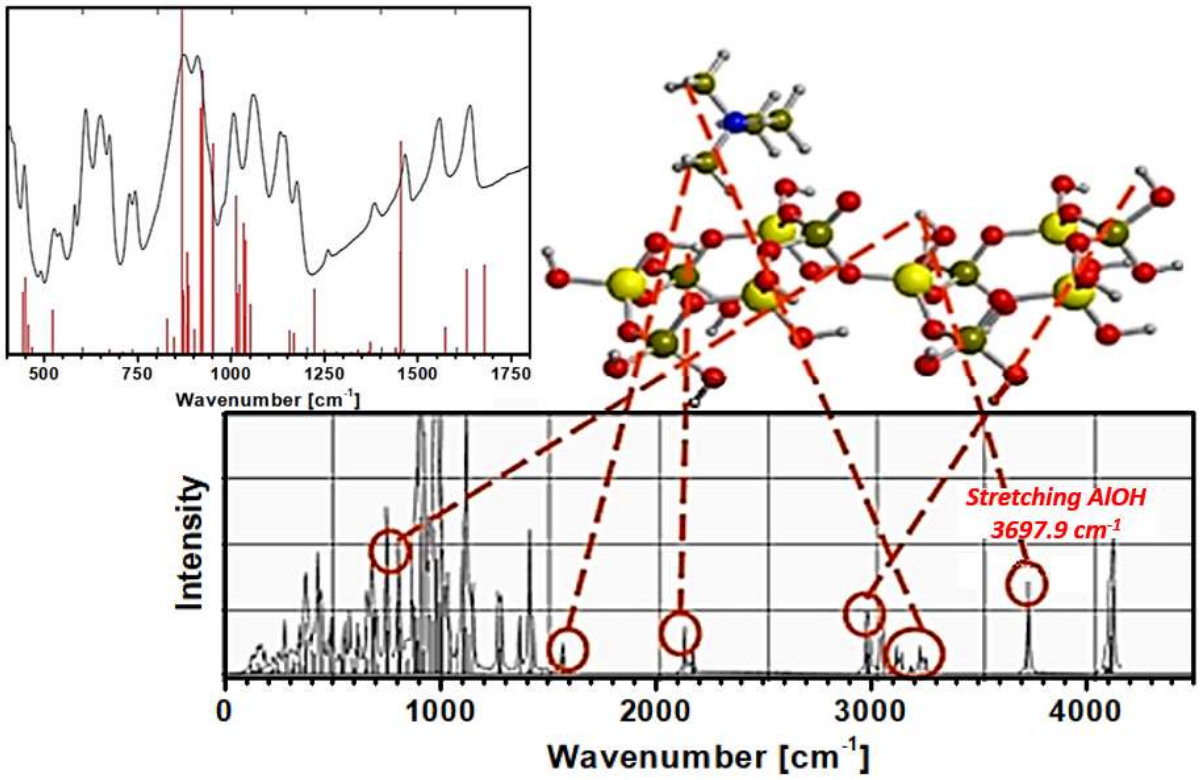

Fig. 14 Top: comparison of experimental (black) and DFT (red, 80 cm^{-1} shifted for anharmonicity) vibrational spectra of AlPO-butylammonium; Bottom: theoretical assignment of the main peaks in the simulated spectrum. Adapted with permission from ref. 175. Copyright 2008 American Chemical Society.

4.4. Layered double hydroxides

Layered double hydroxides (LDHs), also known as hydrotalcite-like materials, are anionic exchanging clays consisting of metal hydroxides layer and anions intercalated into hydrated interlayer for supplying the balancing negative charge.[151,176,177] The nanostructured character of LDHs, their temperature-induced transformations into metastable oxide materials and their ability to reconstruct the LDH state through the action of humidity or water lead to widespread their applications in many technological areas ranging from catalysis to polymer science or drug delivery.[178–181] They can be represented by the ideal formula $[M^{2+}_{1-x}M^{3+}_{x}(OH)_{2x}]^{x+}A^{n-}_{x/n}\cdot mH_2O$, where M^{2+} and M^{3+} are divalent and trivalent metal cations (i.e. Mg^{2+}, Al^{3+}) respectively, and A^{n-} is an exchangeable anion, such as CO_3^{2-}, SO_4^{2-}, and NO_3^-.[182]

Unlike most cationic clay materials, an important feature of LDH is that the layered charge density and the chemical composition can be tuned over a wide range during synthesis with an associated fine control of the properties of LDH-based materials. The synthesis and chemical modification of LDHs offer attractive research opportunities, mostly due to their good environmental stability and simple intercalation/deintercalation chemistry. In this context, the combination of spectroscopic and computational techniques is fundamental to evaluate the host-guest interactions and to calculate the geometric and electronic structures of the LDH intercalated with guest species.[183–185]

The structure of LDHs, although simpler than that of other layered materials such as natural cationic clays, has been largely studied in relation to: (i) charge distribution within the brucitic layer and their local order/disorder at short or long range; (ii) influence of the cation size for maintaining a hydrotalcite-like structure; (iii) order/disorder degree of the anions into the interlayer region and interactions with the brucitic layer; (iv) influence of the interlayer water content on the reactivity; (v) layer stacking and (vi) microstructural defects due to stacking faults and turbostratic disorder. A large number of experimental methods with computational techniques have been very often used to clarify the above-mentioned points. Several examples of these case studies have been recently reviewed from Nocchetti *et al.*[106]

4.4.1. Structural information on LDHs

A recent review collected many convenient synthetic routes for hydrotalcites and presented some examples of joint theoretical and experimental characterization techniques, based on X-ray and electron diffraction for the structural determination.[186]

In 2016, Nielsen *et al*. studied the insertion of Zn in the bayerite layer and fully characterise the obtained series of Zn-Al_4 LDHs with a multidisciplinary approach.[187] In particular, ^{1}H and ^{27}Al ssNMR, IR, and Raman spectroscopy were applied to have a detailed insight into the structure and composition. Four different structural models were assessed using the experimental techniques in combination with first-principles calculations of the ssNMR parameters. The obtained data indicated that the combined experimental and theoretical approach is beneficial to optimise the synthesis conditions of materials thus helping in determining the best procedure for pure phase preparation.

An example of the use of the Raman and IR spectroscopy together with modelling methods was given on nitrate-based layered double hydroxides, $Mg_{1-x}Al_x(OH)_2(NO_3)_x \cdot mH_2O$.[188] Stability towards humidity, dehydration, nitrate group orientation, Al migration and crystal structure were studied. The coupling of vibrational spectroscopies (both IR and Raman) together with modelling methods was employed in this case to have additional insights on the properties of interlayer space, surface species and layers structure. The atomic positions of all the structure models, also in the presence of NO_3^- and H_2O (Fig. 15), were optimized by using DFT-based methods. Starting from these models, the IR spectra were simulated for samples with different chemical compositions and compared with the experimental ones (Fig. 15). The study provided information on the orientation of anions and water molecules in the interlayer space, thus confirming that the combination of experimental and theoretical tools are relevant to understand the interlayer chemistry, and can easily be extended to fully dehydrated systems, more complex anions, and magnetic LDHs among other systems.

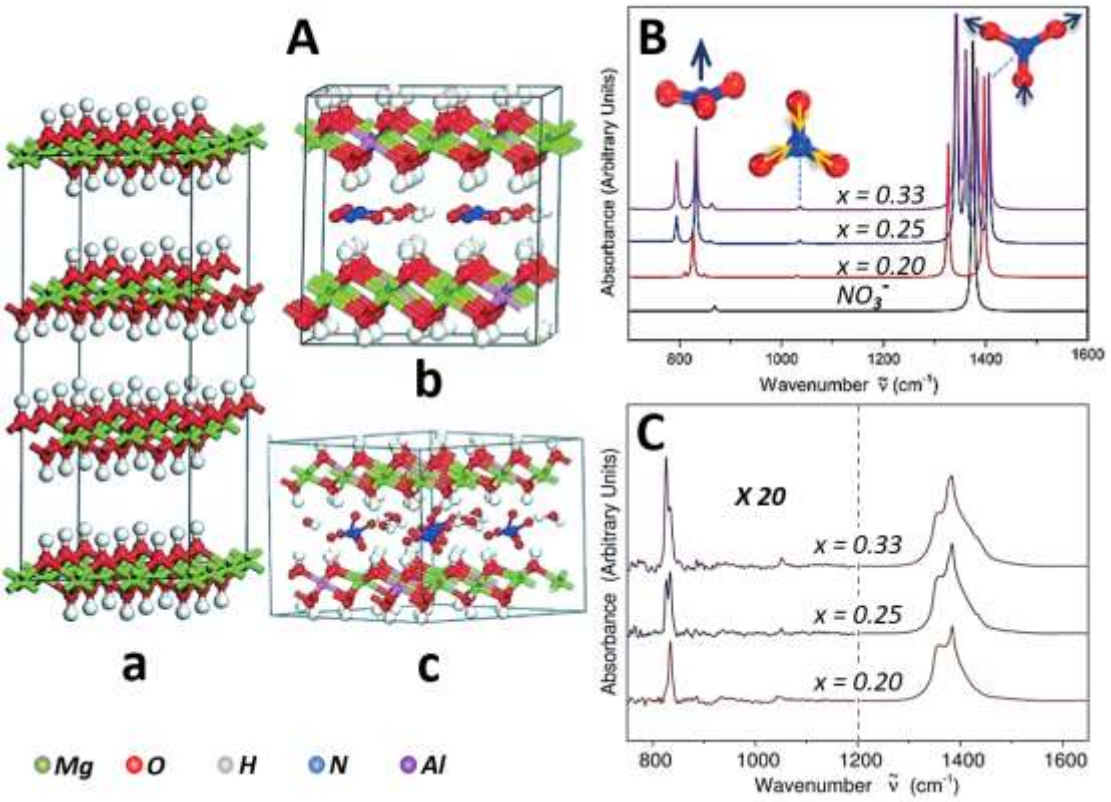

Fig. 15 A) Crystal structure of LDH without any interlayer anions within the A-B-C-A stacking (frame a). Intercalated NO_3^- and H_2O molecules in $Mg1–xAlx(OH)_2(NO_3)x·mH_2O$ for x = 0.125 (frame b) and 0.33 (frame c). For ease of visualization, the NO_3^- and H_2O species within the interlayers are displayed only between the A-B stacking layers. B) theoretically simulated IR spectra for $Mg_{1–x}Al_x(OH)_2(NO_3)_x·mH_2O$ (experimental: x = 0.20, 0.25,0.33; theory: x = 0.20, 0.25, 0.33) as well for gas-phase NO_3^- under ambient conditions (from theory). The origin for each mode is graphically represented in an insert. C) experimental IR spectra of the same compounds. Adapted with permission from ref. 188. Copyright 2015 Wiley-VCH.

4.4.2. Intercalated LDHs

The intercalation processes enlarge the possible applications of LDHs to ionic conductors, catalysts, electrodes, biomaterials and materials for optics, and to the removal of organic pollutants. The hosted molecules (that can have different molecular structure, dimension and charge density) can be oriented in a different fashion in the interlayer and this depends on the experienced interactions with the host structure (host-guest interactions), on the anionic concentration and the experimental reaction conditions.[189,190]

The synthesis of a LDH with Mg^{2+} and Al^{3+} in the ratio of 2:1 co-precipitated with cubane-1,4-dicarboxylate anion was reported, characterized by PXRD and FT-IR methods and

investigated by molecular modeling.[183] IR investigations reported H-bonding between the carboxylate and the LDH interlayer oxides owing to the electrostatic attraction between the electropositive cations in the layer and the organic anions in the interlayer. The dynamical properties, such as mean-square displacements and self-diffusion coefficients, were also analyzed for the intercalated organic anions and water molecules. Cubane-dicarboxylate anions were tilted approximately 54° from the perpendicular orientation to the LDH layer with water molecules dispersed in the interlayer as two main shells at about 0.97 and 1.57 Å from the cubane dicarboxylate end-groups in agreement with the XRD results.

In 2013, Wang *et al*. intercalated a model drug (glutathione, GSH) into LDHs by ion exchange, and a systematic study combining experimental and theoretical investigation was used to have information on the microstructure of LDHs and the reaction mechanism of the GSH intercalation into LDHs.[191] These results provide detailed structural information on the drug-LDHs system, insights into the arrangement of the interlayer anions, and the interactions between the hydroxide layers and the intercalated drug molecules. The simulated hydroxide layers were constructed by using the mineral hydrotalcite ($(Mg_4Al_2(OH)_{12}CO_3(H_2O)_3)0.5$) and the atomic position was obtained from the crystal structure of the X-ray diffraction data. DFT calculations were employed to model the inorganic framework. The geometry of GSH in the ground state (S0) was firstly optimized and then the vibrational spectra (IR and Raman) and ^{13}C NMR chemical shifts were calculated.

The calculated and experimental IR spectra of GSH were compared with those of the intercalated material and a reasonable agreement was observed, and this confirmed that the intercalation was successful. Solid-state NMR spectroscopy was applied to complement the information. The experimental data, in good agreement with the DFT calculations, indicated that, when intercalated, the chemical environment of the GSH changes: the ^{13}C NMR spectrum showed that the integrity of the GSH is well preserved in the interlayer of LDHs. Thus, the combination of FT-IR, ssNMR and computational techniques allowed depicting the structure of the drug-LDHs compounds and drawing a clear picture of the intercalation path of the organic molecule into LDHs.

In 2012, Costantino *et al*. proposed the preparation of LDH nanocontainers, suitable as carriers for Pravastatin, an anionic cholesterol-lowering drug.[192] The comparison of experimental and theoretical vibrational spectra showed that the main difference between sodium and intercalated forms of Pravastatin is due to the electrostatic interactions between COO^- group of the organic drug and the positive LDH layers. ^{13}C ssNMR data and their DFT

simulations also supported this finding. The development of reliable models for the intercalation compounds allowed the authors to assign the experimental ^{13}C ssNMR chemical shifts of both pure and intercalated Pravastatin as well as the vibrational FT-IR and Raman frequencies of the same compounds.

The incorporation of antioxidant molecules as phenolic compounds into LDH galleries is considered a feasible approach to improve their longevity and stability for various applications. The antioxidant 3-(3,5-di-*tert*-butyl-4-hydroxy-phenyl)-propionate anion (BHPPA) was successfully inserted at the interlayer of LDH with a Mg:Al ratio = 3 by utilizing the structural memory effect and its retained antioxidant activity was confirmed by the 2,2-diphenyl-2-picrylhydrazil radical-based colorimetric method.[185] The structure of intercalated species was characterized FT-IR spectroscopy that confirmed the presence of BHPPA anion as revealed by the position of the carboxylate asymmetric and symmetric stretching bands H-bonded to the LDH hydroxyls. The interlayer space revealed by XRPD combined to structural modeling accounted for a bilayer BHPPA arrangement at the interlayer and the co-existence water molecules. The most stable bilayer arranged to minimize the steric hindrance between close bulky *tert*-butyl groups thus resulting in a tilted orientation of the corresponding rings with respect to the layer hydroxyl groups.

Other examples report on the combination of FT-IR, ^{13}C ssNMR and DFT methods for the study of LDH intercalated with different drugs such as Sulindac,[193] Mefenamate[194] and benzoxaboroles.[115] All the reported examples illustrate well the potential of combined spectroscopic, structural and theoretical analyses: here, the role of DFT calculations is mainly to assist the interpretation of spectra and the assignment of difficult adsorption peaks or resonances. In many cases, this is accomplished by simulating the spectra of isolated molecules, and transferring the results to intercalated compounds, but in some cases a model of the interlayer space is proposed as well.[115]

The combination of FT-IR and ssNMR techniques has been often used to confirm the intercalation of different molecules inside LDH and to provide structural/molecular information on the intercalated solids. The following examples underline this aspect.

Costa *et al.* prepared Zn−Al layered double hydroxides (LDHs) containing solely 1-pyrenesulfonate (PS) or 1-heptanesulfonate (HS) anions, or a mixture of the two molecules with HS/PS molar ratios ranging between 7.5 to 8.2, by a direct synthesis method.[195] The

obtained solids were characterized by different experimental techniques including FT-IR, FT-Raman, and $^{13}C\{^{1}H\}$ CPMAS NMR spectroscopy.

The derivatives of fluorenone are chromophore molecules with intriguing photophysical performance to study, develop and apply as solid-state fluorescent materials. The organic anion 9-fluorenone-2,7-dicarboxylate (FDC) was assembled into highly-ordered LDH materials with Mg/Al and Zn/Al ratio = 2 because of its rigid planarity and vertical orientation relative to the LDH layer.[184] Polarization and delocalization of the electronic density of the anionic dye induced by the positively-charged LDH layers was revealed by comparing the ^{13}C MAS NMR features of pure dye with those of the assembled FD-LDH materials. In parallel, a blue shift of 20 and 7 cm^{-1} of the carbonyl band was observed for Mg/Al and Zn/Al LDHs thus indicating that the interaction between the FD carboxylate group and LDH layers was influenced by the elemental compositions of the latter. The periodic DFT calculation adopted to further study the geometric and electronic structures of the idealized model of the two systems structures revealed that the hybrid systems exhibit an energy transfer behavior from the interlayer chromophores to the LDH layer owing to the close energy levels between the π-conjugated fluorenone dicarboxylate and the LDH layer, favorable to produce a highly ordered orientation of transition dipole moment for polarized photoemission (Fig. 16).

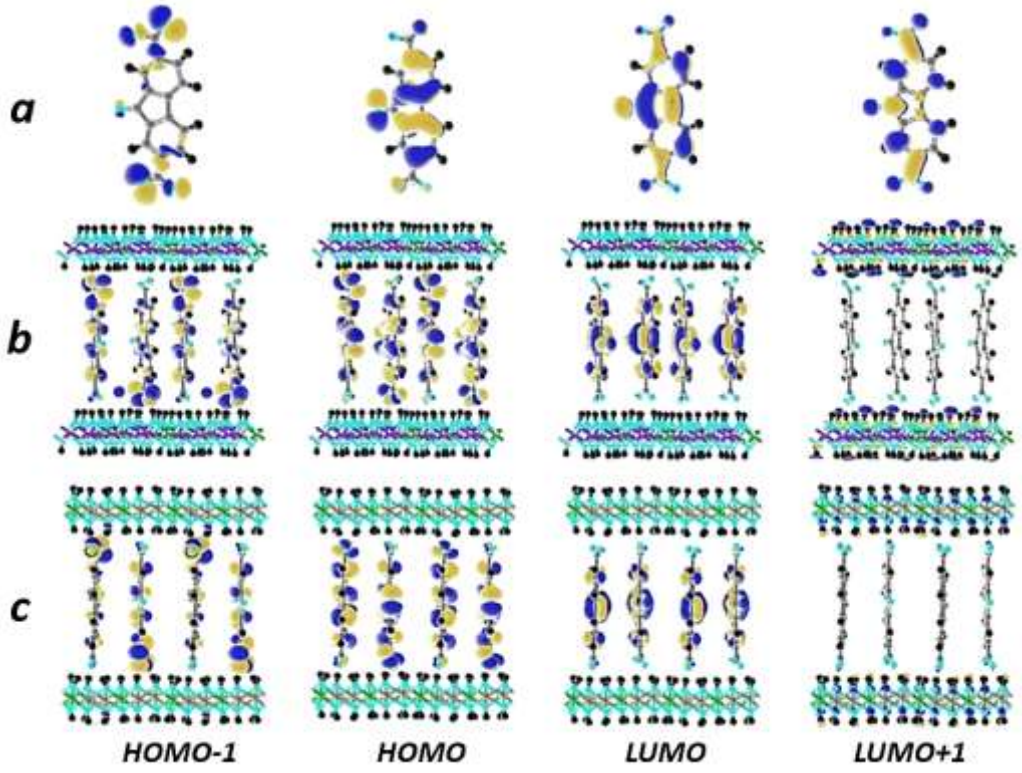

Fig. 16 Frontier orbital profiles (HOMO-1, HOMO, LUMO, LUMO+1) for (a) the pristine FDC, (b) FDC/Mg2Al-LDH, and (c) FDC/Zn2Al-LDH. Adapted with permission from ref. 184. Copyright 2013 The Royal Society of Chemistry.

Here a list of other examples where the combination of FT-IR and ssNMR techniques has been relevant to provide structural/molecular information on intercalated solids:

i) A novel MgAl-based LDH nanofiller intercalated with silsesquioxane-based aminoundecanoic acid (SAD) and grafted with the semiadduct of IPDI and 2-hydroxyethyl acrylate (IPDI-HEA) suitable for polymeric materials prepared by Shi *et al*.[196]

ii) Terephthalate-intercalated NiAl LDH materials proposed by Faro Jr.[197]

iii) The preparation of a composite material based on MCM-22 zeolite and HTLC.[198]

iv) Finally, Song *et al*. reported on the preparation of a LDH anchored ionic liquids as amphiphilic heterogeneous catalysts for the Knoevenagel condensation reaction.[199]

4.4.3. LDH for catalytic applications

LDHs are also largely used for catalytic applications. In this respect a recent work described the synthesis and the characterization of solid state catalysts for aldol condensation reaction, based on activated M-Al-LDH (where M=Ca, Mg).[200] The description of the active sites, formed by distorted $M(OH)_6$ octahedra, providing Brønsted acid moieties: a morphological and chemical difference between Ca and Mg compounds was found and characterized with a wealth of experimental (XPS, EXAFS, FT-IR, ^{27}Al MAS NMR) and computational (DFT) models. In this case, the computational contribution was to describe the structure of the metal hydroxide centres and estimate the strength of the Brønsted acidity; some calculation on model clusters supported the evaluation of the catalytic activity, and the structure-property correlation as well. Similarly, the catalytic activity of Ni[201] and Pd[202] supported by LDH was described by a combination of FT-IR and DFT calculations, along with EXAFS structural measures: in the former article, CO molecular probes were used for in-situ IR spectroscopy and the spectra interpreted with the aid of the theoretical simulations.

The effect of the cation arrangement on the electrocatalytic activity of Ni/Fe LDH in the oxygen evolution reaction was evaluated by comparing FT-IR spectroscopy and periodic DFT calculations, based on plane waves supplemented by the effective Hubbard-U

potential:[203] in this case, a 2D single layer was built to model the LDH with variable Fe/Ni substitution and the atomic arrangement was optimized at the DFT level; then, the reaction of oxygen evolution was simulated at the same level in this model system. Periodic DFT calculations were used in combination with XRPD and EXAFS on the same systems to evaluate the effect of different substitutions on the reaction.[204–207]

FT-IR, along with UV-Vis and XPRD techniques were used to characterize different Ni/Cr and Mg/Al LDH used for the removal of methylene blue, methyl orange and formaldehyde from aqueous solutions: in this study, preliminary DFT calculations described the geometrical arrangement and the electronic band structure of the various LDH samples, supporting the description of the catalytic activity.[208]

4.5. Layered perovskites

Layered perovskites have attracted enormous interest in the recent years because of their unique electronic[209,210] and photocatalytic properties.[211] They consist of perovskite-like slabs and interlayer cations or bismuth-oxide sheets, such as Dion– Jacobson, Ruddlesden–Popper and Aurivillius phases.[212] Moreover, different inorganic ions and organic compounds have been intercalated into the interlayer space of layered perovskites, thus giving rise to the preparation of compounds with novel properties.

In the following list the intercalation process and the structure of the intercalated systems have been studied by a combination of FT-IR and ssNMR:

i) Wang *et al*. reported a new method to intercalate carbon into the interlayer space of a layered $HLaNb_2O_7$ perovskite for modifying the band gap.[213] D-Glucopyranose was firstly grafted onto the interlayer surface of the layered perovskite via the reaction between the *n*-decoxyl derivative of $HLaNb_2O_7$ and D-Glucopyranose.

ii) D-Glucopyranose rings were successfully coordinated onto the interlayer surface of a Ruddlesden–Popper-type layered perovskite, $H_2CaTa_2O_7$, by a reaction with the precursor of *n*-decoxyl derivative of $H_2CaTa_2O_7$.[214]

iii) *n*-Alkyl chains were successfully grafted into the interlayer space of a Ruddlesden–Popper-type double-layered perovskite (with chemical formula $H_2CaTa_2O_7$) via a hydrolysis–esterification process.[215]

iv) Sugahara *et al*. intercalated triethylphosphine oxide [$(C_2H_5)_3PO$; TEPO] into protonated Dion–Jacobson-type ion exchangeable layered perovskites, $HLaNb_2O_7 \cdot xH_2O$ (HLaNb) and $HCa_2Nb_3O_{10} \cdot xH_2O$ (HCaNb).[216] The spectroscopic results suggested that TEPO is in interaction with Brønsted acid sites present on the surface of the solids and that this molecule exhibited different orientations with respect to the inorganic layers.

In few cases, ab initio calculations have been used to support the interpretation of NMR and FT-IR characterization of inorganic or hybrid layered perovskites, whose main interest is in catalysis, though some systems was suggested for photovoltaics applications too.

Kessentini *et al.* diffusely used DFT calculations, with hybrid functional and basis sets including effective core potentials to reduce the computational cost, to assign the vibrational bands in IR and Raman characterization of CdI_4 and $CuCl_4$ perovskites intercalated with organic cations.[217,218] Similarly, the vibrational modes of copper chlorides with organic intercalates were discussed and assigned by Dammak *et al.* through the comparison with existing databases for isolated molecules supplemented by DFT calculations at the same level as above.[219]

The crystal structure of some layered ceramics based on mixed oxides, $La_2Sn_{2-x}Ti_xO_7$ and $RbSr_2Nb_3O_{10}$, was determined by a combination of XRD and ^{119}Sn and ^{87}Rb NMR. In both cases, the resonance spectra were interpreted with the aid of DFT calculations of chemical shifts and EFG tensors: in one example[220] the theoretical analysis also allowed to predict the relative stability of two layered phases undistinguishable from the NMR results, while in another case[221] the geometrical deformation of the layers in a Dion-Jacobson phase was described by comparing the theoretical and the recorded resonance spectra.

A similar approach, based on XRD and ^{87}Rb NMR supported by DFT calculations, was used to determine the crystal structure of $Rb_3Bi_2I_9$: the theoretical approach was also used to describe the optical (absorption and photoluminescence) properties.[222]

It is worth noting that in the above examples the DFT methods were based on localized basis functions and hybrid functionals, as is common in the calculations of spectroscopic parameters to be compared to the experiments. It has been shown repeatedly, on the other hand, that the theoretical optimization of crystal structures as well as the calculation of electronic properties, e.g. band structures, for 2D and 3D perovskites require a careful consideration of spin-orbit coupling (SOC),[223] and possibly also of long-range Coulombic

interactions.[224] These contributions are usually computed within plane waves approaches with non-local density functionals, but a discussion of their possible weight on the simulation of FT-IR or NMR spectra is outside the scope of this work.

4.5.1. Colloidal perovskite nanocrystals

Colloidal nanocrystals of alkaline earth perovskite oxides having the formula ABO_3 (A = Ca, Sr, Ba; B = Ti, Zr), and their corresponding quaternary $A_{1-x}A'_xBO_3$ solid solutions, exhibit a wide range of technologically relevant properties. The versatility of this family of complex oxide nanocrystals stems from the compositional dependence of their physical properties. An interesting example of the coupling of computational and experimental techniques was given by Coperet *et al*.[225] They investigated the CO_2 chemisorption on colloidal $Ba_{1-x}Sr_xTiO_3$ nanocrystal surfaces using different techniques, including in situ FT-IR, ^{13}C ssNMR spectroscopy, and DFT calculations. CO_2 was used as a probe molecule for the study of basic sites. Prior to CO_2 exposure, the FT-IR spectra of the calcined nanocrystals showed the presence of amorphous alkaline earth carbonates. After CO_2 addition to the perovskite nanocrystals, the bands in the same C–O spectral region become more complex and increase in intensity. In order to examine specifically the adsorption and binding modes of CO_2 at the surface of the perovskite nanocrystal, labelled $^{13}CO_2$ was contacted with the samples and ^{13}C ssNMR spectra were collected. Periodic DFT simulations were performed in order to propose assignments for the observed species.

5. 3D porous solids

The pursuit for new efficient 3D porous materials has materialized a significant increase in their publications in the last few years.[1,226] Porous 3D solids with high surface area and active sites are important in both science and technology fields for applications in catalysis, adsorption, separation, gas storage and molecular confinement for technological/biomedical applications. On the other hand, for the rational design and synthesis of porous 3D solids, knowledge about structure-property relationship is essential. Different type of 3D porous materials will be considered (Fig. 17) and will be highlighted how the combination of techniques is a powerful tool to elucidate structure-properties relationship. The powerful combination of ssNMR and FT-IR spectroscopy together with computational methods is already leading to new insights and addresses key issues related to studies of confined spaces.[62,227–229]

The area of inorganic-organic/organic/polymer based framework porous materials (MOFs, COFs, POPs, PAFs, MOPs, PIMs, CMPs, HCPs, CTFs, PMMs) has witnessed extensive attention and rapid growth over the past two decades due to their applications in drug delivery, imaging, catalysis, sorption, separation and storage of gases etc.[230–256] Given that the field of inorganic-organic/organic/polymer frameworks based porous materials research is incredibly diverse, we will omit their coverage and readers are invited to read the excellent reviews that have appeared recently in these areas.[248,251,257–269]

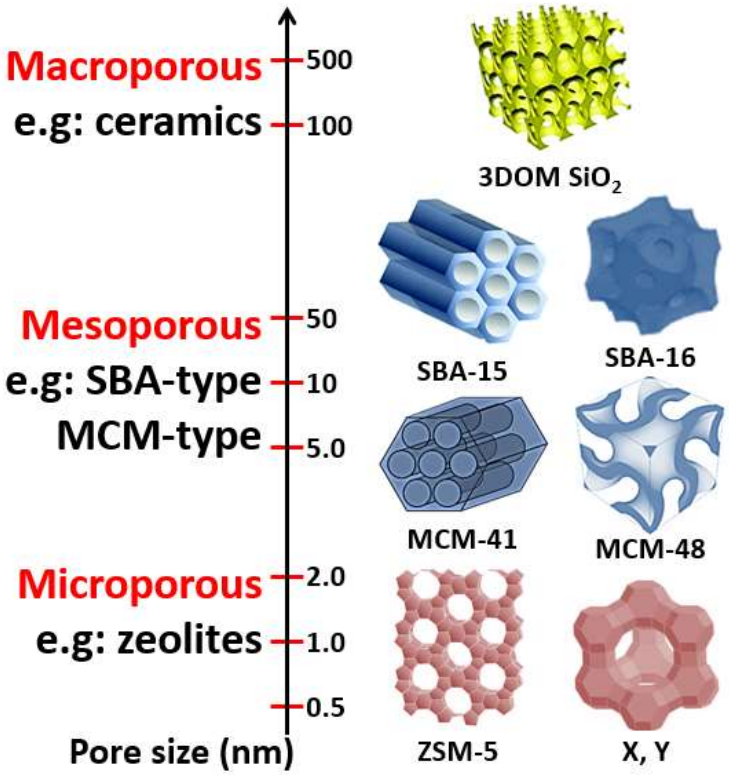

Fig. 17 Classification of selected 3D silica based porous solids according to pore size.

5.1. Microporous materials

5.1.1. Classical zeolites

Zeolites are molecular sieves of robust crystalline silica alumina framework structure formed by a continuous network of oxygen-sharing SiO_4 and AlO_4 tetrahedra. The unit negative charge in the framework created by the presence of one Al^{3+} ion in the tetrahedral position is complemented by loosely held inorganic cations (alkali or alkaline earth cations) or organic cations that reside in the cavities preserving the electroneutrality of the zeolite. Based on IUPAC recommendations, they are classified as microcrystalline porous materials as their average pore diameter falls below 2 nm. The great interest in these microporous materials are due their tuneable physico-chemical properties such as high surface area and pore volume, surface acidity and basicity with ion exchange capacity, high thermal, hydrothermal and mechanical strength. They have found applications in a wide range of fields including catalysis, gas storage, molecular sieve, ion-exchange etc.

In order to achieve wider range of applications, the development of zeolites with extra-large pores and chiral centres are desirable. Over the past few years, there have been considerable efforts to synthesis newer zeolite material and interesting candidates will be reviewed in this segment.

5.1.2. Formation of materials and their structural characterization

Layered zeolites are unique microporous material composed of rigid zeolitic lamellae. In contrast to traditional 3D zeolites, layered zeolites originate from zeolitic precursors consisting of lamellar sheets of unit cell thickness. Wu *et al*. have reported silylation strategy for converting 2D precursors into novel 3D zeolites with high crystallinity by inserting monomeric silanes into the interlayer spaces, producing a series of interlayer expanded zeolitic (IEZ) materials.[270,271] In a recent report, they have adopted a versatile and convenient one-pot post synthesis strategy in the preparation of novel titanosilicate catalysts by simultaneous isomorphous substitution and interlayer expansion of zeolitic layered silicates.[272] The structural transformation and the incorporation of Ti in the preparation of IEZ were monitored using a multi-technique approach. High level DFT calculations along with Rietveld refinement of the XRD data and ^{29}Si and ^{13}C solid-state MAS NMR and FT-IR spectroscopies helped them to perform the structural analysis and catalytic activity studies.

Bottom-up approaches using 2D layered silicates are promising for precise design of 3D crystalline microporous materials and are known for a while. The layers of 2D silicates possess Si−O$^-$ negative charges as well as abundant Si−OH groups with ordered arrangements on the surfaces. Silylation of these layered silicates leads to the formation of new Si−O−Si linkages and larger interlayer pore than those of zeolites obtained by direct interlayer condensation through simple calcination. Asakura *et al*. prepared a novel crystalline microporous material by silylation of layered silicate RUB-51 with tetrachlorosilane and heat treatment for interlayer condensation.[273] They have employed ^{29}Si MAS NMR and FT-IR spectroscopy to follow the bottom-up approach from layered parent material to final 3D microporous zeolite. The evolution of layered silicate RUB-51 to a 3D porous solid was followed by a comparison of ratios of the relative intensities of Q^2:Q^3:Q^4 units as shown in Fig. 18 (A). The large amounts of Q^3 units in heated-tetra-RUB-51indicate that surface silanols are abundant in the pores of final 3D material. FT-IR spectroscopy was also used to determine the presence of OH groups on the surfaces of the obtained pores (Fig.

18 (B)). They have observed signals owing to the stretching vibration of free or slightly hydrogen (3724 and 3691 cm^{-1}) bonded OH groups, which proves the presence of isolated silanols groups inside the micropores of the final material.

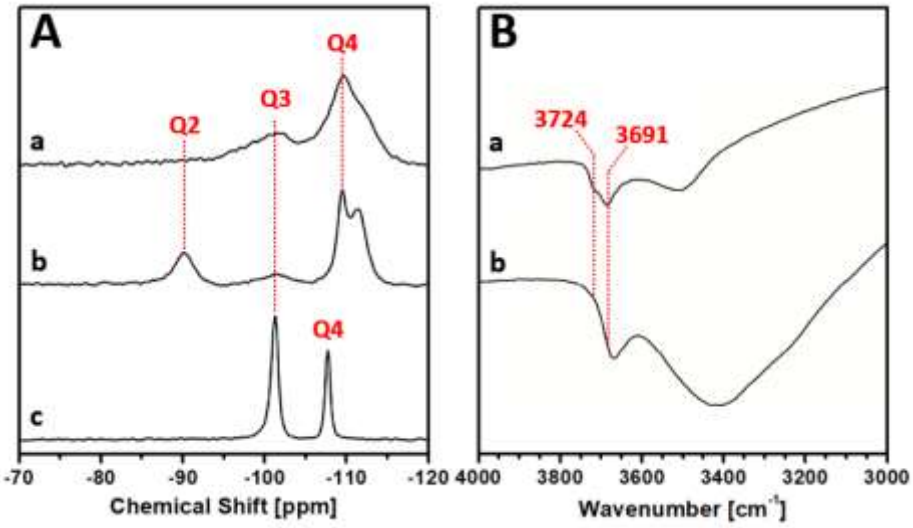

Fig. 18 (A) ^{29}Si MAS NMR spectra of (a) RUB-51, (b) Tetra-RUB-51, and (c) Heated-Tetra-RUB-51 and (B) IR spectra of (a) Heated-Tetra-RUB-51 and (b) Heated-Tetra-RUB-51 after heating at 200 °C for 4 h. Adapted with permission from ref. 273. Copyright 2014 American Chemical Society.

In another study, the transformation mechanism of layered silicate RUB-36 to ZSM-35 zeolites, revealed to be a topotactic conversion process, was investigated in detail by a multi-technique approach.[274] Local interactions between the inorganic building blocks and organic moieties are of key importance to drive the topotactic conversion and to form a zeolite phase. Multi-dimensional ssNMR spectroscopies along with theoretical simulations provided a powerful combination to explore the local environments and interactions in porous materials. In this study, they employed ^{1}H–^{29}Si as well as ^{1}H–^{27}Al HETCOR NMR experiments to probe the spatial connectivity through heteronuclear dipolar interactions. The structure-directing role of the organic moieties was also illustrated by theoretical Monte Carlo simulations. Cejka *et al*. have reported the synthesis of multifunctional porous hybrid material based on the covalently bonded organic–inorganic nanosystems using a top-down approach from zeolite UTL.[275] The porous hybrid material obtained by intercalation with silsesquioxane possessed layered morphology and exhibited hierarchical micro-/mesoporous systems, stable up to 350 °C. Katz *et al*. have used single-step delamination of MWW

borosilicate using aqueous $Al(NO_3)_3$ to prepare aluminosilicate zeolite.[276] Multi-technique approach involving FT-IR and ssNMR spectroscopy established the formation of Brønsted acid sites upon delamination.

The ADOR (assembly–disassembly–organisation–reassembly) mechanism for the synthesis of new zeolites has been recently reviewed by Cejka *et al*.[277] According to this strategy, a previously assembled zeolite is selectively and controllably disassembled into layered building units, which are then organised into a suitable orientation before being reassembled into a new zeolite structure. They claim that the limitation of the traditional synthetic methodologies can be overcome by ADOR process and can fully exploit the potential of zeolite synthesis of all types. There has been a few reports in the recent past that adopted ADOR process for the preparation of new zeolites.[278–280] Ashbrook *et al*.[5] have applied multinuclear ssNMR spectroscopy to sheds light on the role played by water in the ADOR process and to gather insight into the detailed mechanism of the structural changes involved. From ^{17}O and ^{29}Si NMR experiments they were able to demonstrate that the hydrolysis and rearrangement process occurs over a much longer time scale than seen by diffraction.

In a recent report, the local structures of framework ^{27}Al Lewis sites in dehydrated zeolites and their precursors in hydrated zeolites were studied by a combined approach of high-resolution MAS NMR and FT-IR spectroscopy as well as DFT/MM calculations.[102] They have identified tri-coordinated framework aluminium in a mildly dehydroxylated zeolite, which can act as Lewis acid site in catalytic reactions, and exhibits a very broad ^{27}Al resonance ($\delta_{iso} \approx 67$ ppm, $C_Q \approx 20$ MHz, and $\eta \approx 0.1$). The origin of this site was identified to a "perturbed" framework Al atoms in the hydrated precursor zeolite of the form $(SiO)_3AlOH$. The assignment was supported by the presence of the IR vibration at 3655 cm^{-1} due to the O-H stretching mode of terminal $(SiO)_3AlOH$. Furthermore, calculation of NMR parameters (δ_{iso} = 59-62 ppm, C_Q = 5 MHz, and η = 0.3-0.4) was in good agreement with the experimental results (Fig. 19).

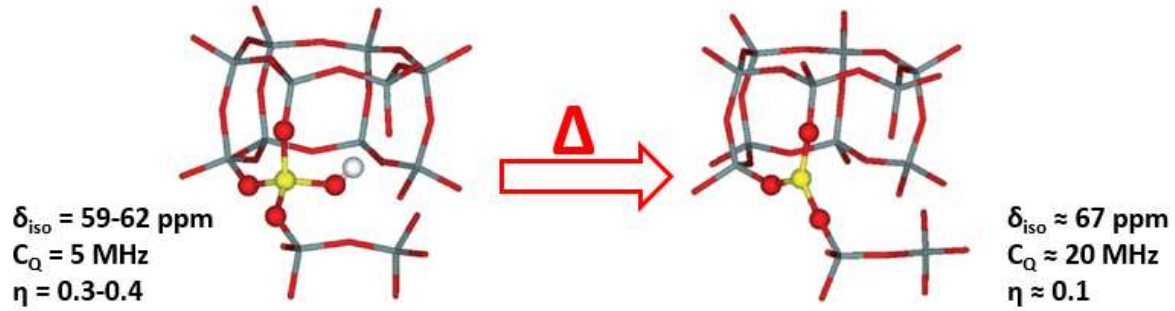

Fig. 19 Structure of a terminal $(SiO)_3AlOH$ group and the corresponding dehydroxylated $(SiO)_3Al$ in the CHA zeolite with the atoms corresponding to O_3AlOH displayed as balls. Silicon atoms are grey, the aluminium atom is yellow, oxygen atoms are red, and the hydrogen atom is white. Adapted with permission from ref. 102. Copyright 2015 Wiley-VCH.

Mapping of various Sn sites in Sn-β zeolites according to chemical shifts were carried out by Wolf *et al*. employing a multi-technique route involving ssNMR and first principle calculations.[281] Their study indicated that the materials showing the highest activity prepared by traditional hydrothermal method possess a highly hydrophobic, defect-free zeolite framework, whereas post-synthetically synthesized Sn-β samples prepared in two steps via dealumination and subsequent solid-state ion exchange from Al-β showed significantly lower activity, which was associated with a hydrophilic framework and/or a lower accessibility. They have concluded that the activity of Sn-β in the aqueous-phase isomerization of glucose was highly dependent on the hydrophobicity of the material. In addition, accessibility and T site positioning of the Sn site, both defect-open and closed sites, were found to be important.

Nakazawa *et al.* have employed a multi-technique approach to solve the structure of a novel aluminosilicate zeolite (YNU-5), a zeolite containing interconnected 12 membered ring (MR), 12MR, and 8MR pores, as well as independent straight 8MR channels.[282] The chemical composition and local structures of constituent elements of the new zeolite were analysed by ssNMR and FT-IR spectroscopy. The Si/Al ratio was estimated as 9.4−10.2 from the ^{29}Si MAS NMR spectrum, while the stability of cationic molecules ($Me_2Pr_2N^+$) in the as-synthesized sample was determined by ^{13}C CPMAS NMR spectrum. In addition, the presence of Na^+ ion with a single local structure was confirmed by ^{23}Na MAS NMR and a four-coordinated Al site was detected by ^{27}Al MAS NMR of as-synthesized YNU-5. Furthermore, FT-IR spectrum of pyridine adsorbed on YNU-5 (Si/Al = 8.4, H^+ form) established the

Brønsted acid sites and Lewis acid sites. Such detailed characterization studies supported in the structural elucidation of YNU-5 by *ab initio* analysis from powder diffraction data.

Structure-directing behaviours of TEA cations toward zeolite Beta was studied by Okubo *et al*.[283] Unlike the role of most OSDAs in zeolite synthesis, the case for zeolite Beta synthesized by using TEA cation is different, where a cluster/aggregate of *ca.* six TEA cations are occluded in the channel intersection of zeolite Beta. From a multi-technique approach, it was revealed that the formation of amorphous TEA^+−aluminosilicate composites and their structural, chemical, and textural evolution toward the amorphous zeolite Beta-like structure during the induction period was vital for the formation of zeolite Beta. The conformational rearrangement of TEA cations has a strong influence with the formation of micropores and the incorporation of Al in the aluminosilicate Beta framework.

Interactions of zeolites with water strongly depend on the presence of hydrophilic moieties including BAS, extra-framework cations, and silanol defects. Resasco *et al*. have systematically studied the crystallinity changes of a series of zeolites (HY, H-ZSM-5, and H-β) with varying Si/Al ratio, density of BAS, zeolite structure, and density of silanol defects upon exposure to liquid water at 200 °C.[284] The most crucial role in zeolite stability in hot liquid water was played by the density of silanol defects. They have proposed that the tolerance of defective zeolites to hot liquid water can be greatly enhanced by functionalization with organosilanes. Similarly, in a combined approach of employing FT-IR and ssNMR spectroscopy,[285] Prodinger *et al*. have demonstrated the significant improvement in the material stability in hot liquid water for microporous zeolite Beta upon post-synthetic silylation treatment. The defects in the siloxy bonds were capped by reaction with trimethylchlorosilane and Si−O−Si bonds were eventually formed. Silylation led to the reduction of the concentration of internal structural defects significantly and enhanced the zeolite stability in hot liquid water.

Solid-state NMR spectroscopy and DFT calculations were combined to study the impact of aqueous medium (heated for 48 h at 160 and 300 °C in an autoclave while being stirred at 600 rpm) on framework integrity of zeolite Beta by Lercher *et al*.[286] They explored the effects of various properties, including Al concentration, Al distribution, particle size, and structural defects on zeolite stability in aqueous medium. The combined data suggested that the crystallinity decreased via selective hydrolysis of the T1- and T2-sites that form the 4MR pores of the zeolite framework resulting in amorphization of the sample. The combination of techniques allowed speciating the location and concentration of Al in the HBEA lattice.

Park *et al*. proposed a reliable formation pathway for UZM-5 zeolite crystals based on the MAS NMR and FT-IR spectroscopy.[287] UZM-5 zeolite synthesized via the charge density mismatch approach resulted in a novel framework topology (UFI) crystallized with four different building units. Solid state ^{29}Si, ^{27}Al and ^{13}C MAS NMR as well as FT-IR spectroscopy were used to characterize the solids isolated in a time series that helped to determine the evolution in structure building process and crystallization. ^{29}Si MAS NMR spectra of solid products separated at early stages of crystallization shown the formation of X-ray amorphous solids and were characterized by one very broad line around −101 ppm (Fig. 20 A). When crystallization time was longer than 24 h, this line disappears and four narrower lines begin to be resolved and were due to the simultaneous dissolution of the initially formed amorphous solids and the growth of Na-UZM- 5 crystals. Similarly, FT-IR spectra in the structural region of solid products showed a weak band around 545 cm^{-1}, assigned to the single 5MR (*s5r*) unit, a part of both *wbc*- and *rth*-cages, originated after 30 h or longer and a band around 570 cm^{-1} due to the *d4r*-cage unit was observed only after 48 h (Fig. 20 B). From these data, they have reasoned that *d4r*-cages were formed after *wbc*-cages, assuming the connecting mode of building units in the UFI structure.[288]

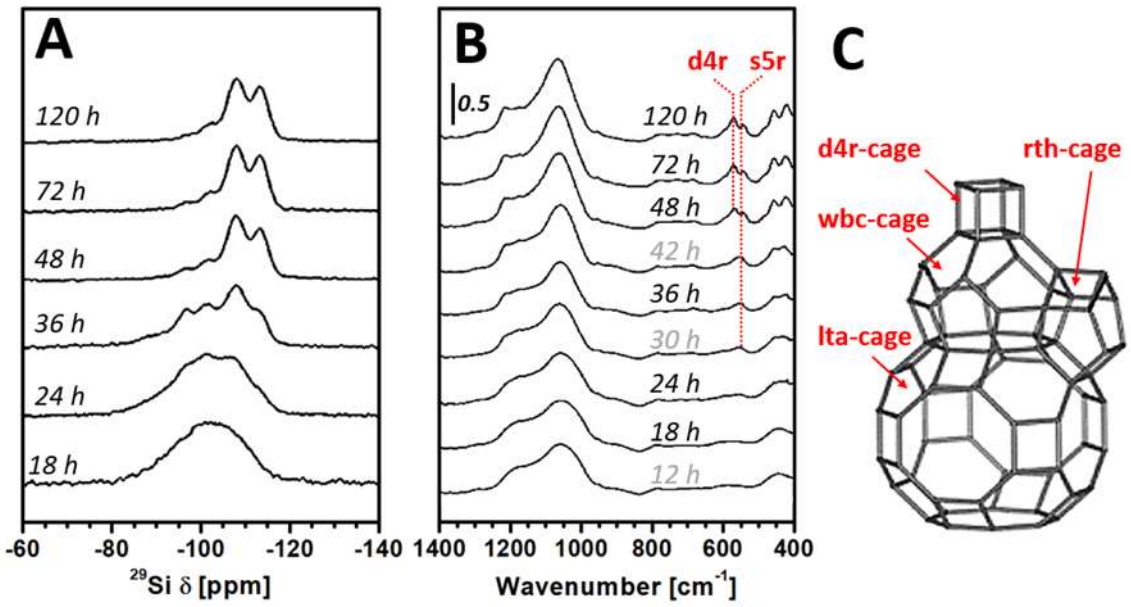

Fig. 20 ^{29}Si MAS NMR spectra (A) and FT-IR spectra (B) of solid products separated after Na-UZM-5 crystallization under rotation (60 rpm) at 150 °C for different times. UFI structure building unit with different cages (C). Adapted with permission from ref. 287. Copyright 2015 American Chemical Society.

Xia *et al*.,[289] for the first time, applied dry-gel conversion technique to prepare organic-inorganic hybrid aluminosilicate zeolites. They followed the synthesis, structure formation and framework modifications through the combined application of ssNMR and FT-IR spectroscopy. Methylene-bridged hybrid zeolite with MOR topology was sulfonated with fuming sulphuric acid to form acidic MOR-SO_3H catalyst, which exhibited high catalytic activity.

Dzwigaj *et al*. applied post-synthesis procedure to prepare molybdenum incorporated Beta zeolite with isolated mononuclear Mo(VI) species, which were characterized using a multi-technique strategy.[290] The incorporation of Mo into the vacant T atom sites was confirmed by FT-IR and MAS NMR spectroscopy. A decrease of the intensity of the IR bands due to isolated internal, terminal internal and hydrogen bonded silanols groups suggested their reaction with the Mo precursor. The same mechanism of incorporation was monitored by the disappearance of peaks in the range 1−4 ppm of the ^{1}H NMR spectrum of Beta.

The same group has further applied multi-technique approach to identify the state of silver ions in the framework of Beta zeolite.[291] To obtain well-dispersed silver species, they have employed a two-step post-synthesis method that allowed the incorporation of silver ions in the framework of zeolite mainly as isolated mononuclear silver species without the formation of metal oligomers or metal oxides. The consumption of OH groups as a result of their reaction with the silver precursor as well as the acidity of the thus formed AgSiBEA has been investigated by FT-IR spectroscopy of adsorbed CO and pyridine used as probe molecules. The changes in the silver state as a function of Ag content have been identified by ^{109}Ag MAS NMR spectroscopy along with other techniques. While the low silver content zeolite showed a signal at 21.5 ppm associated with framework mononuclear Ag(I), high content zeolite exhibited a signal with the chemical shift at -33.2 ppm linked to $Ag_n^{\delta+}$ clusters.

The acidity of hierarchical USY, Beta and ZSM-5 zeolites obtained by alkaline treatment was investigated by Rac *et al*.[292] using multi-technique approach. A comparison, before and after treatment, led to the conclusion that mesopore formation via alkaline treatment in zeolites resulted in acidity alterations. The concentration of acidic sites was almost completely preserved after the modification in all three zeolitic structures, but their distributions in strength were affected. While FT-IR investigations revealed that Brønsted sites strength was more affected by the alkaline treatment than Lewis sites strength, ^{27}Al NMR results showed the redistribution of Lewis sites. Catalytic performance, tested in fructose dehydration

reaction, was shown to be significantly improved in terms of HMF selectivity, when compared to the parent samples.

Van Aelst *et al*. studied the influence of aqueous ammonia treatment on USY zeolite which they wanted to use as a catalyst support with a hierarchical pore system containing micro- and mesopores.[293] The effect of the contact time with the ammonia solution was investigated as well as the effect of subsequent thermal treatments. They applied a suite of 1D and 2D NMR protocols, including ^{1}H DQ-SQ (Fig. 21), ^{27}Al MQMAS, ^{29}Si MAS and CPMAS, and ^{1}H-^{29}Si HETCOR. These authors have observed an increasing loss of crystallinity upon increasing duration of ammonia treatment. However, shorter duration treatment resulted in complex hierarchical material with mesopores and zeolitic micropores next to a dense amorphous aluminosilicate, containing NH_4^+ ions, highly structured water, and silanol nests.

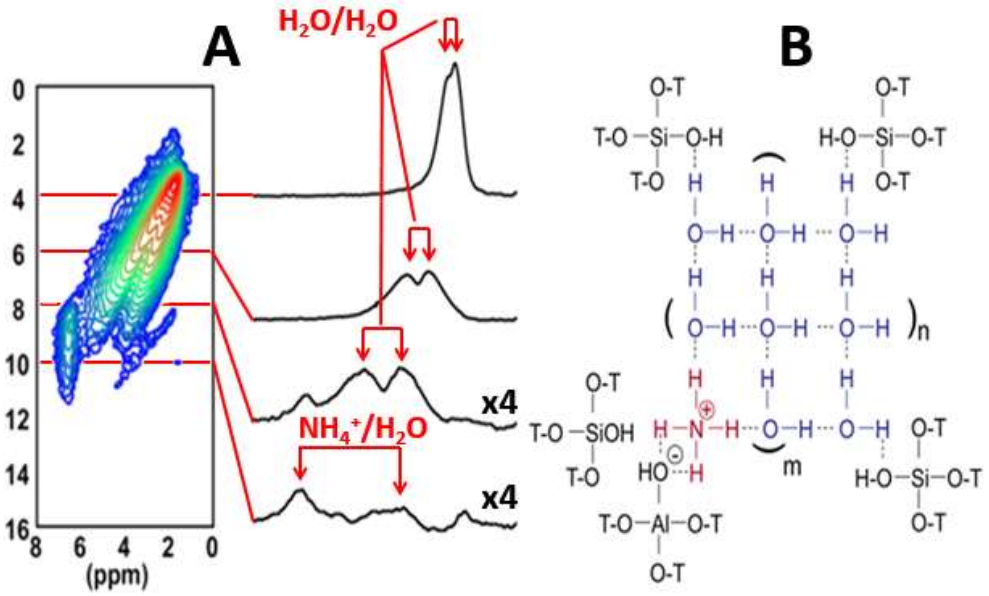

Fig. 21 2D DQ–SQ ^{1}H–^{1}H POST-C7 spectrum (A) of the dehydrated USY zeolite treated with NH4OH solution for 16 h. Some selected slices along the t_1 axis are shown. Proposed local structure of the amorphous hydrated ammonium silicate phase (B). Adapted with permission from ref. 293. Copyright 2014 American Chemical Society.

Fernandez *et al*. reported very recently the role of structure-directing agent in localizing the silanol defects within the framework of silicalite with MFI topology.[294] These authors applied 2D double-quantum ^{1}H MAS NMR experiments with spinning sideband patterns (ssb) simulations to clarify the location and distribution of these defects with respect to tetrapropylammonium (TPA^+) in the as-synthesized silicalite-1 (Fig. 22). The silanol defects (in $SiO^-\cdots HOSi$ structures) are preferentially placed near the methyl groups of the TPA^+

cation at the mid distance between the channels intersections with the inter-nuclear distance between silanol and methyl protons at approximately 3.3 Å, whereas between silanol protons at approximately 3.0 Å. According to this study, two silanols participate in the compensation of the siloxy negative charge. Their approach can also be applied to other zeolites in order to locate the defects or active sites for better understanding of materials properties.

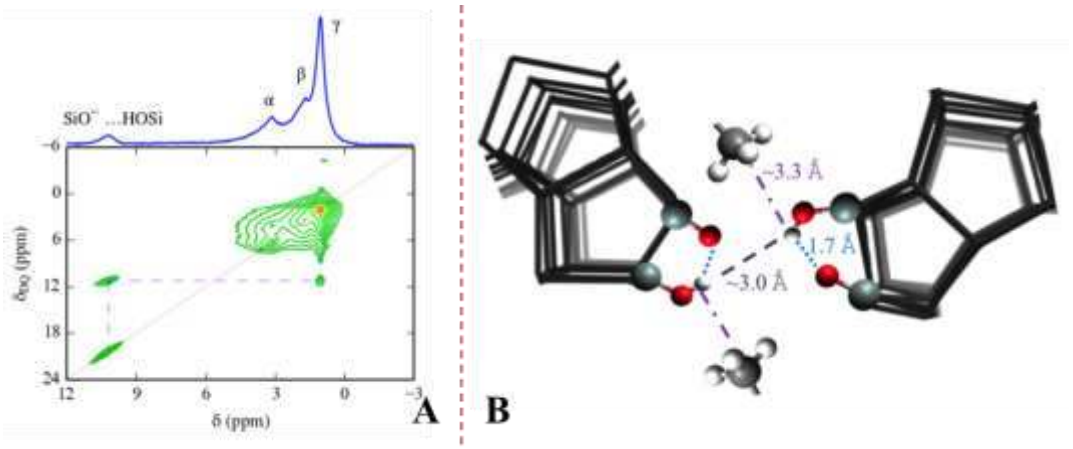

Fig. 22 Conventional MAS (top, in blue) and 2D double quantum (bottom) ^{1}H NMR spectrum recorded using Back-to-Back (BaBa) sequence on the as-synthesized TPA-silicalite-1 at 500 MHz (A). Schematic representation of the SiO^{-}···HOSi defects in the vicinity of TPA methyl groups (B). Adapted with permission from ref. 294. Copyright 2015 American Chemical Society.

Brunklaus *et al*. have applied ^{1}H double and triple quantum NMR spectroscopy to investigate the clustering of defect groups (SiOH and SiO^{-} groups) and their location within the pore walls of four as-synthesized zeolites.[295] The interaction between organic SDA and defect sites as well as among defect sites in zeolites ZSM-12, ZSM-5, SSZ-74 and SSZ-24 was revealed by DQ and TQ coherences. As shown in Fig. 23 a and b they have observed a DQ signal at 20.6 and a TQ signal at 30.9 for as-synthesized ZSM-12. Similarly, the DQ and TQ signals were at 20 and 30 ppm for ZSM-5 (Fig. 23 c and d). Double quantum and triple quantum signals mandatorily require at least a pair of protons and a cluster of three protons in close proximity, respectively. The interaction between the structure directing agent and silanol was found by a DQ signal at 13.5 ppm in ZSM-12 as well as at 10.8 ppm in ZSM-5. They found that connectivity defects were dominant in ZSM-5, ZSM-12, and SSZ- 24, but ordered vacancy defects existed in SSZ-74 instead. They concluded that there is a preferential interaction between framework defects and SDA charge centres, provided that this is

sterically possible. From their structural models, the organic structure directing agent appears to have an important role on the location and orientation of silanol defects in the zeolite framework.

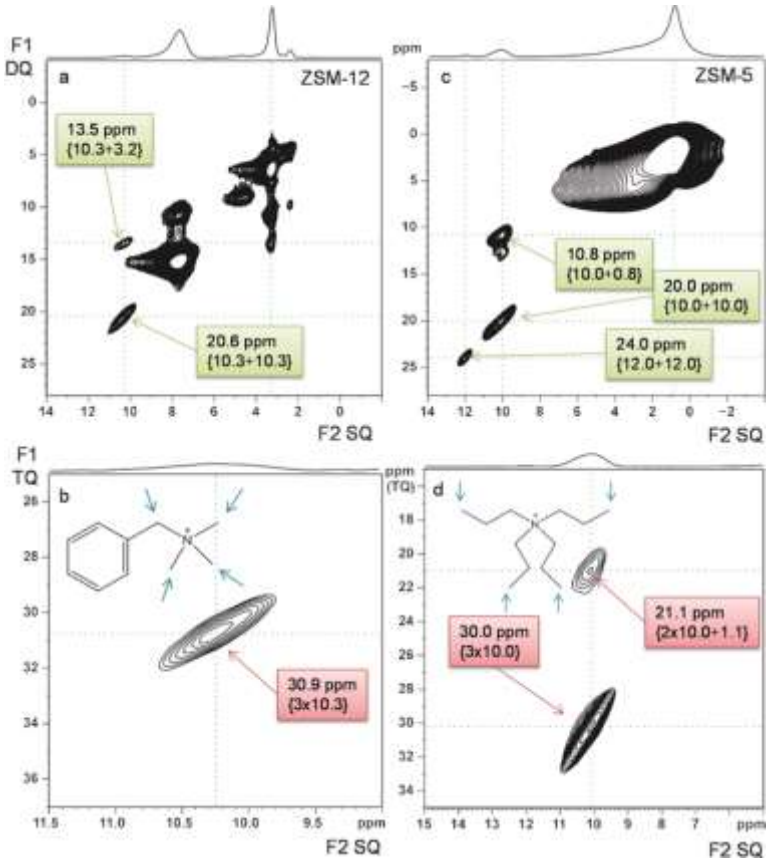

Fig. 23 a) ^{1}H DQ and b) ^{1}H TQ MAS NMR data of ZSM-12; c) ^{1}H DQ and d) ^{1}H TQ MAS NMR data of ZSM-5; Part of structure directing agents (arrows) that interact with the defect protons. Reproduced with permission from ref. 295. Copyright 2016 Wiley-VCH.

Dib *et al*. showed that the local disorder in as-synthesized ZSM-5 could be studied and quantified using ^{14}N MAS NMR as the SDA is usually tetrapropylammonium (TPA) in this zeolite.[296] Insights on the atomic local disordering, which are difficult to be acquired using diffraction methods, could be established by ssNMR crystallography approaches (See the special issue of Acta Crystallographica C http://journals.iucr.org/c/issues/2017/03/00/). The analysis of ^{14}N (a quadrupolar nucleus) spinning side-band patterns of a series of as-synthesized ZSM-5 zeolites containing various amounts of Al were shown to evolve with the Si/Al ratio. The structural information was generated from the quadrupolar coupling parameters (coupling constant, C_Q and asymmetry parameter, η_Q), which defined the width and the shape of the ^{14}N resonances. The influence of the zeolite framework modifications due to Al/Si substitution on ^{14}N NMR parameters was obtained from the DFT calculations.

They have identified two types of interrelated disorder due to the insertion of Al in silica framework. Firstly, the Al substitution leads to a distribution of charges that affects directly the electric field gradient (EFG) at ^{14}N sites. Secondly, the geometrical modification of the zeolite at short-range scales is due to heteroatom substitution, as this produces local variations in electron densities that again affect EFG at ^{14}N sites. These two factors lead to possible rearrangements of the TPA molecules (displacements, conformational changes, etc.) to minimize the intra- and intermolecular electrostatic interactions. As the sitting position of Al atom (one of the 24 possible tetrahedral crystallographic sites) changes, and is responsible for changes in the C-N-C angles in TPA and a deviation from T_d symmetry, very different sets of ^{14}N quadrupolar parameters were obtained.

Tang *et al*. successfully employed micro-explosion method by microwave assisted decomposition of H_2O_2 to create mesopores from the interior zeolite crystal toward the exterior.[297] The effects of the micro-explosion process on the properties of the zeolites were investigated by ssNMR and IR spectroscopies. The ^{1}H spin-echo MAS NMR spectrum showed peaks due to Brønsted acid sites and isolated silanols, in parent Beta zeolite. After microwave treatment, a broad signal owing to H-bonded hydroxyls centred at 4.9 ppm as well as hydroxyls related to extra-framework aluminium can be drawn by the small peaks at 3.6 and 0.2 ppm. Moreover, ^{27}Al MAS NMR spectra of microwave treatment samples showed two additional tetrahedral framework ^{27}Al at two distinct lattice positions of zeolite Beta (Fig. 24). On the other hand, FT-IR spectra showed good preservation of BEA framework during micro-explosion. Pyridine adsorption FT-IR data revealed no notable decrease in the total density of acidic sites but the presence of slight dealumination.

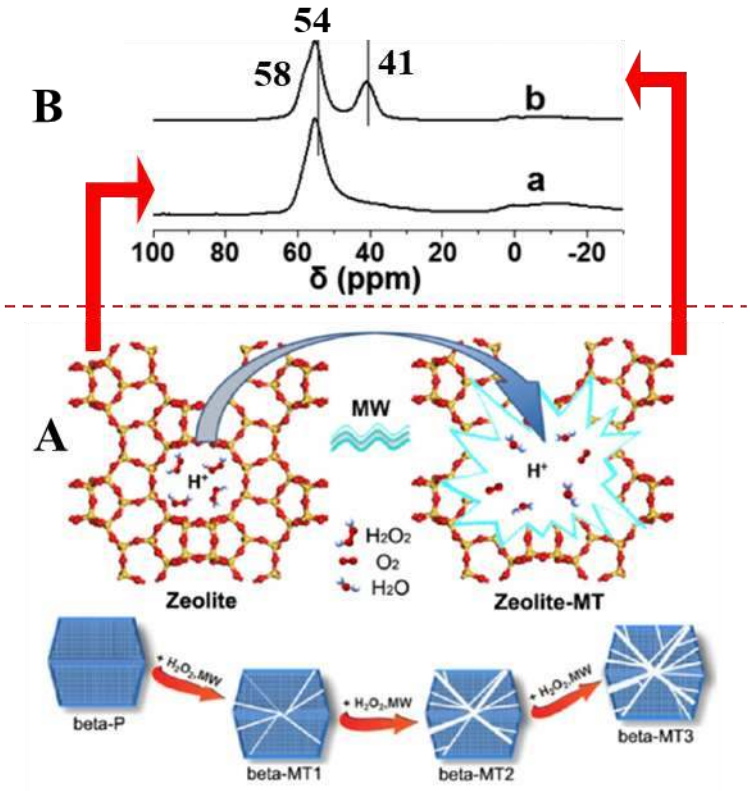

Fig. 24 Illustration of microwave-assisted H_2O_2-decomposition micro-explosion process and creation of interwoven mesopore network in the Zeolite BEA (A). ^{27}Al MAS NMR spectra (B) of BEA zeolite before (a) and after (b) microwave treatment, showing the formation of two additional tetrahedral framework ^{27}Al. Adapted with permission from ref. 297. Copyright 2016 American Chemical Society.

Local structure of layered silicates is often challenging to establish due to disorder of the sheet assemblies. Cadars *et al.*[298] reported a new protocol that combines complementary information from ssNMR on the local compositions and structures of the silicate sheets with information on medium and long-range atomic ordering provided by electron and synchrotron XRD along with support from DFT calculations. These authors were successful in determining the framework structure of a new layered silicate material, CLS-1, despite the high degrees of molecular disorder in its sheet assemblies. The diffraction based approach probed the long-range atomic order, which led to the identification of a set of possible space groups. Solid-state NMR provided local information on the framework structure, through a suite of 1D and 2D ^{29}Si, ^{13}C and ^{1}H NMR experiments from which structural models were established. All of these structures were then relaxed with quantum chemical calculations at the planewave-based DFT. Furthermore, the quality of DFT predictions of NMR parameters for the final structure found by the structure-solution algorithm and refined by DFT was

established as the right one. This protocol can be further extended to the determination of the structure of other layered silicates with low degree of crystallinity and high degree of stacking disorder.

Harris *et al*. have reported a direct hydrothermal synthesis route to prepare isomorphously substituted framework Sn heteroatoms in pure-silica chabazite molecular sieves (Sn-CHA).[299] They have adopted an integrated experimental and theoretical approach to precisely describe the primary coordination and secondary confining environments of Sn active sites in Sn-CHA. FT-IR of Sn-CHA samples saturated with Lewis bases (NH_3, CD_3CN, and pyridine) demonstrated that framework Sn atoms behave as Lewis acid sites, which were then quantified. DNP MAS NMR characterizations of Sn-CHA zeolites showed that Sn sites were incorporated into framework lattice positions, both defect-open ((HO)-Sn-$(OSi)_3$) and closed sites (Sn-$(OSi)_4$), in dehydrated state, which formed hydrated defect and hydrated hydrolysed-open sites upon exposure to ambient conditions or aqueous solution. DFT calculations on cluster models supported the experimentally measured ^{119}Sn NMR CSA parameters for Sn sites. Catalysis studies showed that Sn-CHA zeolite was active in intermolecular propionaldehyde reduction, ethanol oxidation as well as glucose−fructose isomerization.

Ivanova *et al*. have applied time-resolved *in situ* ^{13}C, ^{23}Na, ^{27}Al, and ^{29}Si MAS NMR spectroscopy to monitor the nucleation and growth of zeolite BEA catalyst under hydrothermal conditions.[300] While the ^{29}Si MAS and ^{29}Si CPMAS NMR permitted the detection of various mobile and rigid silicate and aluminosilicate species in solution as well as solid-state and monitoring of their transformation into zeolite, ^{27}Al MAS NMR was very sensitive to the interaction with inorganic and organic cations and provided information on the involvement of different cations in aluminosilicate species at different steps of synthesis. Information on the structure directing behaviour of TEA^+ was provided by ^{13}C MAS and ^{13}C CPMAS NMR spectroscopy. Solution-mediated and solid–solid hydrogel rearrangement have been distinguished for the two different synthesis procedures and insights into the mechanisms of structure-directing behaviour of TEA^+ cations in two reaction pathways have been elucidated from the NMR spectral data.

In a recent study, Oleksiak *et al*. demonstrated the organic-free synthesis of a highly siliceous faujasite zeolite (HOU-3) with spatially biased Si speciation.[301] Modelling revealed that more siliceous FAU was thermodynamically feasible and that kinetic factors govern HOU-3 formation. Solid-state NMR data suggested that the Si speciation in HOU-3 was more

discriminated than random. They have confirmed the improved hydrothermal stability and enhanced catalytic performance, for HOU-3 with Si/Al ratio of 3, relative to commercial zeolite Y.

5.1.3. Surfaces, acid sites and pore confinement

Román-Leshkov *et al*. investigated the Lewis acidity of metal sites in Beta zeolites with ^{15}N pyridine adsorption coupled with MAS NMR spectroscopy and DFT.[302] The ^{15}N chemical shift of adsorbed pyridine was found to scale with the acid character of both Lewis (Ti, Hf, Zr, Nb, Ta, and Sn) and Brønsted (B, Ga, and Al) acidic heteroatoms that are difficult to analyse with traditional methods (Fig. 25 A). Theoretical DFT calculations showed a strong correlation between experimental ^{15}N chemical shift and the calculated metal–nitrogen bond dissociation energy. Electron affinity and Mulliken electronegativity showed a linear correlation with the experimentally determined ^{15}N isotropic chemical shift values of strong and weak acidic sites (Fig. 25 B). They have concluded that pyridine adsorption and direct detection by ^{15}N CPMAS NMR spectroscopy can distinguish between Brønsted and Lewis acidity, their strength, as well as the number of framework and extra-framework metal sites in metal-substituted zeolites. More importantly, it can distinguish inactive metal oxides from metal-substituted zeolites as well as it is able to record spectra under dehydrated and hydrated conditions, emphasizing the water tolerance of these solid acids.

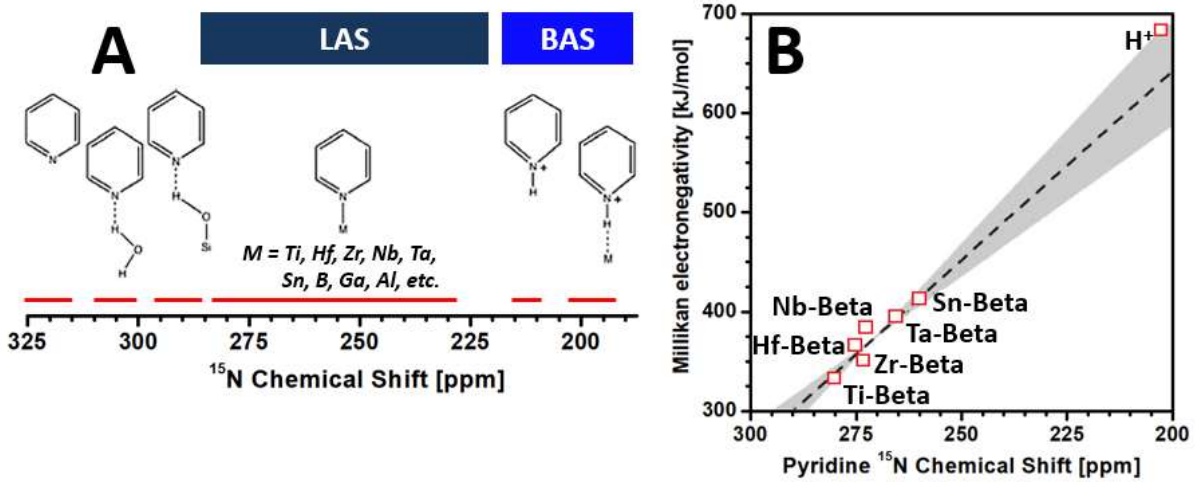

Fig. 25 ^{15}N ssNMR chemical shift scale of various pyridine binding environments for Lewis (LAS) and Brønsted acid (BAS) sites (A) and Mulliken electronegativity vs pyridine ^{15}N ssNMR chemical shift plot (B). Adapted with permission from ref. 302. Copyright 2016 American Chemical Society.

Deng *et al*. comprehensively reviewed the ssNMR methods for acidity characterization of solid acid catalysts with the help of DFT calculations to justify the correlations between experimental chemical shift values and the Brønsted/Lewis strength of acid sites in solid acid catalysts.[103] When pyridine-d_5 is adsorbed on isolated silanol groups, H-bonding normally lead to δ_H values in the range of 2–10 ppm while its adsorption on Brønsted acid sites results in the formation of pyridinium ion complexes which results in δ_H values in the range 12–20 ppm. Similarly, they have employed DFT calculations to obtain quantitative correlations between ^{1}H NMR chemical shift data and acid strength. They have reported an explicit correlation curve between the predicted δ_H and deprotonation energy values (intrinsic acid strength) for the solid acid systems (Fig. 26). Those theoretical results were in good agreement with experimental data. Deng *et al*., also combined ssNMR spectroscopy and DFT calculations for measuring the base strength of solid catalysts with pyrrole as probe.[85] These authors systematically investigated the adsorption structures, adsorption energies, and corresponding ^{1}H chemical shifts of pyrrole adsorbed on various basic zeolites with varied base strengths by using a combined NMR experiment and theoretical calculation approach. Furthermore, the study demonstrated that the zeolite confinement effect would decrease the ^{1}H chemical shift of adsorbed pyrrole by ca. 0.4 ppm.

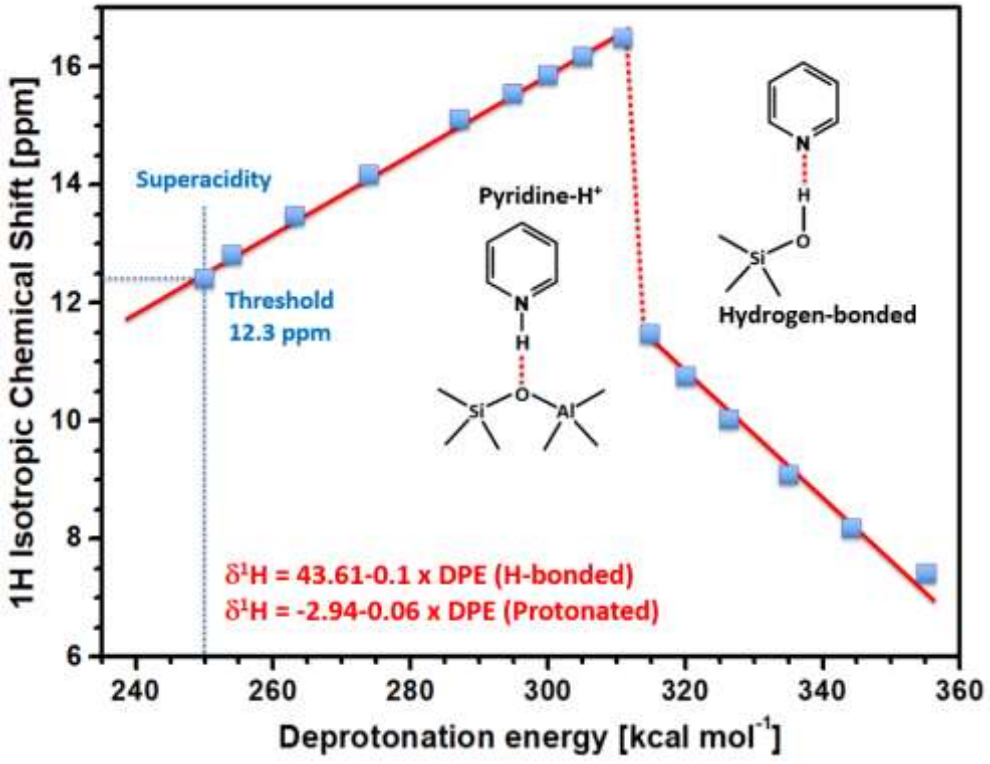

Fig. 26 Correlations between ^{1}H NMR chemical shifts and the deprotonation energy (DPE) for Brønsted acid sites in solid acids in the presence of adsorbed pyridine-d5. Adapted with permission from ref. 103. Copyright 2013 Elsevier Ltd.

DFT calculations in combination with ssNMR spectroscopy were implemented to investigate the specific aluminium location and the origin of Brønsted acid strength in Al-rich as well as Si-rich Beta zeolite catalyst.[49] The Brønsted acid strength was correlated to the Al location at the specific T-site on the zeolitic framework. DFT calculations of proton affinities, NH_3 adsorption energies and ^{1}H chemical shifts of pyridine-d5 adsorption on Al-rich H-Beta revealed that its average Brønsted acid strength was weaker than Si-rich counterpart.

Lercher *et al*. has proposed a general methodology that allows direct probing of Al distributions by NMR spectroscopic methods in zeolites with high confidence.[303] ^{27}Al single pulse MAS NMR spectra of HBEA zeolites with high Si/Al ratios were obtained at high magnetic field strengths. By combining the various field ^{27}Al MAS (Fig. 27) and high magnetic field MQMAS NMR, four different peaks were deconvoluted using the same set of quadrupole coupling constants, asymmetric parameters and relative integrated peak intensities for the tetrahedral Al peaks. They have concluded from the study that the effect of second order quadrupole interaction can be ignored and quantitative results can be derived by directly fitting the high field (~19.97 T or higher) spectra using mixed Gaussian/Lorentzian line shape with the support of DFT NMR calculations.

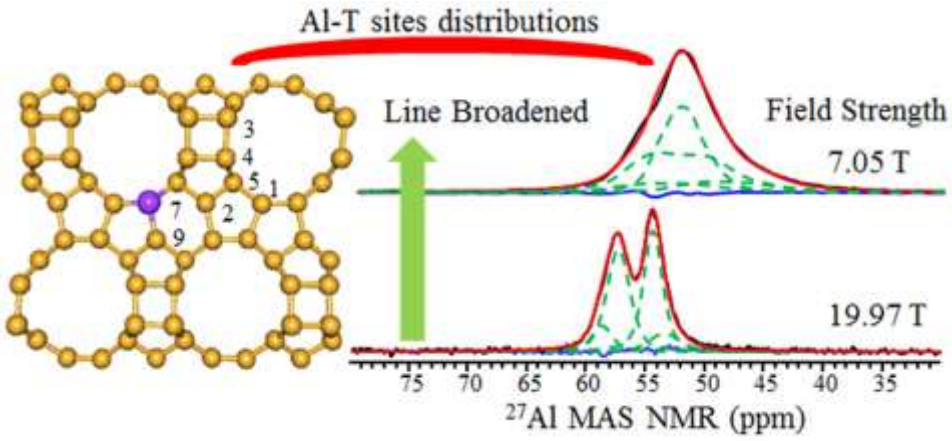

Fig. 27 ^{27}Al MAS NMR data on zeolite HBEA at various field strengths demonstrating the significant decrease in the quadrupole interactions at high field. Reproduced with permission from ref. 303. Copyright 2017 American Chemical Society.

The ^{31}P MAS NMR can be used as tool to study solid acids using trimethylphosphine oxide (TMPO), which shows chemical shift highly sensitive to the acid strength and can be introduced to porous systems in gas phase or liquid phase using solvents. In a recent report, Hayashi *et al*. studied the acid properties of ZSM-5 type zeolite by ssNMR using TMPO as a probe molecule.[68] They introduced TMPO from the gas phase at 373 K in order to increase the loading level as well as to probe almost all the acid centres. The ^{31}P chemical shifts in the range between 90 and 60 ppm are attributed to TMPO adsorbed on Brønsted acid sites, whereas the signals between 60 and 40 ppm are ascribed to other sites.

A great deal of attention has been paid to synthesise highly siliceous zeolites owing to their higher hydrothermal stability and better catalytic properties in comparison with Al-rich zeolites. Tarach *et al*. studied the hydrothermal stability and catalytic performance of desilicated highly siliceous zeolite ZSM-5.[304] The concentration of Brønsted and Lewis acid sites was measured in quantitative IR studies of pyridine adsorption, while their strength was determined in pyridine thermo-desorption experiments and low temperature carbon monoxide adsorption. The ^{27}Al MAS NMR measurements delivered information on the status of Al atoms in both native and desilicated zeolites as well as on the changes of this status upon the steaming process.

The ^{2}H NMR spectroscopy has become a method of choice for the investigation of molecular dynamics in molecular and solid-state systems. Lalowicz *et al*.[305–309] have applied ^{2}H NMR and IR spectroscopy along with spectral simulations to derive the confinement effect and molecular dynamics of methanol-d_4 and D_2O inside the zeolite faujasite cages. Water confined in the NaX and NaY zeolites indicated that the presence of sodium cations in zeolite framework is important for observed mobility of water molecules and stability of water clusters. On the other hand, by measuring the temperature-dependent relaxation of deuterium in the range between 20 and 170 K, it was possible to distinguish gas phase, liquid-like, and immobilized methanol-d4 in zeolite cages.

5.1.4. Applications

Wang *et al*. combined experimental NMR and theoretical investigations to gain new insights into the hydrocarbon-pool chemistry of the methanol-to-olefin (MTO) reaction over zeolite H-ZSM-5.[310] They have co-feeded methanol and benzene over zeolite and detected active intermediates such as various cyclopentenyl cations and the pentamethylbenzenium ion. They

have demonstrated the operation of an aromatics-based paring mechanism for the formation of propene, which was also theoretically supported by DFT calculations.

By combining FT-IR and ssNMR spectroscopies along with other techniques, Raja *et al.*[311] have outlined the crucial differences in diffusion modes and molecular interactions of active sites within solid-acid catalysts based on MFI and FAU topologies. Such understandings can be utilized in the industrial production of ε-caprolactam (precursor to Nylon-6) under low-temperature, liquid-phase conditions.

The transformation of biomass into fuels is of great industrial relevance for green chemistry reasons. Sels *et al*. have demonstrated the cooperative catalysis for multistep biomass conversion with bifunctional Sn/Al Beta zeolite using a combined spectroscopic approach.[312] Lewis acid Snβ-type zeolites with varying amounts of Brønsted acid Al in the framework were synthesized by partial dealumination of β zeolite, followed by grafting of Sn centres (Fig. 28 A). FT-IR and ^{27}Al MAS NMR demonstrated the presence of Brønsted acid framework Al^{IV} as well as tetrahedral Lewis acidic Sn^{IV} sites (Fig. 28 B). Zeolites containing moderate amounts of framework Al showed the highest catalytic activity, validating the cooperative effect of Lewis Sn^{IV} and Brønsted Al^{IV} acid sites.

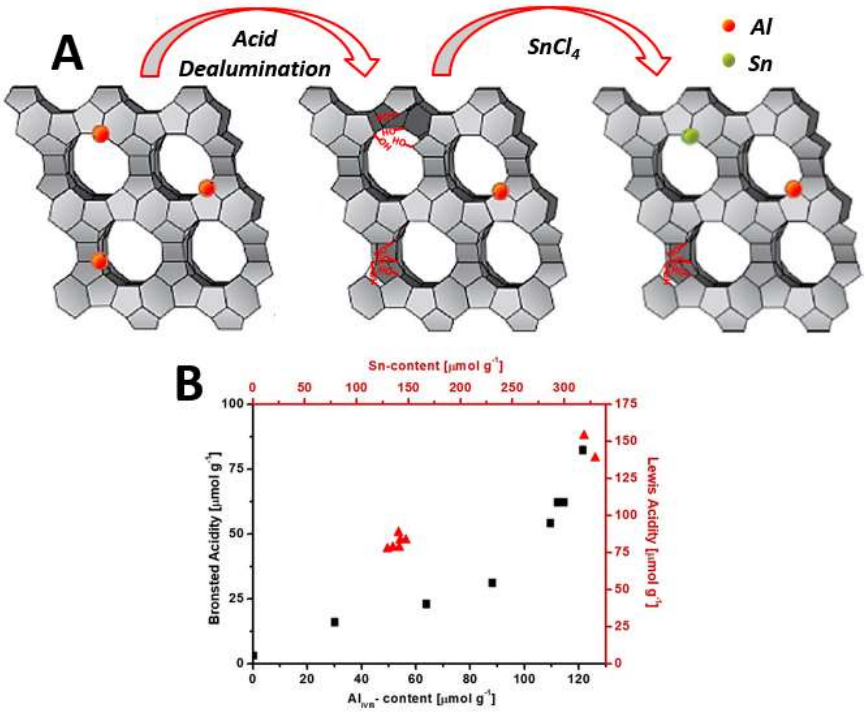

Fig. 28 Schematic representation of the synthesis of Sn/Al zeolitic material (A) and a plot of Brønsted and Lewis acidity per weight of material, obtained with quantitative FT-IR probed

pyridine sorption, as a function of the Al^{IV} (bottom axes) and Sn content (top axes) of the materials (B). Adapted with permission from ref. 312. Copyright 2015 American Chemical Society.

Hunger *et al*. also investigated Sn-Beta zeolites as Lewis acid catalysts for the ring-opening hydration of epoxides prepared by two-step post-synthesis strategy.[313] Solid-state ^{119}Sn MAS NMR and FT-IR spectroscopy revealed that most Sn species have been successfully incorporated into the framework of Beta zeolite and exist as isolated tetrahedral Sn^{IV} in open arrangement creating strong Lewis acidity (Fig. 29 A). The signal at −420 ppm observed for Sn-Beta was due to framework Sn^{IV} in open arrangement, while no Sn^{IV} in closed arrangement was detected at −443 ppm (Fig. 29 B). More importantly, hydration of tetrahedrally coordinated open arrangement Sn species resulted in an octahedral Sn^{VI} species and seen at −685 ppm. The catalytic activity study in the ring-opening hydration of epoxides to the corresponding 1,2-diols showed remarkably high selectivity at near ambient and solvent-free conditions. They have also reported recently a novel approach for the characterization of Lewis acidic solid catalysts by ssNMR spectroscopy. Acetone-2-^{13}C, trimethylphosphine oxide (TMPO) and ammonia were applied as probe molecules for ssNMR investigations of Lewis acid sites on γ-Al_2O_3, TiO_2/anatase and lithium-exchanged zeolite Na-Y.[314]

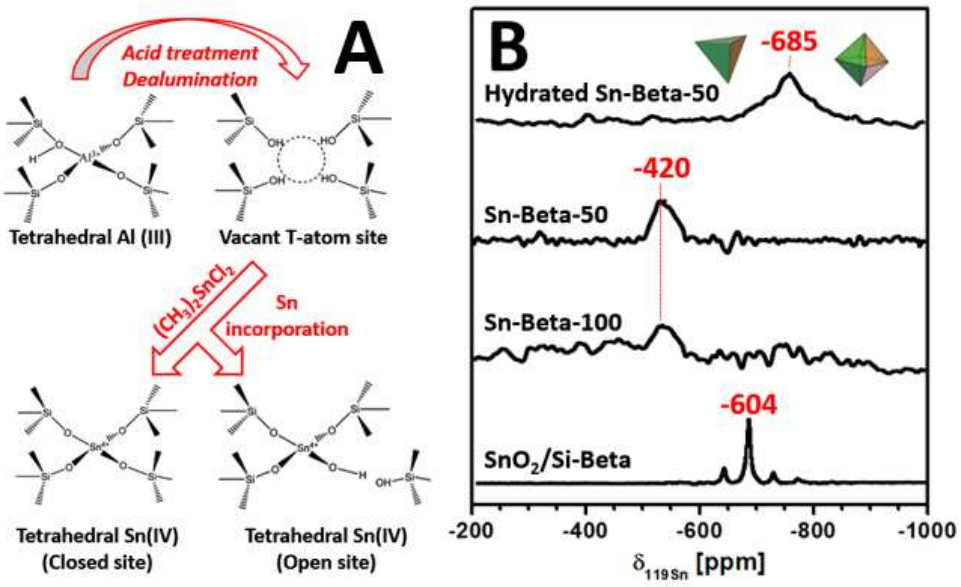

Fig. 29 Schematic representation of the incorporation of tetrahedrally coordinated Sn(IV) species into Beta zeolite (A) and ^{119}Sn MAS NMR spectra of dehydrated and hydrated Sn-

Beta and SnO_2/Si-Beta samples. Adapted with permission from ref. 313. Copyright 2014 American Chemical Society.

Dai *et al*. demonstrated for the first time the formation of the tert-butyl cation during isobutene conversion on zeolite H-ZSM-5 by ssNMR spectroscopy supported by DFT calculations.[315] ^{1}H and ^{13}C MAS NMR studies as well as the theoretical calculations indicated that the *tert*-butyl cation formed on zeolite H-ZSM-5 by conversion of isobutene could be captured with ammonia. Furthermore, they did not observe any signals due to *tert*-butylammonium ions in the reaction between ammonia and isobutene in the absence of Brønsted acidic sites.

The reaction mechanism of solid-acid catalysed phenol alkylation with cyclohexanol and cyclohexene in decalin has been studied using *in-situ* ^{13}C MAS NMR spectroscopy and the Amsterdam Density Functional (ADF-2014) package.[316] *In-situ* ^{13}C ssNMR spectroscopy can probe, at a molecular level, the reaction pathways for this type of solid-acid catalysed reactions, at high temperature and high pressure conditions. They have established that intramolecular rearrangement of cyclohexyl phenyl ether is a minor pathway to cyclohexylphenols and alkylation occurs via a stepwise route initiated by olefin protonation.

Radhakrishnan *et al*. investigated the pore mouth catalysis in etherification of β-citronellene with ethanol on zeolite Beta using FT-IR and ssNMR spectroscopy.[317] *In-situ* FT-IR investigations using pyridine revealed that access to the interior of zeolite Beta crystallites were not blocked by pre-adsorption of 2,4,6-collidine. While *in-situ* ^{13}C Hahn-echo and $^{1}H–^{13}C$ CPMAS NMR characteristics were used to discriminate between molecules freely moving in liquid phase outside the zeolite and molecules adsorbed inside zeolite pores and in pore mouths. Preferential adsorption of ethanol in zeolite pores dictates the etherification reaction of β-citronellene molecule from the external liquid phase in a pore mouth and prevents side reaction.

Moreno-Gonzalez *et al*. have tested two copper zeolites with different framework topology for the selective catalytic reduction of exhaust gas from diesel vehicles.[318] They have studied the interaction of ammonia with zeolite Cu-SSZ-13 (CHA topology) with a uniform distribution of Cu^{2+} sites prepared in one pot and a conventional Cu-ZSM-5 (MFI topology) for comparison. *In-situ* EPR and ssNMR spectroscopies combined with DFT calculations have provided experimental evidence for the formation of various ammonia containing copper species under different conditions. DFT calculations along with 1D and 2D ^{15}N and

^{1}H MAS NMR spectroscopy of ^{15}N enriched ammonia adsorbed on the Cu zeolites provided direct information on the reduced Cu^{+} sites formed, as well as on the $^{15}NH_4^{+}$ cations formed on the Brønsted acid sites which shed light on the selective catalytic reduction reaction mechanism. Cu-SSZ-13 zeolite has also been used in SCR reaction.[319]

Ab initio calculations (mainly at the DFT level, though some examples of correlated post-Hartree-Fock methods exist too) are often used to supplement the vibrational spectroscopic characterization, supporting the peak assignments. Many examples published prior 2015 are reviewed and the role of probe molecules is also described, with particular attention to CO, CO_2 and NO used to investigate the surface acid sites in different zeolites.[320]

Very recently, Knott *et al*. have reviewed the experimental and computational progress in the modelling of MFI zeolites, concentrating on the catalytic applications, and underlying again the role of DFT calculations in the interpretation of vibrational spectra, as well as in the definition of small size (cluster) models of the reacting systems for the investigation of reaction mechanisms.[321]

The theoretical shift of the stretching frequency of NO and CO molecular probes was used in conjunction with FT-IR experiments to characterize the adsorption sites in some copper-exchanged zeolites and zeotypes (SAPO).[322] Similarly, the comparison of theoretical and experimental CO frequencies was used to describe the cationic sites in high silica USY zeolites decorated with alkali metals[323] and in FER systems including Ca^{2+} cations.[324] In both cases, the modification of the probe stretching frequency could be correlated to the structure of the surrounding material, in particular the number and position of silanol groups, through the modelling of suitable clusters.

Of particular interest is the use of DFT calculations to identify some representative vibrations in the low-frequency pseudolattice region, involving ring oscillations and quite difficult to interpret in the experiments: modelling of suitable clusters and of periodic frameworks allowed to describe in detail the ring vibrations in FER, MOR and HEU zeolites, with a great improvement in the spectra interpretation.[325] A similar approach had been used in to identify the 5-1 ring vibrations in spectra recorded for MOR zeolites after heavy metal cations immobilization.[326]

Because of the extensive use of zeolites in catalysis, in many papers a combination of theoretical and experimental techniques is applied to describe reaction mechanisms: most of such applications lie outside the scope of this work, but in some recent applications FT-IR

spectra have been interpreted with the aid of DFT simulations, leading to suitable chemical models of interacting systems, for instance propene in potassium-FER zeolite,[327] or acetic acid and methanol in H-Beta zeolite.[328] The photocatalytic degradation of methylene blue catalysed by a Ni(II) hexa-aza complex embedded in Y zeolite was followed by a series of spectroscopic measurements, supported by DFT calculations on model systems, describing both the neat and the encapsulated complex.[329]

In an outstanding work recently published,[330] different spectroscopic and diffraction techniques were used in conjunction with DFT calculations to describe the self-organization of perylene-diimide dyes inside a zeolite L: in this theoretical-experimental approach, the supramolecular organization in the confining matrix was described by modelling the atomistic structure and comparing the simulated structure and spectra with the measurements (Fig. 30).

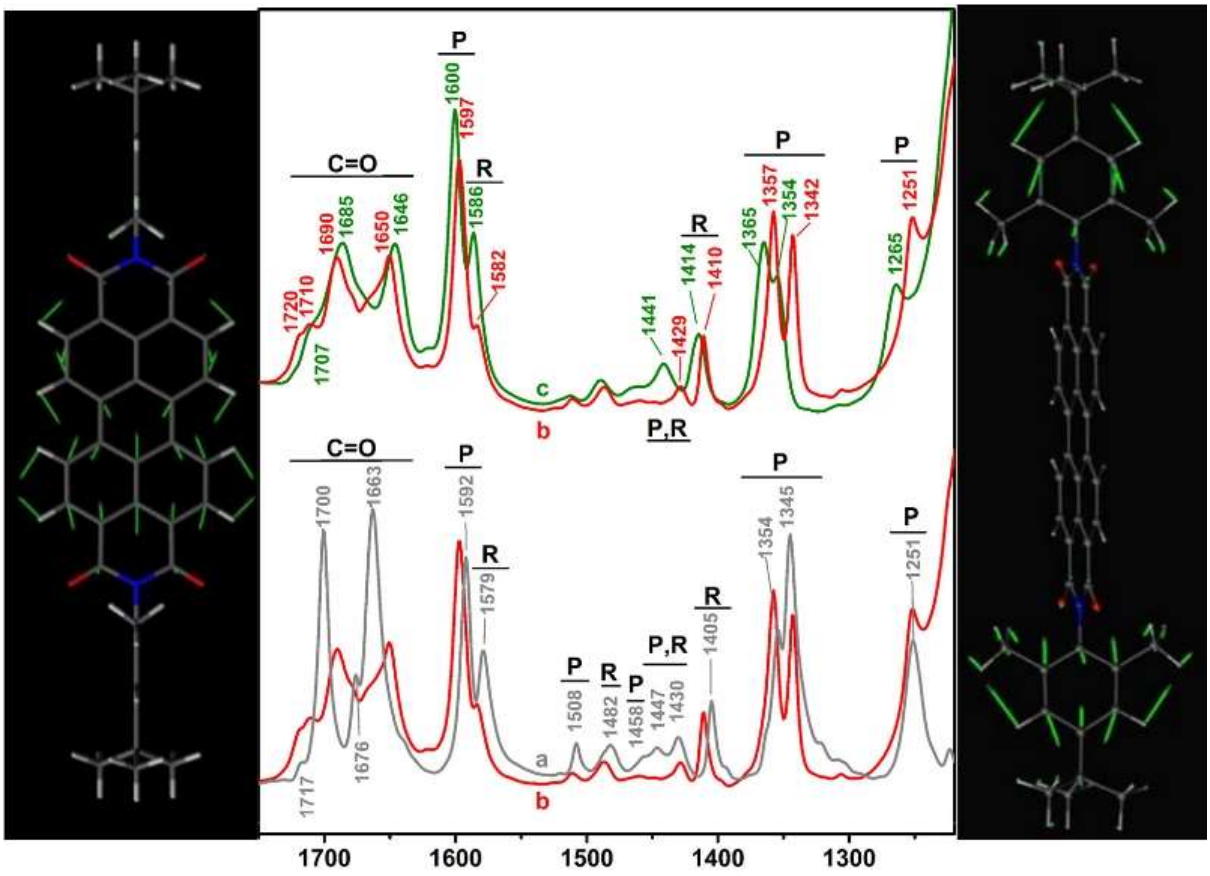

Fig. 30 Center: FT-IR spectra of perylene dye embedded in zeolite L in solid state (gray), degassed (red) and re-hydrated (green). Left and right panels: sketch of two normal modes computed at DFT level for isolated dye molecule, used for the assignment of the IR bands. Adapted with permission from ref. 330. Copyright 2018 American Chemical Society.

When coupled to NMR experiments, ab initio calculations are usually employed to reproduce chemical shifts and chemical shift anisotropies, to be compared to the experimental values in different conditions, often with the support of suitable probes. Many nuclei have been considered by this approach: ^{119}Sn chemical shift anisotropies were computed at the DFT level on model clusters to elucidate the interaction sites of tin in CHA zeolites;[299] ^{13}C CPMAS NMR experiments were interpreted with the aid of multiscale theoretical simulations to investigate the solvent effect on the activity of acetone probe in ZSM-5;[76] analogously, pyrrole was used as ^{1}H NMR probe to test basic sites on catalytic materials, by comparing a number of experimental data on different zeolites with DFT computed chemical shifts for pyrrole on a generic 8T zeolite model.[85]

A combination of DFT and MAS NMR spectroscopy on ^{29}Si nuclei was used to study the structural and chemical modifications induced by Ge/Si substitution in zeolite Beta: in this work, it was possible to discriminate the different substitution sites thanks to the accurate calculation of chemical shifts in different suitable model clusters;[331] the structure of a newly synthesized AST zeolite was determined by ^{14}N NMR spectroscopy, by reproducing the NMR parameters at the DFT level, after the theoretical optimization of the material, and demonstrating the presence of weak CH...O hydrogen bonds inside the structure.[332]

Zheng *et al*. have reviewed the use of ^{31}P NMR spectroscopy for the study of acid sites in various liquid and solid catalysts, including several zeolites, with the support of DFT calculations: in this case, instead of reproducing the NMR tensors, the calculations were mainly used to estimate the acid strength to be correlated with the measured magnetic spectra.[69]

A comprehensive review was recently published about the studies employing DFT calculation of chemical shift tensors to support the assignment and the analysis of ^{27}Al NMR spectra: a variety of Al containing solids were mentioned in this work, among which different zeolites, underlying the potential utility of this combined approach.[333]

5.2. Zeo-type materials

In the early 1980, a new class of microporous crystalline materials, aluminophosphates (AlPOs), different in nature with respect zeolites that are silicates or aluminosilicates, but

with similar textural and shape-selectivity properties, have been synthesized.[334] ALPOs cover a wide range of different crystalline structures: some analogous to traditional zeolites such as SAPO-34 (CHA structure) or SAPO-37 (FAU structure) and others with unique structures. The AlPOs framework allows introducing isolated active centres via isomorphous substitution of metal-ions into the alternating AlO_4 and PO_4 framework tetrahedra during synthesis generating a diverse range of active sites (solid-acid and/or redox centres).[335] Al(III) and/or P(V) can be replaced by Si(IV) to form SAPO-n materials and by other metals to form MeAPO-n or MeAPSO-n materials. Owing to the availability of a large-range of metal ions that could be effectively incorporated into a diverse-range of AlPOs architectures creating Brønsted acids or redox sites and containing wide-range of pore apertures, these microcrystalline materials have been widely used as acid or redox heterogeneous catalysts. Among silicoaluminophosphates (SAPOs), SAPO-34 has been investigated extensively due to its well-established industrial relevance in the methanol-to-olefin (MTO) acid catalysed process (100 % methanol conversion and > 90 % selectivity to C_2-C_4 light olefins).[336] The catalytic activity of microporous crystalline materials in MTO reactions is due to the presence of Brønsted acid sites, SiO(H)Al, within their channels and cavities. The Brønsted acidity in SAPOs is produced by the insertion of Si(IV) at the P(V) site, which leads to the formation of negatively charged frameworks that are balanced by protons attached to Si-O-Al bridges; this mechanism is denoted SM2. The substitution of Si(IV) for Al(III), SM1, is another possible mechanism of Si insertion; however, this would lead to the formation of Si-O-P bridges, which are energetically unfavourable as suggested by a computational study on SAPO-5 and have never been observed experimentally. The double substitution of neighbouring Al(III) and P(V) by two Si atoms has been often proposed for the Si insertion; this third mechanism, SM3, is responsible for the formation of Si islands, e.g., silicate-type patches with variable extension, within the AlPOs frameworks. The silicon content can address the substitution mechanism generating different SAPO structures. The three mechanisms are represented in Scheme 1.[337] The local structure of Brønsted acid sites in SAPOs is formally similar to that of classical zeolites.

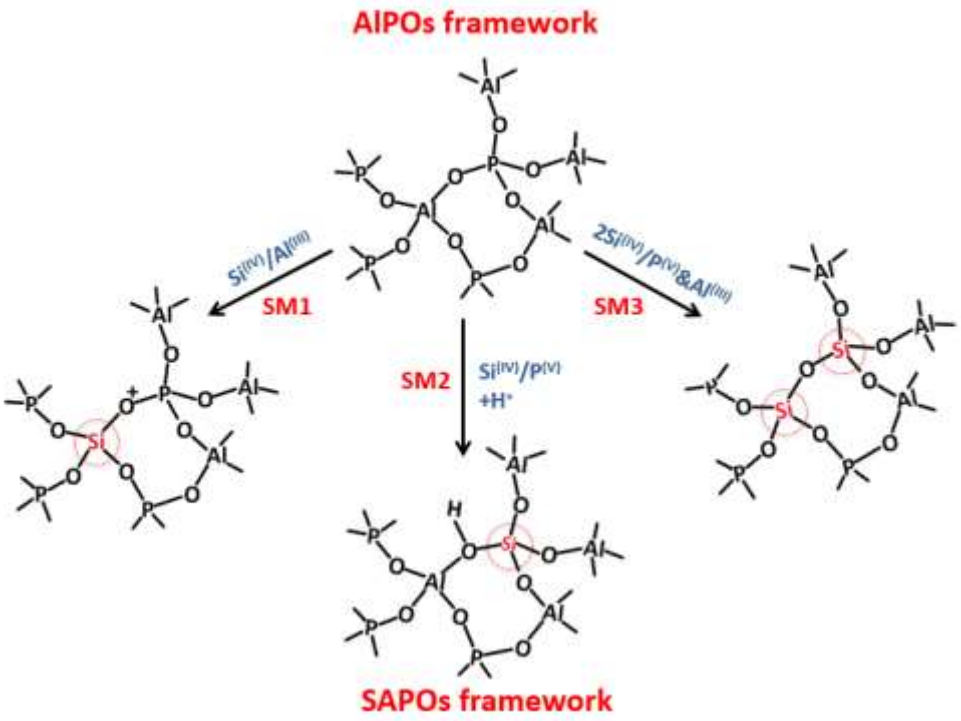

Scheme 3 *Adapted with permission from Pastore et al. Annu. Rev. Mater. Res.*, 2005, **35**, 351–395. *Copyright 2005 Annual Reviews.*

The nature and the strength of the acid sites in the SAPOs can be assessed coupling FT-IR spectroscopy with (^{1}H, ^{29}Si, ^{31}P and ^{27}Al) ssNMR. In particular, the acid strength of Brønsted sites can be studied by FT-IR spectroscopy using adsorption of probe molecules with basic character, such as ammonia or pyridine, or by measuring the temperature at which these molecules are desorbed (temperature programmed desorption (TPD) measurements).[338] However, these techniques and the use of strong basic probe molecules do not allow discerning among families of Brønsted sites with small differences in acid strength; in this case the use of probe molecules with weaker basicity such as CO is compulsory. In particular, the CO adsorption at 100-110 K on acid materials produces a downward shift of the stretching mode of O-H (ν_{OH}) due to the interaction of the acid site by H-bond with the CO molecules. The measure of the ν_{OH} shift upon formation of the OH….B adducts represents a classical method to estimate the acidity of Brønsted sites.[320,339–341] To achieve information on the coordination of framework constituent of AlPO or SAPO architectures, ssNMR is widely used, in fact different chemical shifts are observed by changing the coordination of Al or P from tetrahedral to octahedral.

SAPO-34 catalysts have been deeply characterized by FT-IR and ssNMR. In the O-H stretching region of FT-IR spectra (Fig. 31 A), calcined SAPO-34 displays two intense bands with maxima at 3630 and 3600 cm^{-1} assigned to the stretching mode of Al(OH)Si Brønsted acid sites in the O4 (3630 cm^{-1}, OH_A) and O2 (3600 cm^{-1}, OH_C) structural configurations of the CHA framework.[342,343] The two acid sites have been also evidenced by ^1H MAS NMR spectroscopy (Fig. 31 B): a signal at around 4 ppm, associated with Brønsted Si(OH)Al groups, is present and after deconvolution, two components at 3.6 and 3.9 ppm can be identified, corresponding to the two protons in the CHA framework.

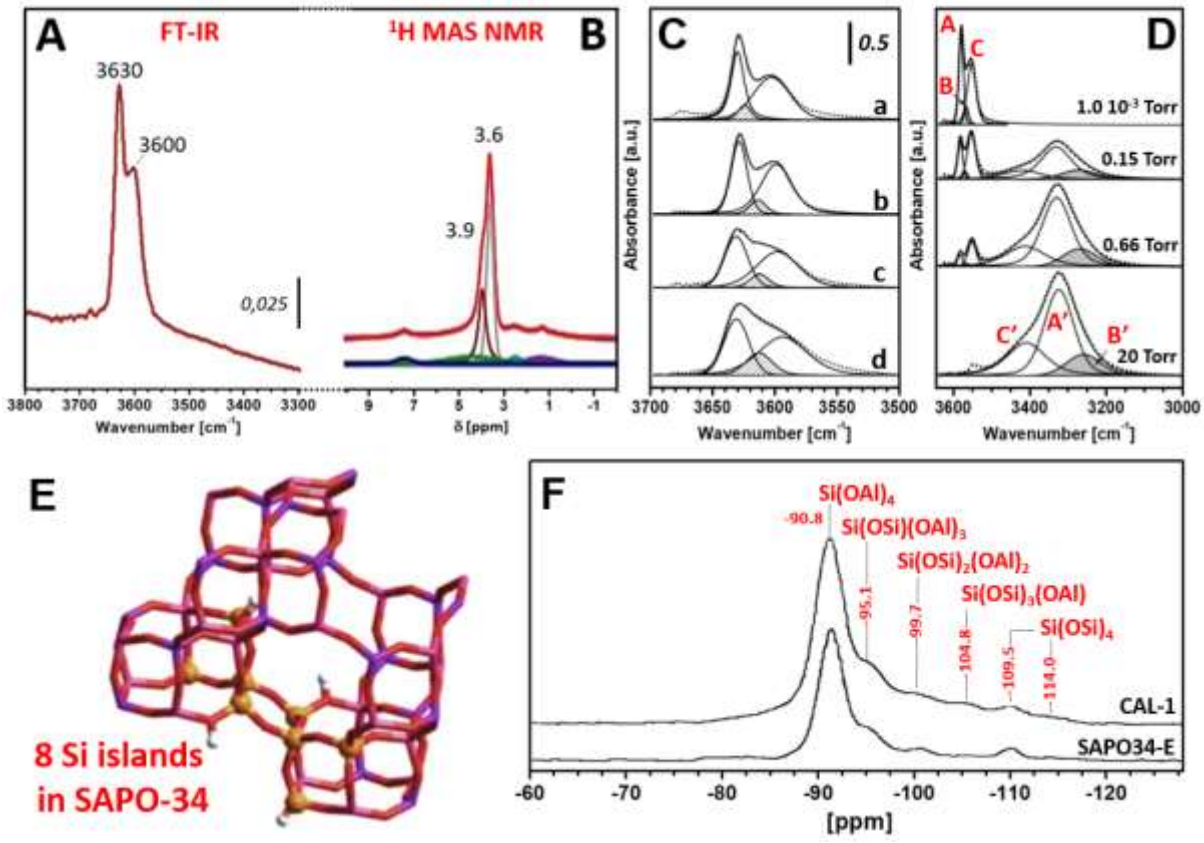

Fig. 31 (A) FT-IR spectra in the O-H stretching region of a calcined microporous SAPO-34; (B) ^1H MAS NMR spectra of a SAPO-34 sample similar to (A); (C) SAPO-34 samples (a to c) of different origin and CAL-1 (d), a silicoaluminophosphate with CHA structure, as described in ref. 342; (D) sample (b) under different CO pressures; (E) a representation of a silicon island in a SAPO-34 structure, after substitution of 4 couples of Al/P atoms with 8 silicon atoms as described in ref. 337; (F) ^{29}Si CP MAS NMR of selected samples of frame (C). Adapted with permission form ref. 337 and 342. Copyright 2005 Annual Reviews and Copyright 2007 American Chemical Society.

Clear-cut proofs of the presence of a third type of Brønsted acid sites (named OH_B) were found by FT-IR study of weak probe molecules: these sites, absorbing at 3625 cm^{-1}, have been described in literature by a multi-peak curve-fitting (Fig. 31 C and D).[342] The validity of this curve-fitting procedure was checked using the empirical correlation proposed by Makarova *et al*. based on the increase of the extinction coefficients of OH groups involved in H-bonding.[339] Brønsted OH_B sites were found more acid with respect OH_A and OH_C by studying the shift of the stretching O-H mode due to the CO adsorption at 110 K (Fig. 31 D): the downshift observed for OH_B Brønsted sites was ca. 331 cm^{-1}, higher than those found at 277 and 145 cm^{-1} for OH_A and OH_C, respectively. The OH_B were found even more acid than the protons of the H-SSZ-13, the zeolitic homologues ($\Delta\nu_{OH}$ = 316 cm^{-1}).[344] The nature of these particular acid sites was explained in terms of Si sites present at the borders of silica islands (Fig. 31 E), having a local environment similar to that of Brønsted sites in zeolites; this hypothesis was confirmed by a detailed comparison of the data obtained on samples with different Si loadings and by ^{29}Si CP MAS NMR analysis (Fig. 31 F). It is of note that ^{1}H MAS NMR could not directly detect the OH_B sites because of the strong overlapping with the other two proton signals, whereas ^{29}Si CP MAS NMR proved their possible location. Again, this enlightens the relevance of adopting a combined FT-IR/ssNMR and theoretical study for an in-depth characterization of solid systems with high structural complexity.

The position and the chemical environment of copper ions embedded in SAPO catalysts were characterized with a combination of IR spectroscopy and DFT calculations, employing different probe molecules: NO was used to describe the structure of Cu-SAPO-34, compared to Cu-SSZ-13, and the comparison of experimental and theoretical frequencies indicated the presence of dimeric copper oxo ions;[322] CO was also used in a combined FT-IR and theoretical investigation of Cu-SAPO-34 to locate the copper sites, depending on the preparation methods.[345] In both these studies, the calculations were used to assign the vibrational frequencies of the probe/copper complexes, using models of the different conformations.

On the other hand, DFT calculations were used in conjunction to FT-IR measurements to elucidate the mechanism of NO oxidation in Cu-SAPO-18 catalyst: in this case, the role of the theoretical study was related to the modelling of the process, rather than to the spectroscopic characterization.[346]

5.3. Mesoporous materials

Mesoporous silica has received much attention due to its well-defined structural order, high surface area, and tuneable pore diameter. Although the first successful report patented on the synthesis of mesoporous silica happened in 1970's, the effective introduction to scientific community appeared in 1992 from Mobil research and Development Corporation. Those ordered mesoporous silica materials (MCM type) had pore diameter up to 10 nm. However, mesoporous silica systems with larger pore diameter up to 30 nm started to appear in 1998 and were called Santa Barbara Amorphous (SBA type).

Unlike microporous materials, mesoporous materials have the advantage that its larger ordered pore system can be utilized for a variety of applications such as gas storage, separation, and heterogeneous catalysis as well as drug delivery. Moreover, its inner walls could be functionalized to yield single-site, chiral and catalytically active centers, which could be determined using FT-IR and multi-nuclear MAS NMR spectroscopy. These techniques opened up the prospect of understanding how the catalytic effects are achieved in these porous systems or how a molecule is confined inside the pores. Alonso and Marichal have recently reviewed the application of ssNMR spectroscopy on the study of formation mechanisms, the characterisation of structures, textures, surfaces and interfaces, functionalisation, dynamic properties and structure–reactivity correlations.[347]

5.3.1. Surfaces, acid sites and pore confinement

Study of the formation of mesoporous material is of great importance in order to tailor the pore size to specific uses and to maximize the stability. When a non-ionic triblock co-polymer surfactants of the type $EO_{106}PO_{70}EO_{106}$ (Pluronic F127), was used in a self-assembled micellar approach, a 3D cubic Im3m space group arranged mesoporous silica material was formed (SBA-16).[348,349] By the careful variation on the amount and ratios between reactants such as surfactant F127, water, HCl, butanol and TEOS, it was possible to control the texture of SBA-16. The synthesis is driven by a self-assembling of the co-polymer in micelles, which minimizes the contact of its hydrophobic parts with the water solution and leads to the formation of the silica inorganic structure by hydrolysis of tetraethoxysilane (TEOS) at the water/polymer interface. Bisio *et al*. reported a combined application of FT-IR

and ssNMR spectroscopy, to assess the interactions occurring between the triblock copolymer and the SBA-16 siliceous framework at different hydration levels.[350]

They have employed multi-nuclear multi-dimensional MAS NMR experiments to probe the organic-inorganic interfaces formed by the copolymer and silica framework in as-synthesized SBA-16. Heteronuclear correlation (HETCOR)[351] experiments, based on proton to silicon or proton to carbon dipolar couplings, are sensitive concurrently to the atomic distances of interest and to the co-polymer segmental mobilities. The presence of strong surface interactions between the block-copolymer and various framework silicon sites were hinted by the overlapping cross peak pairs (in 2D ^{1}H-^{29}Si HETCOR data) generated between protons of the alkoxy units and silicon nuclei of the as-synthesized SBA-16. Interpenetration of the F127 polymer blocks into the inner silica walls were confirmed by the correlation peaks appeared between Q^3 and Q^2 silicon sites and methyl protons of co-polymer at around 1 ppm. Such cross peaks were absent in dehydrated SBA-16 sample hinting reorganization of the PEO and PPO blocks of the copolymer. In addition, 2D ^{1}H-^{13}C HETCOR data also revealed the location and role of water in the formation and stabilization of polymer-silica interfaces (Fig. 32). Moreover, the organization of PEO and PPO blocks at the interface and their dynamics controlled by the interfacial water was also revealed. Strong hydrogen bonding interactions between copolymer and silica framework were confirmed by the appearance of cross-peak between the PEO units (^{13}C at 70.7 ppm) and the ^{1}H signal of hydrogen bonded silanols at 5.7 ppm. Variable temperature FT-IR studies confirmed the H-bondings between SiOH and etheric oxygen atoms of co-polymer. Such integrated approach using multiple characterization tools helps one in understanding the formation of mesoporous materials and forecasting their properties.

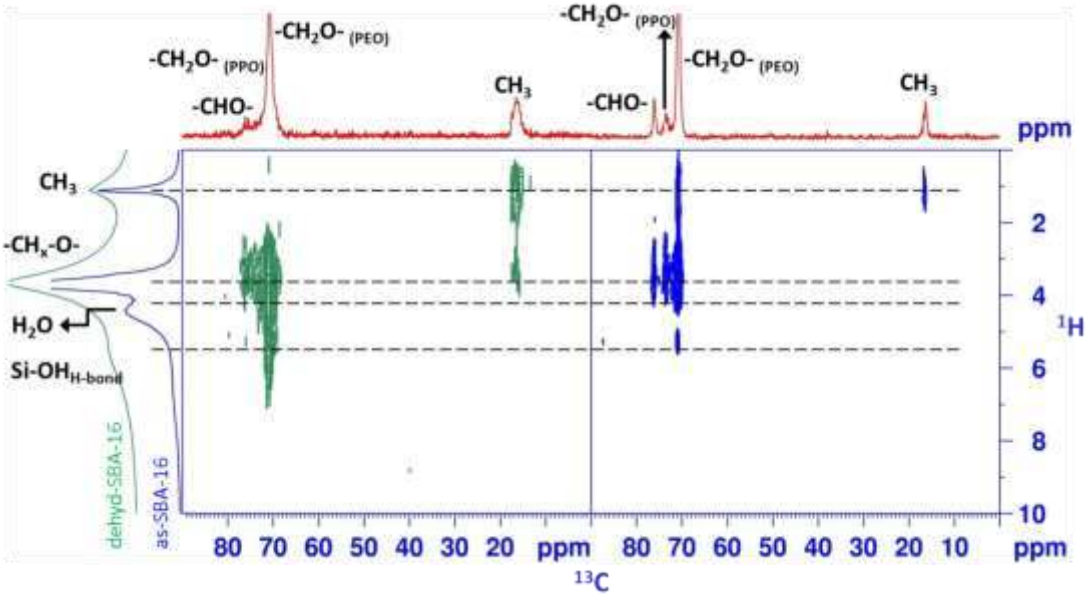

Fig. 32 2D ^{13}C–^{1}H HETCOR NMR spectra of as synthesized (right) and dehydrated (left) SBA-16. ^{1}H MAS NMR spectra is on the ^{1}H axis while the ^{13}C projections on the ^{13}C axis (top). Adapted with permission from ref. 350. Copyright 2012 The Royal Society of Chemistry.

Yasmin and Muller have applied supercritical fluid approach to prepare alkyl bonded mesoporous MCM-41 silica materials with higher surface coverages.[352] The degree of bonding and cross-linking of the alkylsilanes was determined by ^{29}Si NMR spectroscopy, and the application of FT-IR and ^{13}C NMR spectroscopy revealed the conformational behaviour and mobility of the bonded alky chains.

Cattaneo *et al*. prepared organosulfonic modified SBA-15 silicas for catalytic applications in organic reactions.[353] Catalytic activity of the propylsulfonic pendants in the ordered mesostructured of SBA-15 was restricted to 20 mol %. The extent of the propylsulfonic functionalization into the silica materials was monitored through ^{29}Si ssNMR spectroscopy. Above 50 mol % of organic functionalization, a progressive modification of the SBA-15 hexagonal mesoporous structure was observed which suggested an inhomogeneous distribution of the organic pendants. From ^{1}H and ^{13}C MAS NMR, it was shown that a full conversion of the -SH groups to $-SO_3H$ was possible only at low functionalization degrees while at higher degrees the formation of S-S bridges was the predominant mechanism.

Reid and Crudden were successful in producing stable molecular chirality within the walls of periodic mesoporous organosilicas via self-assembly.[354,355] Their chiral PMOs showed strong

circular dichroism signals that were completely preserved after post-treatment of the solid-state material favouring the conformationally locked chiral PMO. Solid state ^{13}C CPMAS NMR confirmed the presence of the chiral dopant embedded within the PMO materials while the ^{29}Si MAS NMR signals in the T-site region indicated a high degree of condensation in the final material.

Azhati *et al*. recently demonstrated that ordered highly zeolitized mesoporous materials can be obtained via gradient acidic assembly growth strategy with mixed template synthesis approach.[356] The resultant highly zeolitized mesoporous aluminosilicate SBA-16, composed of the intergrown zeolite subcrystal particles, exhibited high surface area and pore volume, typical channel of MFI framework and uniform mesopore (~5.7 nm). They have used multi-technique approach to characterize the material including solid-state ^{29}Si and ^{27}Al MAS NMR and FT-IR spectroscopies. FT-IR spectra of adsorbed pyridine were used to calculate the relative concentration of the Brønsted and Lewis acid sites from the intensity of the PyH^+ and PyL bands.

Recent investigations by Peemoller *et al*. utilized proton NMR to model the chemical shift averaging, due to the making and breaking of hydrogen bonds as water molecules move on the mesoporous MCM-41 surface, both as a function of hydration and temperature.[357,358] Various hydrogen bonding configurations of water on MCM-41 are shown in Fig. 33. They identified two water groups of which one makes up 37–42 % of the total water hydrating MCM-41 and was assigned to H-bonded surface OH group adsorption sites. While the water group making up 58–63 % of the water on the surface was assigned to Si–OH groups. It was found that the water groups maintain these fractions over all temperatures (over a temperature range of 200–325 K) and hydrations, with minor deviations.

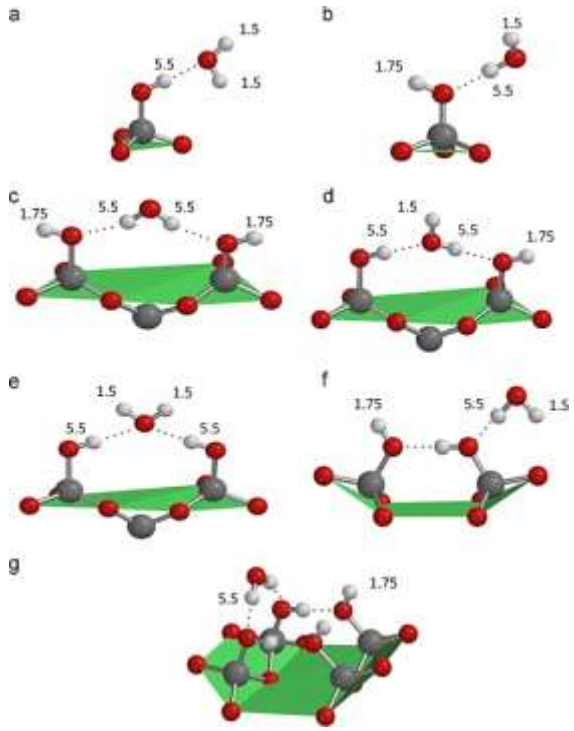

Fig. 33 The various hydrogen bonding configurations of water, a–g, to the surface silanols considered in the chemical shift averaging model. Dotted lines represent hydrogen bonds. All protons involved in hydrogen bonding are assumed to take the same isotropic chemical shift value of 5.5 ppm. Protons of water molecules and OH groups not involved in hydrogen bonding were assigned a value of 1.5 ppm and 1.75 ppm, respectively, at 293 K. Reprinted with permission from ref. 357. Copyright 2013 Elsevier Ltd.

In the work of Grünberg *et al*. melting of naphthalene confined in mesoporous silica MCM-41 with a pore width of 3.3 nm was studied using ^{2}H solid-echo NMR in the temperature regime from 180 to 250 K.[359] Melting point of the naphthalene molecules confined in mesoporous silica MCM-41 showed a reduction of 152 K. The line shape changes in the melting region were simulated with models and found out that a relatively narrow distribution of melting points of the naphthalene molecules inside the pores, is indicative of a well-defined organization of the naphthalene molecules within the pore structure.

Kamarudin *et al*. utilized FT-IR and ssNMR for probing the influence of Al loading in mesoporous silica nanoparticles (MSN) for the evaluation of Ibuprofen adsorption and release.[360] Acidity in Al-MSN samples was monitored using pyridine pre-adsorbed FT-IR spectroscopy (Fig. 34 A). The bands at 1545 cm^{-1} and 1639 cm^{-1} were due to pyridinium ions bound to Brønsted acid sites, while the bands at 1446 cm^{-1} and 1619 cm^{-1} were due to pyridine bound to Lewis acid sites. H-bonded pyridine showed a band at 1596 cm^{-1} while the band at 1488 cm^{-1} was assigned to pyridine associated with both Brønsted and Lewis acids.

The trend in the relationship between Brønsted and Lewis acid sites according to Al grafting on MSN is illustrated in Fig. 34 B. Brønsted and Lewis acid sites related Al coordination sphere were determined by ^{27}Al MAS NMR spectroscopy. The spectra of higher Al loaded samples showed two peaks at around 0 and 55 ppm, corresponding to extra-framework (octahedral) and framework (tetrahedral) Al coordination, respectively. An increase in Al loading in mesoporous silica amplified the acid sites that embraced the molecules, and raised the retention in Ibuprofen release.

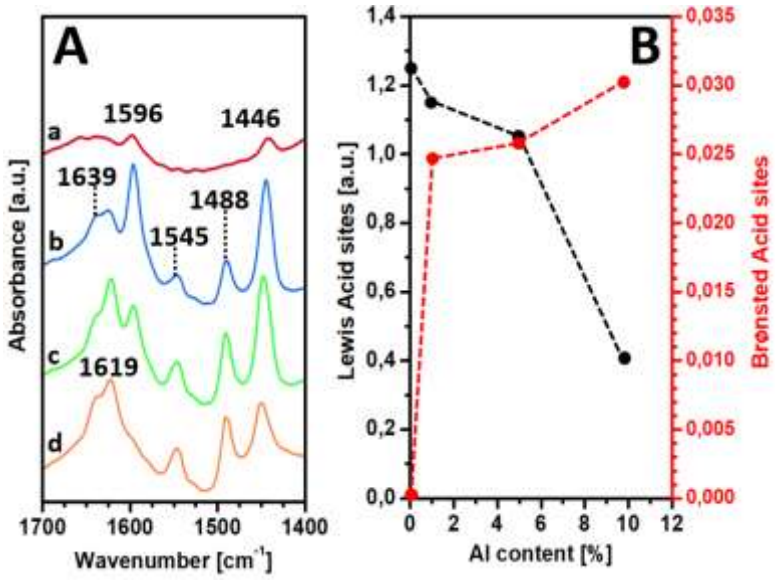

Fig. 34 (A) FT-IR spectra of adsorbed pyridine of: (a) MSN; (b) 1Al-MSN; (c) 5Al-MSN; (d) 10Al-MSN outgassed in 423 K. (B) Relationship of Lewis acid sites and Brønsted acid sites with Al loading. Adapted with permission from ref. 360. Copyright 2015 The Royal Society of Chemistry.

Bhaumik *et al*. have reported a new heterogeneous catalyst, mesoporous bifunctionalized organosilica containing Brønsted acidic and basic sites, with exceptionally high surface area and tuneable porosity.[361] They have employed various techniques along with FT-IR and ssNMR spectroscopy to determine the acid strength and demonstrated the excellent catalytic activity of the mesoporous material for the synthesis of HMF from various carbohydrates.

Washton *et al*. unveiled the confinement effects on the behaviour of supercritical methane in nonporous and mesoporous silica under variable temperature and pressure regimes using high pressure MAS NMR and MD simulations.[362] ^{13}C MAS NMR experiments on bulk methane showed the chemical shift of methane in the pure state was between −10.45 and −9.71 ppm

from 28.2 to 112.7 bar of pressure, respectively. The ^{13}C isotropic chemical shift of methane mixed with nonporous silica changed only slightly (-9.76 ppm at 112.7 bar). Meanwhile, methane loaded into mesoporous silica exhibited two distinct resonances at −9.62 and −9.17 ppm due to unconfined and mesopore confined molecules, respectively (Fig. 35 A). The effects of confinement were studied by variable temperature ^{13}C MAS NMR measurements. A lack of thermal response was observed for ^{13}C chemical shifts associated with unconfined methane either in nonporous or mesoporous silica (as well as for bulky methane). In addition, confinement effects are evident in the line broadening exhibited for methane in mesoporous silica relative to pure methane. A decrease in pore size leads to hindered translational and rotational motion for the methane molecules, leading to restricted motion that will shorten the T_2 relaxation time and contribute to line broadening. Pressure induced changes to the ^{13}C NMR chemical shift values of methane were attributed to methane densification on the pore surface and molecular dynamics disclosed the fluid densification enhanced by pore confinement and increased CH_4−CH_4 interactions (Fig. 35 B).

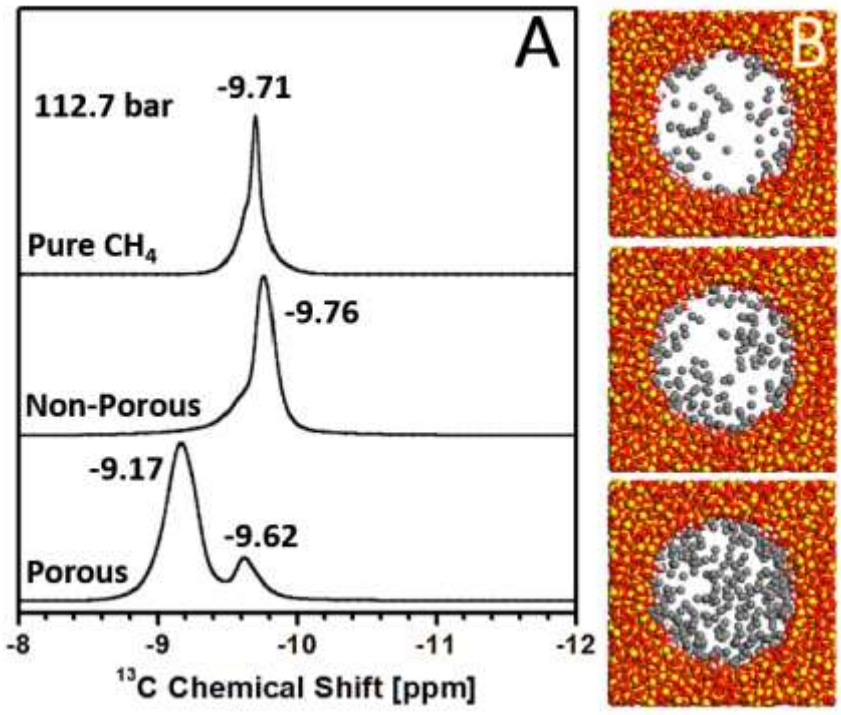

Fig. 35 Proton decoupled ^{13}C MAS NMR spectra of methane in the pure state and in mixtures with nonporous silica and mesoporous silica, acquired at 112.7 bar and 307 K (A). Snapshots of 4 nm silica pore model (B) with methane adsorbed at 307 K, 28.2 bar (Top), 56.4 bar (middle), 112.7 bar (Bottom). Red balls are oxygen atoms, gold balls are silicon atoms, white balls are hydrogen atoms, and grey balls represent methane molecules. Adapted with permission from ref. 362. Copyright 2017 American Chemical Society.

5.3.2. Mesoporous solids for drug delivery

Confining pharmaceutically active ingredient into the mesoporous materials has been a hot topic in the recent past. Bioavailability of the drug molecule can be enhanced by their retarded release from meso-pores. About 25 % of all marketed drugs are fluorinated molecules and developing novel nano-confined pharmaceutical formulations as drug delivery systems can have day-to-day applications. Nartowski *et al.*[363] have applied variable temperature ^{19}F magic angle spinning NMR spectroscopy along with computational methods, to derive detailed mechanistic insights into the crystallization of Flufenamic Acid in a confined environment of mesoporous silica materials with different pore diameters (3.2–29 nm). They found out that the encapsulation of Flufenamic Acid molecules within silica scaffolds led to either the formation of confined crystals or the stabilization of the confined amorphous phase, as well as a highly mobile species in the form of a molecular liquid-like layer at the silica surface depending on the pore size of the host and the properties of guest molecules (size, flexibility, and thermal behaviour). A combined approach enabled them to gain a better understanding of the fundamental processes of molecular aggregation at different porous environments, motional regimes and at different length scales.

Azaïs *et al*. have applied DFT calculations and ssNMR spectroscopy to determine the origin and the strength of the interactions at the molecular level for Ibuprofen and benzoic acid, encapsulated in hydrated MCM-41 modified with organic moieties.[364] They have observed both by calculations and experimental methods that micro-solvated silica surface was found to adsorb better Ibuprofen and benzoic acid than the bare silica surface at 300 K. The water layer acted as an adhesive between the organic molecules and the silica surface, where rapid reorientation of the molecules inside the mesoporous silica occur due to adsorption/desorption induced by the interactions. On the other hand, silica surface functionalization by aminopropyl groups confirms that the adsorption of organic molecules on that surface was very unfavourable in the absence of micro-solvation. The water molecules at the surface prevent the aminopropyl moiety from interacting preferably with the surface silanols and a competition between water adsorption and interaction with the amino groups makes the aminopropyls available for interaction with Ibuprofen or benzoic acid molecules which lead to their retarded desorption from the silica surface. They have stated that, by the careful choice of organic functionalization in mesoporous silica, one could control the release rate of the molecule of interest. A combination of ab initio calculations

and ^{1}H and ^{13}C ssNMR experiments were used to investigate the adsorption of Ibuprofen onto hydrated and functionalized mesoporous silica: the theoretical models helped to describe the position and the adsorption energies, highlighting the central role of water monolayers on the silica surface.[364] In a related study, they have applied variable temperature ^{1}H MAS NMR experiments to demonstrate the fast chemical exchange between protons of the COOH group of the organic molecule and protons from water molecules at the silica surface.[365] A different approach was adopted by Vega *et al*.[366] to describe the adsorption/desorption dynamics of a drug model, namely a glycine-alanine dipeptide, onto SBA-15 at different degrees of hydration: the interaction with the hydrated surface was followed by deuterium MAS NMR, evaluating the size of the water clusters surrounding the adsorbed molecules. In this case, molecular dynamics (MD) simulations were used to support the measurements and model the adsorbate dynamics: a standard force field was used.

Many applications of mesoporous silica involve drug delivery and controlled release: recently, some papers apply theoretical methods along with FT-IR and ssNMR techniques to describe the interaction of drug molecules, or their molecular models, with such environments. Barczak *et al*. described a number of SBA-15 samples decorated with different organic groups, including amines, pyridine, thiols and others, and evaluated the adsorption capacities of Diclofenac, a widely used anti-inflammatory drug. The results were rationalized by describing the interaction of Diclofenac with the organomodified surface by means of FT-IR measurements and DFT calculations, to detail the atomistic interactions.[367] Other drug release experiments were performed on mesoporous silica microspheres functionalized by metal (Pt and Ti) complexes, studying the interaction and the release dynamics of guanosine and bovine serum albumin by means of FT-IR and ^{13}C MAS-NMR: DFT calculations supported the experiments by modelling the interaction energies and the adsorption/desorption mechanisms.[368] MCM-41 and SBA-15 were tested as potentials carriers for a poorly soluble drug (Nimodipine), which was shown to be incorporated either in crystalline or in amorphous form, the latter being markedly more resistant to washing: the properties of the loaded samples were characterized by several techniques, including FT-IR and DFT calculations, which were used to interpret the vibrational spectra (modelling the bulk Nimodipine molecule).[369]

5.3.3. Mesoporous solids for CO_2 adsorption

In a recent report, structure of chemisorbed CO_2 species in amine-functionalized mesoporous silica were studied by ssNMR and computer modelling.[370] To shed light on the nature of chemisorbed CO_2 species formed and their intermolecular interactions with neighbouring amine groups, they have applied a ssNMR and computational approach on various amine-grafted SBA-15 materials loaded with ^{13}C-labeled CO_2 at variable pressures under tightly controlled atmosphere. Three distinct chemisorbed CO_2 species were identified in this study and all of them were involved in hydrogen bonds with either surface silanols or neighbouring alkylamines. Different combinations of hydrogen bonding networks (weak to very strong) essentially stabilizes the carbamic acid and alkylammonium carbamate-like ion pairs in amine-grafted SBA-15 materials loaded with $^{13}CO_2$.

Gatti *et al*. reported a study on the adsorption of CO_2 on different organo-modified silicas (SBA-15 and MCM-41) with varying degree of amine concentrations. They have employed three different amino-silane species, namely, 3-aminopropyltriethoxysilane (APTS), 3-(2-aminoethyl) aminopropyltrimethoxysilane (EAPTS) and 3-[2-(2-aminoethyl)aminoethyl] aminopropyltrimethoxysilane (PAPTS) which were incorporated into mesoporous silica by either grafting procedure or by one-pot preparation method.[371] In another strategy, they have varied the particle size of the mesoporous silicas which had grafted amino groups and studied the CO_2 adsorption behaviour.[372] By using integrated approach of various spectroscopic (FT-IR and ssNMR) and calorimetric techniques as well as computational techniques, they have found out that the reactivity of amino-modified silica samples towards CO_2 was deeply influenced by both the preparation route and by the type of organo-silane used for the functionalization of the materials. Post-synthesis grafting of organo-silane was more efficient than one-pot method, as the CO_2 adsorption data showed. Amine protonation owing to the acidic preparation condition was responsible for the ineffective nature of one-pot preparation method. On the other hand, a higher amount of CO_2 physisorption was observed in the nanometer sized mesoporous sample, due to their higher pore volume, whereas, chemisorbed (carbamate and carbamic acid) species were predominant in the micrometer sized sample (Fig. 36).

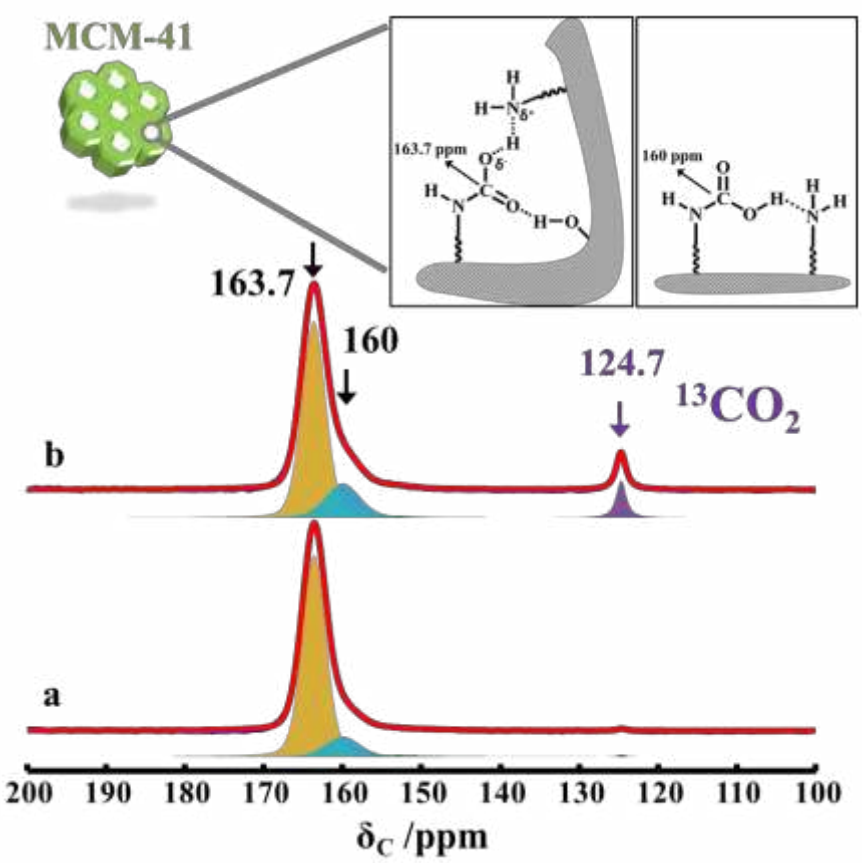

Fig. 36 ^{13}C MAS NMR spectra of $^{13}CO_2$ adsorbed on amino-silane grafted mesoporous MCM-41 with micro-size particle (a) and nano-size particle (b) recoded using a MAS rate of 10 kHz. Each spectrum includes experimental and deconvoluted spectra[373] with individual contributions from each ^{13}C site. Schematic diagram representing two possible models of the hydrogen bonding network formed by carbamate and carbamic acid species with surface silanols and neighbouring amino-units. Adapted with permission from ref. 372. Copyright 2017 The Royal Society of Chemistry.

Combined theoretical and experimental techniques have been often used to characterize organo-modified mesoporous silica: for instance, a surface functionalized by aminopropyltriethoxysilane was studied by ^{29}Si NMR, as well as TGA and ESI-MS, and modelled by DFT calculations, which helped to describe the hydration states of the tethered functional groups.[374] The stability of organo-modified silica, with amines of variable length grafted on the surface, was investigated in a number of different conditions, to evaluate the relation between stability and chain length. Several experimental techniques were employed, among which ^{13}C ssNMR, and the results supported by ab initio calculations describing the degradation pathways by optimizing reactants, products and possible transition states.[375]

Some older results about the structure and the stability of surface modified silica for the immobilization of enzymes are reviewed.[376] Here, some examples of molecular dynamics simulations supporting the structure analysis are reported, highlighting the importance of a theoretical atomistic description when non-crystalline samples are found.

Other surface modifications of silica have been recently described by combined methods: for instance, zinc oxide grafted on mesostructured silica foam has been described by vibrational spectroscopy supported by theoretical calculations performed on realistic amorphous silica surface models, using the harmonic simulated spectra to assign the experimental vibrational modes.[377] The CO_2 adsorption in SBA-15 was shown to increase upon incorporation of potassium chloride particles: the formation of gas-trapping sites around the KCl clusters, caused by the intense electrostatic field generated, was described by molecular dynamics simulations with a specifically derived force field, and by DFT calculations of the adsorption energies. In this work ^{29}Si MAS-NMR spectra were recorded to confirm the results of the simulations, showing the actual formation of regions with a high concentration of gas around the KCl clusters.[378] A series of crown-ethers were immobilized on SBA-15 surface, previously derivatized with alkyl halide chains, to test the separation of lithium isotopes from liquid samples: the structure of the functionalized surfaces was confirmed by ^{1}H and ^{13}C NMR spectra, and the complexation reaction between lithium and the macrocycle ligands was reproduced by ab initio calculations. In this work, the structure of the Li complexes inside the silica pores could be described in good detail, thanks to the comparison of the optimized structures with the results of the NMR analysis.[379]

Paul *et al*. have applied multi-technique approach on the investigation of interaction of water vapour with aminopropyl groups on the surface of mesoporous silica nanoparticles.[380] The application of rotor-synchronised spin-echo magic angle spinning ^{1}H NMR methodology provided the substantial suppression of broad probe background signal as well as the signals from strongly dipolar coupled terms (other broad signals) in partly hydrated samples delivering an opportunity to obtain the signal of surface groups. They have judiciously chosen the delay time (τ) as an optimised compromise between the signal decay owing to relaxation and the resolution gain owing to longer delay times. The essential advantage of this approach was that, it could provide a spectrum, without undergoing drastic surface changes and masking of delicate interface interactions when the sample was dehydrated under vacuum. The interaction of water with the surface of mesoporous silica functionalized by aminopropylsilanes was carefully studied by ^{29}Si, ^{1}H and ^{13}C ssNMR and FT-IR

spectroscopy, evaluating the strength of hydrogen bonds between the organic chains and the surface silanols, as well as with the water molecules, and evidencing the presence of a small amount of protonated ammonium groups. This point was discussed in detail with the help of ab initio simulations, showing the conditions for the protonation of amino groups on the silica surface in the presence of water.[380]

Andreev *et al*. further developed the spin-echo sequence with the insertion of a dipolar filter prior to the sequence.[381] ^{1}H dipolar filtering spin-echo MAS NMR technique has been demonstrated its usability, in that work, for the semi-quantitative analysis of dried and partly hydrated commercially available zeolites. They acknowledged that the technique can reveal the framework stacking faults species that can be crucial for understanding of relationships of structure and performance.

Otomo *et al*. prepared variable Al loaded MCM-68 zeolites by post-synthetic acid treatment that were investigated by ^{27}Al MQMAS NMR spectroscopy.[55] Location of Brønsted acid sites and their tolerance against the acid treatment were determined by FT-IR spectroscopy using two probe molecules, pyridine and di-*tert*-butylpyridine. Brønsted acid sites were located in the 12MR channel as well as in 10MR windows and inside the supercages for Si/Al ratio of 10. High-silica MCM-68 had Brønsted acid sites predominantly in the 10MR windows and inside the supercages confirming their high resistance against the acid treatment. MCM-68 catalysts with Si/Al ratio of 33 showed better catalytic performance in the dehydration of sorbitol than Beta, ZSM-5, and Mordenite.

5.3.4. Other Applications

Harrach *et al*. demonstrated the unique applicability of ssNMR methods combined with MD simulations for the characterization of binary fluid mixture inside porous silica materials.[382] The phase behaviour of an isobutyric acid-water mixture inside mesoporous SBA-15 material showed microphase separation: the isobutyric acid-rich phase was close to the pore wall while the water-rich phase was in the center of the pores. However, upon increasing temperature, the relative water concentration increases at the pore surface and leads to a more thorough miscibility.

Another interesting illustration of the relevance of multi-technique approach in characterizing mesoporous silica nanoparticles was reported by Martins Estevao *et al*.[383] These authors

covalently coupled Rose Bengal (RB) photosensitizer to mesoporous silica nanoparticles (MSN) and demonstrated the advantage in photodynamic therapy applications given that the photosensitizing molecules are stably incorporated into the nanoparticles and are protected from the outer environment. The covalent coupling and the stability of RB on MSN was confirmed by FT-IR (Fig. 37) and ssNMR spectroscopic techniques. The structure of RB in water solution and immobilized into the channel of MSNs was also optimized theoretically, with DFT methods, to understand the structural modifications induced by the adsorption on the silica particles.[384]

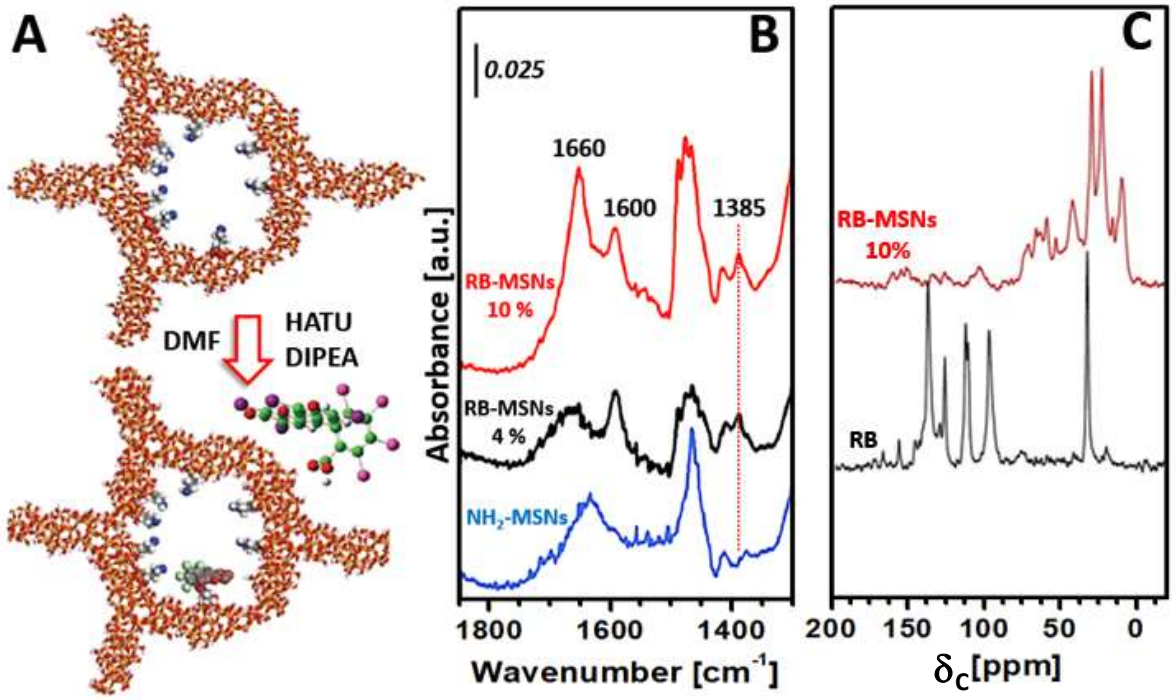

Fig. 37 Schematic representation of the synthetic procedure used to obtain Rose Bengal photosensitizer bound to mesoporous silica nanoparticles (A). FT-IR spectra of RB-MSNs and NH_2-MSNs (B) and ^{13}C CPMAS NMR spectra (C) of RB-MSN and pure Rose Bengal. Adapted with permission from ref. 383. Copyright 2015 The Royal Society of Chemistry.

The design and development of molecular machines including molecular rotors, motors, and brakes have attracted attention over the past decade.[385] To control the rates of rotation and rotational barriers of molecular devices, one may judiciously use non-covalent forces (e.g. hydrogen bonding). Molecular dynamics in such systems can easily be followed by ssNMR spectroscopy in combination with other techniques. Comotti *et al*. have reported, in 2008, the study of molecular rotor motions in periodic mesoporous organosilicas (PMOs), which consist of fully covalent architectures using phenyl-silica.[386] Recently, they have studied

periodic mesoporous hybrid materials composed of divinyl-*p*-fluorophenylene units bridging two adjacent siloxane layers, exhibiting periodic architecture.[387] For the structural characterization, they have employed ssNMR to investigate the motional behaviour of *p*-phenylene moieties in the mesoporous fluoro-organosilicas using ^{13}C spin–lattice relaxation measurements. The 180° flip of benzene ring was demonstrated by ^{2}H NMR (ca. 108 Hz at 325 K). They have achieved the molecular rotational modulation by substituting the organic unites (e.g. with I_2) or by filling the pores with guest molecules (e.g. with N_2 or CO_2) as shown in Fig. 38. Such solids can be used in gas capturing, detection and sensing.

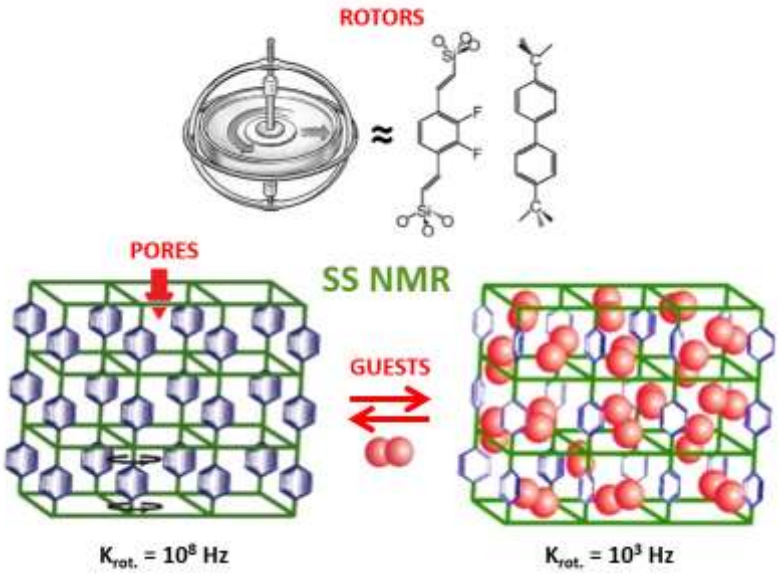

Fig. 38 Schematic representation of macroscopic gyroscope, molecular rotors and the host-guest molecular dynamics in porous solids detected by ssNMR. Adapted with permission from ref. 385. Copyright 2016 American Society of Chemistry.

In the past thirty years, ^{129}Xe NMR has been applied to various porous systems, as an efficient technique to investigate the structure of porous solids. The timeline of ^{129}Xe NMR development is reported in Fig. 39. The main advantage of ^{129}Xe NMR is the high sensitivity of xenon atom to its local environment. Any distortion of the large highly-polarizable electron cloud of xenon atom is directly transmitted to the nucleus, affecting the chemical shift. During the last 30 years, ^{129}Xe NMR spectroscopy has been applied on various systems, such as microporous zeolites, mesoporous silica, pillared clays, hierarchical solids, and hybrid porous materials.[388,389]

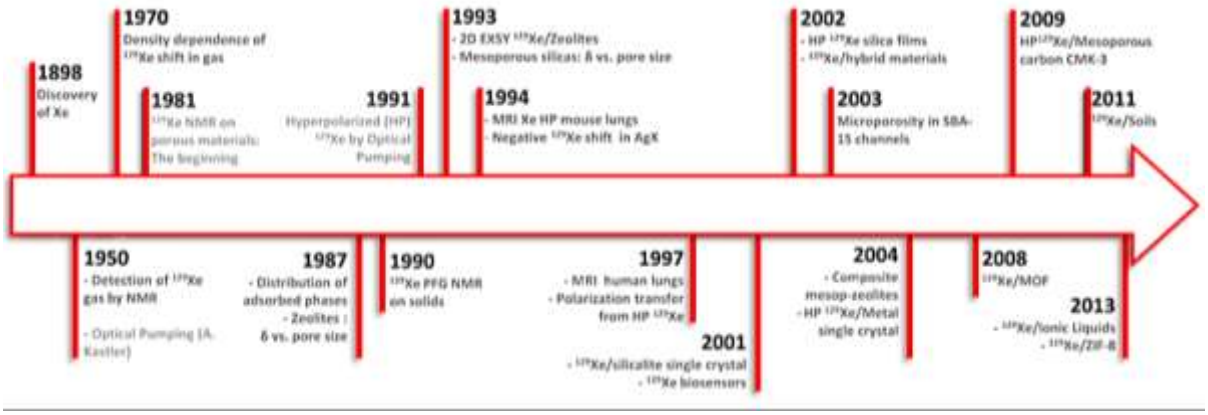

Fig. 39 Historical timeline of ^{129}Xe NMR with important years and events. Adapted with permission from ref. 388. Copyright 2016 Elsevier Ltd.

Dynamic nuclear polarization (DNP) is one of the most promising methods to enhance the intrinsic sensitivity of ssNMR experiments by several orders of magnitude.[390] Recently, there are few reviews appeared which provided in-depth overview about the theoretical and practical aspects of DNP under MAS conditions at high magnetic fields.[391–394] They have also covered the applicability of DNP MAS NMR spectroscopy towards the problems in materials science and the readers are encouraged to go through these excellent sources for more in-depth information. The application of DNP NMR on microporous and mesoporous materials have been reported recently.[395–402] Lafon *et al*. have recently demonstrated the propagation of DNP-enhanced ^{1}H polarization via ^{1}H–^{1}H spin diffusion over distances up to several hundreds of nm in mesoporous silica nanoparticles (MSN) loaded with surfactant molecules.[396] The approach was established using MSN, functionalized with 3-(*N*-phenylureido)propyl (PUP) groups, filled with the surfactant cetyltrimethylammonium bromide (CTAB) and have observed an enhancement of ^{13}C and ^{29}Si signals $\varepsilon_{on/off}$ of around 8. In CTAB-free MSN, the DNP enhancement was around 30 validating the ability of radical TOTAPOL to penetrate into the mesopores of MSN. This research work has revealed the new opportunities created by DNP NMR for the study of organic–inorganic hybrid porous materials.

5.4. Hierarchical porous materials

Microporous materials (porous diameter < 2.0 nm) such as zeolites have been extensively used as heterogeneous catalysts in refinery and petrochemical industrial processes where their

shape-selective properties are exploited. Nevertheless, zeolites do not work at their fully potential due to the fact that the sole presence of micropores imposes diffusion limitations on the reaction rate, and the mass transport to and from the active sites located within the micropores is slow and limits the performance of industrial catalysts. Different synthetic strategies have been adopted to avoid this limitation, such as minimizing the size of the zeolite crystals (< 50 nm) or increasing the pore size of the zeolites losing in this way the shape-selectivity. Some other limitations are introduced following this procedures, in fact large pore zeolites or mesoporous materials suffer for low shape-selectivity, while small zeolite crystals are difficult to recover. For these reasons, hierarchical zeolites, which combine two levels of porosity (micro and meso) in the same material, represent a viable alternative to traditional microporous systems.[403,404] Two levels of porosity interconnected into porous materials can be achieved following a "top-down" or a "bottom up" approach. The top-down approach involves post-synthetic modifications, such as demetallation under acidic or basic conditions, to extract framework constituents whilst preserving crystallinity. Whereas, the bottom-up approach uses surfactants and templates, whereby sophisticated and sacrificial surfactant molecules self-assemble into a supramolecular micelle that guides the formation of the mesoporous network, a structure-directing agent facilitates the formation of the microporous architecture. The bottom-up approach is a relatively facile route, being compatible with a "one-pot" synthesis, and benefits from a high degree of structural control through the modification of the micellar structure (see the special themed issue of Chem. Soc. Rev., titled "Hierarchically-structured porous materials: from basic understanding to applications" appeared in 2016)[405]

The catalytic evaluation of hierarchical zeolites has shown enhanced performances in traditional and emerging applications.[406,407] In addition, the peculiar features of hierarchically porous materials, high surface area, large accessible space, low density, variable chemical compositions and interconnected hierarchical porosity at different length scales, can be exploited not only in catalysis but also for light harvesting, electron and ion transport, and mass loading and diffusion, endowing them with technological importance in energy storage and conversion, photocatalysis, adsorption, separation, gas sensing, and biomedicine applications.[408]

Multi-techniques approach is needed to elucidate structure, texture and localization of the active sites in the multilevel pore network of hierarchical zeolites.[409] As for the Brønsted

acidity is necessary to compare the spectroscopic features using FT-IR and ssNMR of the hierarchical zeolites with the ones of the analogues microporous zeolites, in fact in hierarchical zeolites the distribution of the acid active sites in the internal or external surfaces requires particular attention and the adsorption of substituted bases of different size that can selectively probe acid sites in different positions is highly recommended. The structural modification responsible for changes in the acidity of hierarchical zeolites can be clarified by ^{27}Al MAS NMR studies that enable to check the coordination of aluminium revealing the presence of penta- or octahedrally coordinated sites. The number of framework Si atoms that can be removed without producing structural damage is governed by the Si/Al ratio and framework topology as well as by alkaline treatments (concentration and type of desilicating agents). Gośa-Marek *et al*. used a dealumination/desilication approach combined by the presence of tetraalkylammonium, a pore directing agent (PDA) to produce hierarchical mordenite starting from commercial MOR zeolite, and reported a detailed ssNMR and FT-IR characterization.[410] The ^{29}Si and ^{27}Al (Fig. 40) MAS NMR analyses clarified the local environment of Si and Al atoms upon the consecutive demetallation processes and addition of tetrabutylammonium hydroxide (TBAOH) as PDA. The ^{29}Si MAS NMR spectrum of commercial MOR showed a strong signal at 111 ppm attributed to Si(4Si,0Al) units and a less intense one at 105 ppm evidencing the presence of one Al in the direct neighbourhood of Si atoms, Si(3Si,1Al). Upon dealumination (DeAl/MOR), the Si(3Si,1Al) signal decreased significantly in intensity and an increase in the Si(4Si,0Al) signal was observed evidencing a high efficiency of the dealumination procedure. For alkaline(NaOH)-treated (DeSi_NaOH/DeAl/MOR) and added TBAOH (DeSi_NaOH & TBAOH/DeAl/MOR) samples, a drop of the Si(4Si,0Al) signal was detected due to a decrease of the Si/Al ratio of the sample upon desilication. Nevertheless, in NaOH & TBAOH medium the privileged extraction of silicon atoms from Si(4Si,0Al) units was observed, since for DeSi_NaOH&TBAOH/DeAl/MOR the 2-fold increase of the Si(3Si,1Al)/Si(4Si,0Al) intensities ratio was evidenced, when comparing to DeAl/MOR. On the contrary, for DeSi_NaOH/DeAl/MOR the increase of the Si(3Si,1Al)/Si(4Si,0Al) ratio was considerably less pronounced. Consequently, in NaOH medium, Si atoms in the neighbourhood of four Si in Si(4Si,0Al) units are extracted before those Si atoms that are placed in the Si(3Si,1Al) units. Thus, the presence of AlO_4^- stabilizes neighbouring Si atom (in the Si(OH)Al groups) by the repulsion of OH^- ions.[411] This effect is predominant when the zeolite was treated in the presence of TBAOH. The ^{27}Al MAS NMR spectrum of the commercial MOR consists of one intense signal at 50 ppm assigned to tetrahedral Al(IV) at the zeolite framework.

Dealumination results in the 3-fold drop of Al(IV) signal and the appearance of a small signal typical of Al(VI) extra-framework species. Further treatment, i.e., desilication, reverses an earlier trend, and the expected growth of the Al(IV) signal was observed. The typical signal of Al(VI) species was not detected in the ^{27}Al MAS NMR spectra of desilicated zeolites (DeSi_NaOH/DeAl/MOR and DeSi_NaOH&TBAOH/DeAl/MOR).

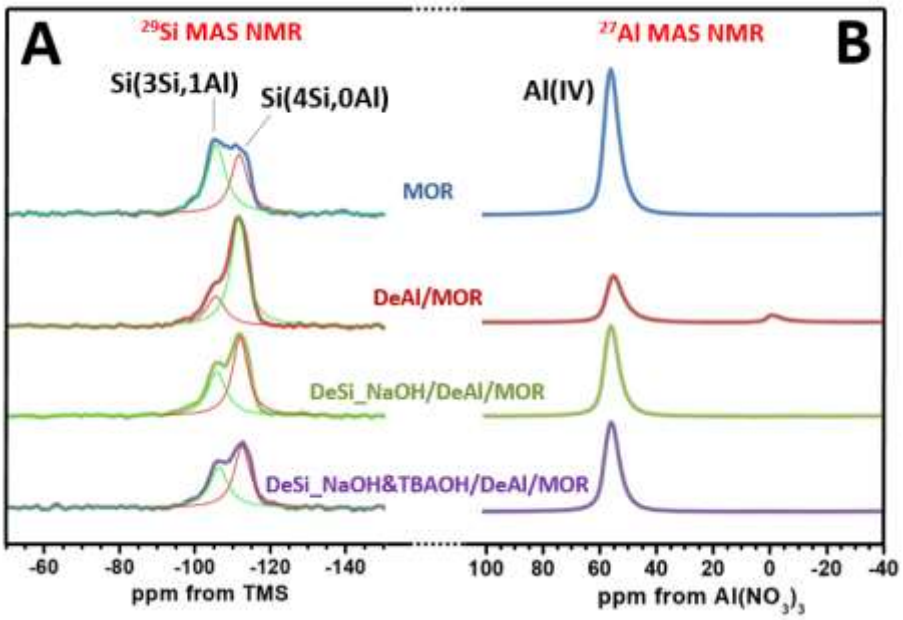

Fig. 40 ^{29}Si MAS NMR (A) and ^{27}Al MAS NMR (B) spectra of mordenite samples. Reproduced with permission from ref. 410. Copyright 2014 American Chemical Society.

The acidity of the hierarchical mordenite was evaluated by FT-IR spectroscopy by the comparison of the OH groups in the O-H stretching mode range present in the differently treated samples. Brønsted acid sites (Si-OH-Al) typical of MOR catalysts are present in the FT-IR spectra at 3603 cm^{-1}. Dealumination of commercial mordenite (DeAl/MOR) produced a significant reduction of the intensity the Si(OH)Al band accompanied by the development of the low intensity broad band associated with the formation of H-bonded Si−OH groups in silanol nests (3500 cm^{-1}). Desilication resulting in the selective Si atoms extraction for alkaline(NaOH)-treated MOR is manifested as growth of the 3740 cm^{-1} Si−OH band intensity related to the enhanced population of silanol groups on new fabricated mesopore system, i.e., mesopore surface improvement. Moreover, the band at 3610 cm^{-1} due to Brønsted acid sites is restored. CO adsorption at low temperature (Fig. 41 B) evidenced that Lewis acid sites originated from dehydroxylation, and this predominantly suggests that the Al species

introduced to the desilicating mixture were partially integrated into the zeolite framework giving rise to both Brønsted and Lewis acidity. This reinsertion of the Al atoms, extracted from zeolite together with the Si atoms, onto the mesopore walls led to the new acid sites formation, mainly the Lewis acid sites. One of the hypotheses assumes that the Brønsted sites formed by reinserted Al atoms are disposed toward dehydroxylation; thus the Lewis acid sites formed in this process are situated on the mesopores walls. In consequence, the amount of Lewis acid sites can be taken as the measure of the resistance of the desilicated zeolite to the thermal treatment and, in the case of desilicated mordenite, clearly confirms their high thermal stability.

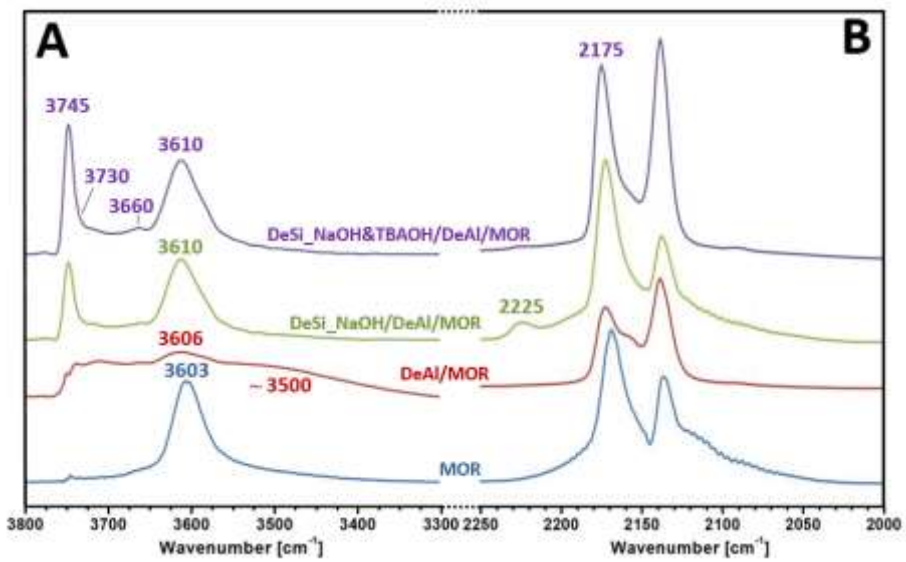

Fig. 41 FT-IR spectra in the O−H stretching region (A) and in the C-O stretching region after CO adsorption at 77K (B) on mordenite samples. Reproduced with permission from ref. 410. Copyright 2014 American Chemical Society.

Erigoni *et al.*[62] explored a post-synthetic desilication strategy in alkali (NaOH) media to produce hierarchical H–ZSM-5, starting from parent MFI zeolites with different Si/Al ratio. In H–ZSM-5 microporous zeolite, different types of silanol groups are present, external and internal Si-OH, and nest Si-OH, together with stronger Si-OH-Al Brønsted sites: the alkali treatment can modify these OH sites, in terms of their localization, concentration, and acid strength. FT-IR spectroscopy of adsorbed probe molecules coupled with ^{1}H MAS NMR was performed to assess the impact of the post-synthetic desilication on the acidic properties of the produced hierarchical ZSM-5. The effect of the NaOH treatment on hierarchical H–ZSM-5 is visible in the O-H stretching region of the FT-IR spectra (Fig. 42 A). The alkaline-treated

ZSM-5 (labelled 30H and 80H) show an increasing of the signal of the isolated Si-OH groups (3745 cm^{-1}) with respect to parent zeolites (labelled 30P and 80P) in agreement with their increased external surface area. On the contrary, a fraction of the Brønsted acid sites (Si-OH-Al groups, BAS), which shows a typical band at 3615 cm^{-1}, was lost in the hierarchical catalysts; this effect is particular evident in the low Si/Al catalyst. Together with FT-IR spectra, ^{1}H MAS NMR spectroscopy provided direct information on the different proton sites present in the hierarchical zeolites (Fig. 42 B). The proton spectra of parent and hierarchical zeolites (recorded on catalysts treated at 250 °C) consist of contributions from isolated Si-OH_{ext} (1.6–1.8 ppm), Si-OH_{int} (2.0 ppm), hydroxyl units bound to Lewis acid sites (LAS) and extra-framework Al species (EFAl) through hydrogen bonding (2.4– 2.8 ppm), Brønsted acid sites (3.8 ppm) and H-bonded hydroxyls (Si-OH_{nest}) (4.3 ppm). In addition, a peak at 0.8 ppm due to isolated Al-OH is visible in the 30 P sample. Quantitative representations of various protonic species are shown in Table 2 correlated with the FT-IR frequencies. The desilication treatment produces an increase in the signal intensity of isolated Si-OH groups with respect to the parent zeolites and a loss of a fraction of BAS, particularly evident for the low Si/Al ratio zeolite. Moreover, the presence of H-bonded species is confirmed in all samples and the presence of isolated Al-OH species is evidenced only in the low Si/Al samples.

Table 2 FT-IR frequencies and population distribution of protonic species obtained from ^{1}H MAS NMR in parent and hierarchical H-ZSM-5 zeolites. Reproduced with permission from ref. 63, Copyright 2016 Wiley-VCH

ASSIGNMENTS	ν_{OH} [cm^{-1}]	^{1}H CHEMICAL SHIFT (δ) [ppm]	^{1}H SPECIES (%)			
			30H	*30P*	*80H*	*80P*
Si-OH_{ext}	3745	1.6 – 1.8	12	4	17	6
Si-OH_{int}	3720 - 3710	1.8 – 2.0	17	11	10	11
LAS	3665	2.4 – 2.8	18	16	22	18
BAS	3615	3.8	9	19	13	18
Si-OH_{nest}	ca. 3500	4.3 – 6.6	44	46	38	47

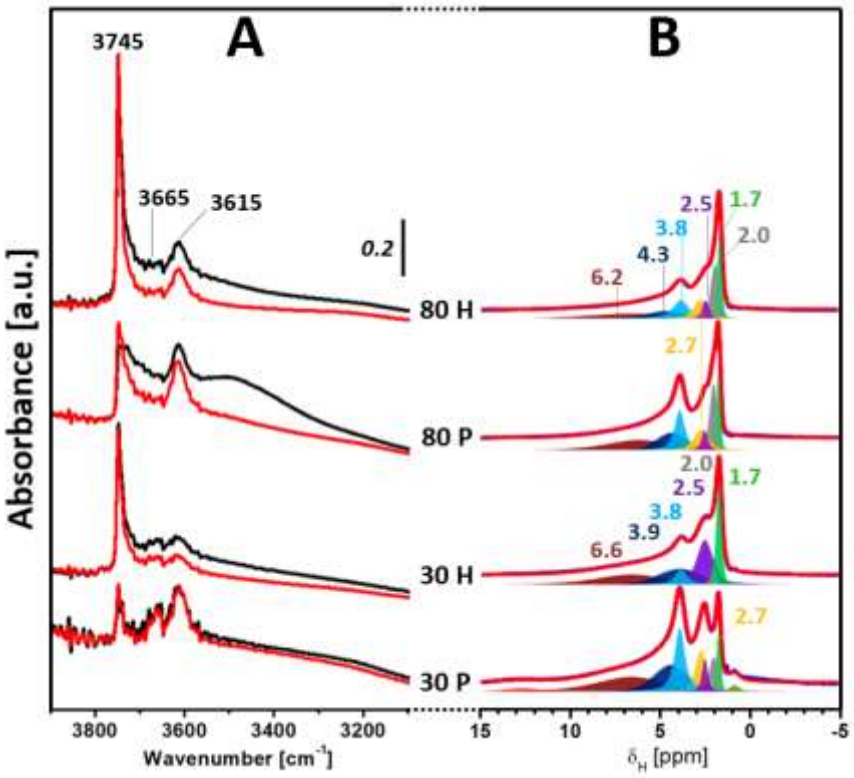

Fig. 42 A) FT-IR spectra in the O-H stretching region of parent and hierarchical H-ZSM-5 thermally treated at 250°C (black lines) and at 500°C (red lines). B) ^{1}H MAS NMR spectra recorded after outgassing the catalysts at 250°C. Experimental and deconvoluted spectra with individual contribution from each ^{1}H sites are reported for each samples. Reproduced with permission from ref. 63, Copyright 2016 Wiley-VCH.

To assess the accessibility and strength of acid sites in hierarchical H–ZSM-5, FT-IR spectroscopy of adsorbed probe molecules with different basicity and steric hindrance was used. Substituted pyridines have been widely used to study and quantify the enhanced

accessibility of acid sites in hierarchical zeolites, given their impediment to diffuse through small micropores. In particular, 2,4,6-trimethylpyridine (2,4,6-TMP) with a kinetic diameter (KD) approximately 0.74 nm is too bulky to enter the H–ZSM-5 micropores and interacts only with the acid sites located in either mesopores or micropore mouths of the hierarchical zeolites. These interactions can be readily identified in the aromatic ring vibration region of the FT-IR spectrum. In particular, the ν_{8a} mode, which in the liquid phase appears at 1611 cm^{-1}, is very sensitive to the acidity of the OH sites present on the catalysts, and its position changes with respect to the strength of the acid centres. When ν_{8a} mode appears at wavenumbers higher than 1630 cm^{-1}, the formation of a protonated species can be inferred, whereas lower wavenumbers correspond to H-bonded adducts.[412] The FT-IR spectra in Fig. 43 show the stretching region of C-C ring vibrations of the 2,4,6-TMP irreversibly adsorbed. In all samples, bands typical of 2,4,6-TMP H-bonded to Si-OH groups (1618 and 1572 cm^{-1}) are present. These bands almost completely disappeared after outgassing the samples at 423 K. A strong band at 1638 cm^{-1}, negligible for the parent zeolites and more resistant to the thermal treatment at higher temperatures is evident in the hierarchical zeolites and is assigned to the protonated 2,4,6-TMP molecules (2,4,6-$TMPH^+$) formed upon interaction with strong Brønsted acid sites. The presence of this band in the hierarchical catalysts evidenced that desilication enhances the accessibility to the internal Brønsted acid sites.

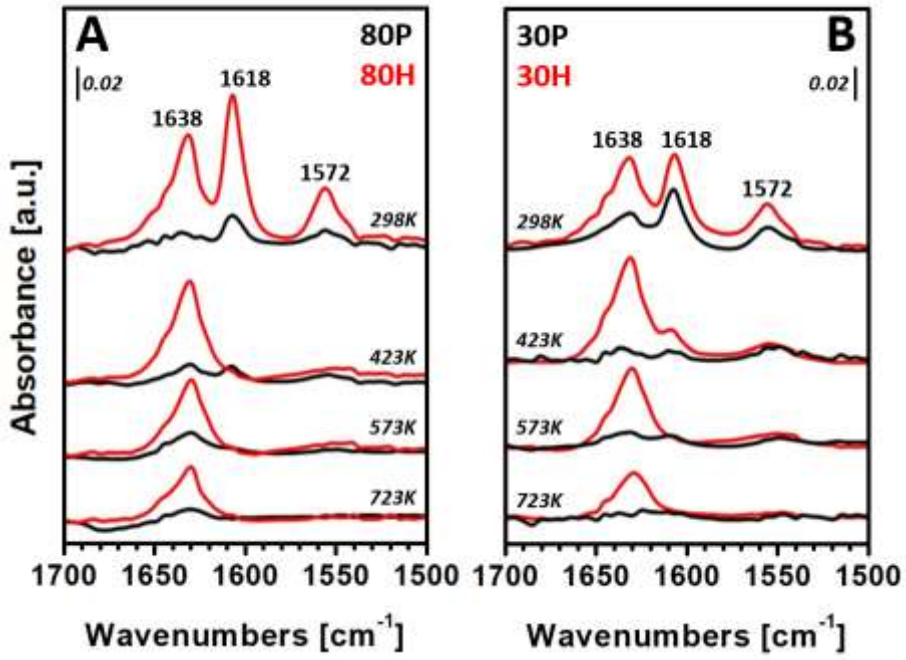

Fig. 43 FT-IR difference spectra of A) 80 P and 80 H and B) 30 P and 30 H upon 2,4,6-TMP outgassing at room temperature (90 min) and at higher temperatures (423, 573, and 723 K). Reproduced with permission from ref. 63. Copyright 2016 Wiley-VCH.

Table 3 Integrated area (A) of the ν_{8a} (1638 cm^{-1}) band and concentration of accessible Bronsted acid sites (N). Reproduced with permission from ref. 63, Copyright 2016 Wiley-VCH

CATALYSTS	A [cm^{-1}]	N [mmol g^{-1}]
80H	1.35	2.18
30H	1.04	1.69
80P	0.20	0.32
30P	0.07	0.11

The data in Table 3 clearly show that in the hierarchical materials (80H and 30H) the number of the Brønsted sites accessible by molecules as bulky as 2,4,6-TMP is greatly increased with respect to the parent zeolites.

Another example of the combination of FT-IR and ssNMR techniques to study the acidity of hierarchical ZSM-5 obtained by dealumination-realumination process (Scheme 4) is reported by Li *et al.*[413] ^{27}Al MAS NMR evidenced in the ZSM-5 sample treated with a NH_4F solution and subsequently in alkaline condition a broadening of the signal at 54 ppm due to tetrahedral Al sites suggesting the existence of various types of four-coordinate Al species. The acidity of the differently treated ZSM-5 samples was assessed by FT-IR (Fig. 44 A) Fluorination significantly decreases the intensities of the signals due to Si-OH defects (3720 and 3520 cm^{-1}) and of the band due to Brønsted acid sites (3600 cm^{-1}) for hierarchical H-ZSM-5 (HZ-F6: sample treated with 0.06M NH_4F solution) suggesting less Al framework compared to microporous H-ZSM-5 (HZ), which is in agreement with the distortion of tetrahedral Al in ^{27}Al MAS NMR. The bands due to the Si-OH also disappear for HZ-AT (sample treated with 0.2M NaOH solution), which confirms selective leaching of defective Si-sites by alkaline-treatment. On the contrary, the band 3600 cm^{-1} has a larger intensity, which is in agreement with a larger amount of Brønsted acid sites. A larger band at 3732 cm^{-1} is detected for HZ-F6-AT (sample treated with NH_4F followed by treatment with NaOH solutions), which demonstrates a larger amount of terminal Si-OH groups, while the intensity of the 3600 cm^{-1} band decreases compared to that of HZ, and this suggests special tetrahedral Al species for HZ-F6-AT. ^{1}H MAS NMR experiments (Fig. 44 B), in agreement with the FT-IR data, show three main resonances at 1.6 (Si-OH), 2.3 (OH bound to extraframework Al species), and 3.8 (BAS) ppm with different intensities in the treated samples. In particular, the 3.8 ppm signal of the HZ-F6-AT is weaker than that of the HZ, and this feature is ascribed to special Al sites that contribute less to acidity, as suggested by NH_3-TPD, ^{27}Al MAS NMR and FT-IR results.

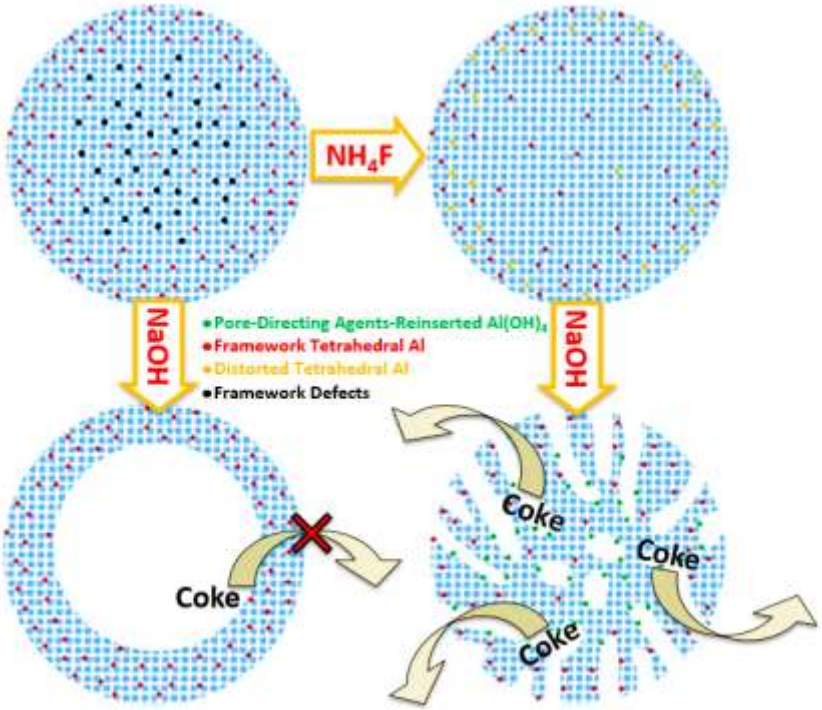

Scheme 4 Adapted with permission from ref. 413. Copyright 2017 American Chemical Society.

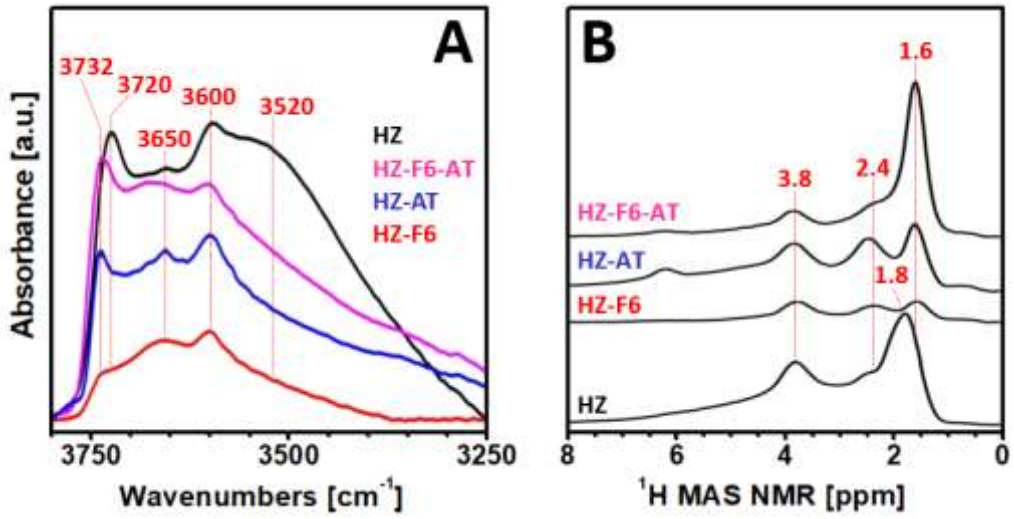

Fig. 44 A) FT-IR spectra in the O-H stretching region and B) ^{1}H MAS NMR spectra of ZSM-5 (HZ) and hierarchical H-ZSM-5 (HZ-F6: sample treated with a 0.06M NH_4F solution; HZ-AT: sample treated in 0.2M NaOH solution and HZ-F6-AT: sample treated in NH_4F followed by treatment in NaOH solutions). Reproduced with permission from ref. 413. Copyright 2017 American Chemical Society.

The “top-down” procedures used to convert microporous zeolites in hierarchical ones was also applied to produce hierarchical SAPOs catalysts;[414] also in this case FT-IR spectroscopy coupled with ssNMR was a powerful tool to explore the structural and physico-chemical modifications induced by the post-synthesis treatment.

As mentioned at the beginning of this chapter, hierarchical zeolites or SAPOs can be also synthesized by using a bottom-up approach using mesoporogens as surfactants in the synthesis gel.[61,415] Trimodal porous hierarchical SSZ-13 zeolites (CHA topology) has been obtained using $[C_{22}H_{45}\text{-}N^{+}(CH_3)_2\text{-}C_4H_8\text{-}N^{+}(CH_3)_2\text{-}C_4H_9]Br_2$ (denoted $C_{22\text{-}4\text{-}4}$ Br_2) as mesoporogen.[416] The nature of the OH groups of the SSZ-13 zeolites was investigated by means of ^{1}H MAS NMR (Fig. 45) and FT-IR spectroscopy of adsorbed CO. The deconvolution of the signal at lower ppm, evidenced two contributions, one at 1.8 ppm, due to isolated external Si-OH at lattice defect sites and one at 2.0 ppm that refers to the interaction of Si-OH with neighbouring oxygen atoms, indicating that they are located in the zeolite micropores. The band at ~4 ppm belongs to the Brønsted acid sites (i.e. protons bound to oxygen atoms bridging Si and Al) and signals in the region 2.5−3.0 ppm correspond to protons of Al-OH moieties at extra-framework positions. These assignments are supported by data from ^{1}H-{^{27}Al} TRAPDOR NMR experiments that helps to identify the protons located in the vicinity of Al atoms.

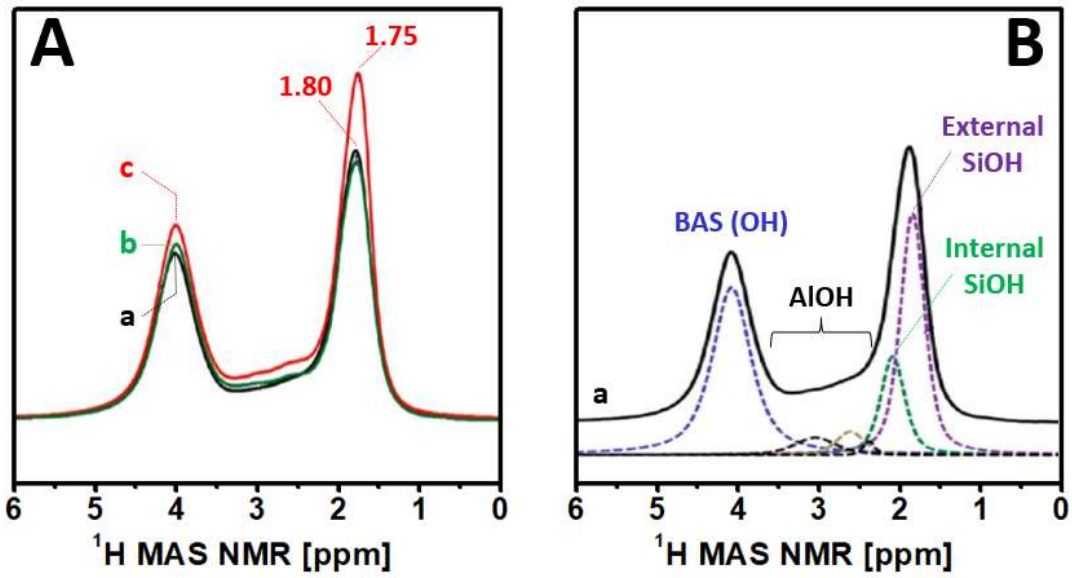

Fig. 45 (A) ^{1}H MAS NMR spectra of (a) SSZ-13-R, (b) SSZ-13-F, and (c) SSZ-13-F-M25. (B) deconvolution of the spectra for SSZ-13-R. SSZ-13-R is the reference sample, SSZ-13-F is the sample obtained by adding NaF to the synthesis gel and SSZ-13-F-M25 is the sample where a fraction of TMAdaOH (N,N,N-trimethyl-1-adamantammonium hydroxide) replaced by $C_{22\text{-}4\text{-}4}$

Br_2. Reproduced with permission from ref. 416.Copyright 2016 American Chemical Society.

The acidity strength was elucidated by FT-IR spectra of adsorbed CO and pyridine. Pyridine, a molecule too large to enter the pores of CHA zeolite, was used to detect Brønsted acid sites located outside the micropore space of the zeolites (Fig. 46, band at 1545 cm^{-1} due to the protonated form of pyridine upon interaction of strong BAS). The concentration of Brønsted sites at the external crystal surface of SSZ-13-R is negligible. On the contrary, such sites could be clearly observed for SSZ-13-F-M25 because of its higher surface area. It was estimated that approximately 5% of all of the Brønsted sites were located at the external crystal surface in hierarchical SSZ-13-F-M25.

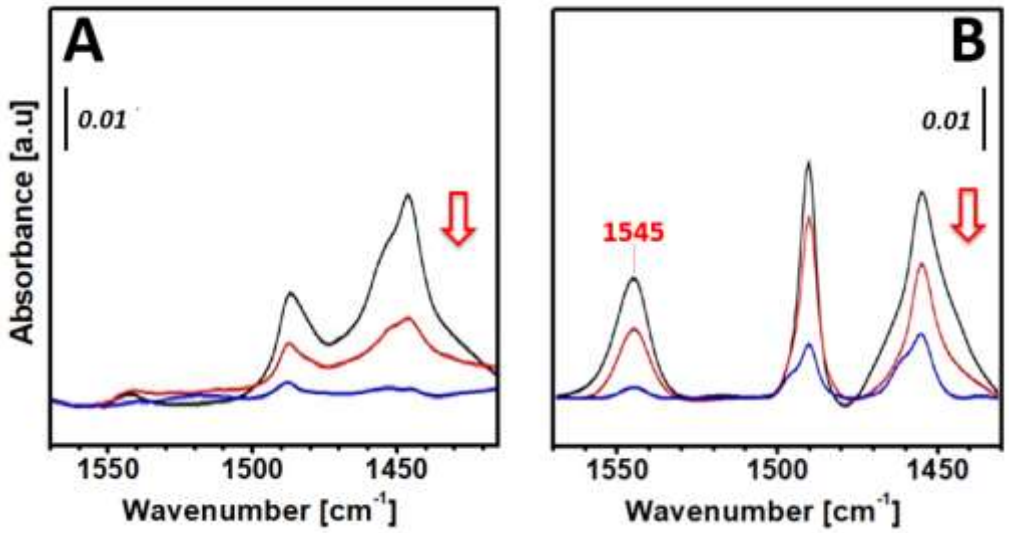

Fig. 46 FT-IR spectra of pyridine adsorbed on the proton forms of (A) SSZ-13-R and (B) SSZ-13-F-M25 after evacuation at 150, 300, and 500 °C (arrow indicates increasing evacuation temperature). Reproduced with permission from ref. 416, Copyright 2016 American Chemical Society.

5.5. Evaluating host-guest and guest-guest interactions

5.5.1. Environmentally driven studies

Inorganic host materials are used for a wide variety of environmentally beneficial applications.[417] Industrial wastewater, sewage, or rainfall/irrigation runoff may contain detrimental additives in concentrations that make them unsuitable for human and animal consumption. Impacted waters may require decontamination before it can be returned safely into the aquatic ecosystem. Among the multitude of physical, chemical, and biological

methods suitable for the removal of contaminants from water, adsorption seems to be the most efficient and cost-effective method.

In this context, if the combination among the spectroscopic investigations and computational modelling is still not routinely adopted in the definition of properties of porous solid matrices for environmental applications, its combined application to elucidate the interactions between 2D/3D systems and guest molecules (host-guest interactions) or between guest species (guest-guest interactions) confined in the voids of porous and layered systems is even less common to find in the literature. The reason for this infrequent approach is due to several factors here synthesized: (i) the experimental conditions allowing the observation of the host-guest and guest-guest adducts cannot be easy to reproduce switching from one spectroscopic technique to another as is the case of gaseous substances loaded on solid supports (an example of possible experimental setup is described in the first part of this review, Chapter 3, Fig. 8); (ii) the stabilization energy involved in possible host-guest as well as guest-guest arrangements can be small as is in the case of van der Walls (vdW) forces, thus making the observed/calculated signal/value unsuitable to predict the real and more stable conformation; (iii) the formation of clusters may depend on several interacting portions that spread the overall stabilizing effect on molecular scale and make difficult the observation of circumscribed and well defined effects.

As far as the study of the host-guest and guest-guest interactions in 3D systems is concerned, their involvement has been recently observed in high silica zeolite-based technologies for impacted waters and gas purification.

The occurrence of sulfonamide antibiotics in water bodies is an emerging environmental topic that is related to the diffusion of antibiotic resistance in the environment. In this context, high silica zeolite Y was successfully used to remove high amount of environmentally persistent sulfonamides (fully occupied faujasite supercages at the maximum loading capacity) from water with favourable adsorption kinetics (equilibrium time $\leq$1 min). The sulfonamide antibiotics irreversibly adsorbed in the pore of zeolite Y were deeply investigated by IR and ssNMR analysis augmented by calculations at the DFT level.[24,418,419] The comparison among the computed and experimental IR signals of sulfamethoxazole sulfonamide in CH_2Cl_2 and adsorbed in the zeolite Y allowed to define medium-weak and cooperative H-bonds and multiple vdW forces involved in the host-guest interactions.[418] In addition, the amide and imide tautomeric form of other sulfonamide antibiotics (namely, sulfathiazole, sulfamerazine, sulfadimethoxine, and sulfadoxine) adsorbed by the same zeolite Y was clearly defined for the first time by a combined FT-IR, $^{15}N\{^{1}H\}$CPMAS NMR

and DFT calculation approach, and H-bondings were described for those embedded in dimeric form.[24] The adsorption of sulfamethoxazole from water was also studied in the presence of model molecules of natural phenolic compounds (namely, vanillin and caffeic acid) always occurring in natural waters.[419] The coadsorption of the antibiotic and vanillin by the zeolite Y occurred in the range of pH typical of natural waters (5-8) through H-bonding between the carbonyl oxygen of vanillin and the heterocycle NH of sulfamethoxazole in amide form as defined by FT-IR analysis in agreement with the adduct stabilization energies computed in vacuum at the DFT level (56.2 kcal mol^{-1}) with respect to the isolated molecules. These findings indicate that the presence of phenolic compounds in aqueous media do not limit the adsorption performance of the high silica zeolite Y toward sulfonamide antibiotics and confirm its suitability for separation processes in natural waters.

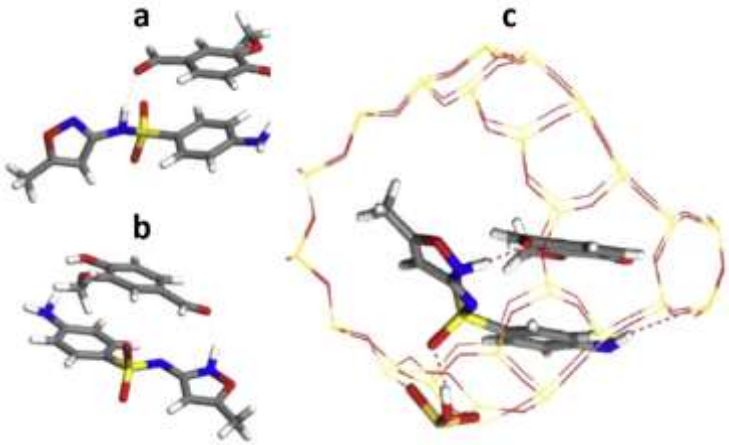

Fig. 47 DFT optimized structures of sulfamethoxazole antibiotic + vanillin complex with antibiotic in amide (a) and imide form (b) in vacuo and in the zeolite cage (c) framework. Reproduced with permission from ref. 410. Copyright 2016 Elsevier Ltd.

Recently, high silica zeolites are also gaining a special attention for environmental applications finalized to waste gas purification and hydrocarbons traps. Control of volatile pollutants is of major concern to the oil and chemical industries where air pollutants originate from breathing and loading losses from storage tanks, venting of process vessels, leaks from piping and equipment, wastewater streams, and heat exchange systems. An application of the combined spectroscopic and computational approach to quantify the co-adsorption of *n*-hexane and toluene as molecules representative of fuel-based aliphatic and aromatic components via gas phase in confined space of high silica zeolite Y and ZSM-5 is available.[420–422]

In the study of Sacchetto *et al*. FT-IR and ssNMR spectroscopy were used to elucidate the type and strength of the host-guest and guest-guest interactions between the model molecules singly adsorbed on the zeolites surfaces at different loadings/pressures.[420] At low loading, toluene displayed π-H-bondings with zeolite silanols (more numerous in Y than in ZSM-5) while at higher dosages vdW interactions became more pronounced. In *n*-hexane adsorption, dispersion forces mainly were those driving the adsorption by both zeolites. The interactions between the silica surfaces and each pollutant computed at the DFT level, and supplemented by empirical formulation of dispersion energies, led to estimate the relevance of dispersion forces to stabilize the pollutant molecules (especially *n*-hexane) at the internal of zeolite cavities and/or cages.

To quantify each single constituent of a mixture adsorbed onto solid sorbents, the definition of specific molar absorption coefficients in adsorbed form can be suitable. In this context, the quantification of gaseous *n*-hexane and toluene coadsorbed into zeolites Y and ZSM-5 porosities has been addressed by a combination of FT-IR and microgravimetric analysis of each single molecule adsorbed on the two supports.[421,422]

Different molar absorption coefficients of *n*-hexane at 1380 cm^{-1} (methyl bending mode) were derived (0.278±0.018 and 0.491±0.032 cm μmol^{-1} for Y and ZSM-5, respectively) owing to a significant change of the dipole moment of the methyl group adsorbed on the two solids.[421] Similarly, the estimation of the molar absorption coefficients at 1605 cm^{-1} (C=C stretching mode) of toluene adsorbed on the same supports resulted quite different for Y and ZSM-5 (0.224 ± 0.019 and 0.378 ± 0.030 cm μmol^{-1}, respectively).[422] The different environment experienced by *n*-hexane or toluene molecules adsorbed inside the porosities of the two zeolites was confirmed by computational modeling.[421,422] These findings reveal that the use of probe molecules for quantitative measurements of surface sites has to be judiciously adopted, especially if adsorption occurs in the restricted spaces of microporous materials.

This approach allowed determining for the first time the optical adsorption isotherms of both toluene and *n*-hexane coadsorbed on the zeolite Y and ZSM-5 from an equimolar gas mixture.[422] Different toluene and *n*-hexane adsorption regimes were shown by each zeolite: Y revealed more affine for toluene whereas ZSM-5 for *n*-hexane. Complementary solid state ^{1}H and ^{13}C NMR experiments at variable temperature provided more insights on the local environment that the pollutants experience inside the zeolites pores. The topology of MFI zeolite influences the diffusion of *n*-hexane: the aliphatic molecules are able to occupy both

linear and zigzag channel types so that they do not allow toluene to arrange at the intersection channel where molecules are generally favorably adsorbed.

The confinement effect of zeolite framework was also observed to play crucial roles in governing the ^{1}H NMR chemical shifts of adsorbed pyrrole as a probe molecule over basic catalysts.[85] Here, the adsorption structures and the corresponding ^{1}H chemical shifts of pyrrole H-bonded over various zeolites (namely, LiY, NaZSM-5, NaY, and KY) with varied intrinsic base strengths was systematically investigated by using a combined NMR experiment and theoretical calculation approach. Since both oxygen and nitrogen atoms could act as framework basic sites, the so-called intrinsic basicity is dependent on the complex framework structure and chemical composition. DFT calculations were employed to explore the adsorption structures and ^{1}H chemical shifts of pyrrole adsorbed over the zeolites. Based on a generic 8T zeolite ($(SiH_3)_3$-Si-X-Si-O-$(SiH_3)_3$, X = O or NH), various calculated models with different Si−H bond lengths were constructed to represent the basic sites with varied strengths and used to predict the pyrrole adsorption structures as well as the ^{1}H chemical shifts. The correspondence of larger ^{1}H chemical shift of adsorbed pyrrole to stronger basic site on solid catalysts was demonstrated by experimental results. A linear correlation between the ^{1}H chemical shift of adsorbed pyrrole and the proton affinity value of solid bases was theoretically found to be independent from the basic central atoms (e.g., O or N). The influence of confinement effect on the adsorption structures and ^{1}H chemical shifts of pyrrole over basic zeolite catalysts with respect to mesoporous Si-MCM-41 decreased the ^{1}H chemical shift by ca. 0.4 ppm.

5.5.2. Supramolecular organization

Supramolecular organizations inside zeolite nanochannels represent a challenging research field for electronic properties and potential technological applications. A regime not investigated in applications yet and that might have great potential for future development in this field is the confinement of close-packed dye molecules. In this context, K^+ zeolite L (LTL-framework type, Si/Al ratio 2.9) was maximally loaded with fluorenone molecules via gas phase and the composite (1.5 fluorenone molecules per L unit cell) investigated by an integrated experimental and computational approach.[423] As revealed by comparing ATR-IR spectra of fluorenone (both solid and in cyclohexane solution) to the molecules maximally loaded in the zeolite, the composite arranged to concomitantly maximize the π-stacking of fluorenone (intermolecular guest-guest interactions) and to allow the carbonyl group to

interact with a K^+ (host−guest interactions). DFT calculations were performed on a series of models for the composite. The PBE approximation with periodic boundary conditions and Grimme corrections for the guest-guest interactions was applied throughout. The calculated stabilization energy of the resulting minimum energy structure with respect to the isolated components equaled to −266.5 kJ mol^{-1}. The water molecules inside the packed channel were found to arrange to maximize hydrogen bond interactions, thus providing further stabilization to the system without altering the guest distribution, which is governed by the stronger guest-guest and host-guest interactions. The quasi 1-D noncovalent supramolecular nanoladders running along the zeolite channels, formed by pairs of π-stacked fluorenone molecules, hold some resemblance with the structure of solid fluorenone pairs. However, the confinement inside the zeolite channels and the different dimensions of the guest molecule and the zeolite unit cell prevent the connectivity of consecutive pairs of molecules like in crystalline fluorenone. The identification of the continuous and quasi 1-D dye nanostructure self-assembled into a zeolite, accompanied by the understanding of the interplay of host−guest/guest−guest interactions governing supramolecular organization at the high packing conditions gathered in this study, strongly suggests that high-loading regimes deserve to be deeply investigated to design dye−zeolite composites for innovative optical devices.

5.5.3. The reactivity in confined space

The potential use of specific drugs is often hindered by oxidative processes that might be limited by their confinement into inorganic matrixes as covered by the research field on drug encapsulation. This is also the case of the amino acid L-3,4-dihydroxyphenylalanine (L-DOPA) in the treatment of Parkinson's disease that is hindered by an oxidative polymerization that passes through the cyclized leucodopachrome and dopachrome forms up to melanin.[424] In this study, the complex oxidation mechanism of L-DOPA adsorbed by water solution at pH 3.1 and 5.9 on a synthesized zeolite Beta has been addressed by a multidisciplinary IR, Raman, ssNMR and periodic DFT investigation. The zeolite Beta in Na^+ form and a Si/Al ratio = 12 was synthesized and loaded with L-DOPA at about 9% wt. The determination of the neutral, zwitterionic, cationic, or anionic state of L-DOPA in the zeolite was elucidated by Raman-IR and NMR findings that highlighted the presence of -NH_3^+ and -COOH groups in L-DOPA. The molecular modeling revealed that an ion

exchange occurs between the protonated form of DOPA and its derivatives and the Na^+ cations in zeolite micropores. The results can be used to limit the L-DOPA polymerization by combining the steric effect of zeolite matrix and the condition of amino acid immobilization.

As far as the catalytic processes in 3D microporous systems are concerned, generally, the transformations of reactants start with polarization and protonation by the acid sites in zeolites. Thus, the charge distribution and its subtle change in zeolite channels are considered to drive and influence adsorption and reaction energetics. In this context, several studies adopting a multidisciplinary approach to evaluate the activation state of reagents within the solids' porosities can be found in the literature.

Esterification of carboxylic acids, as promising candidates to replace petroleum fuels, by solid acid catalysts is a very important process in organic synthesis as well as in the fuel industry as it is considered an alternative "green" route for the use of free fatty acids and bio-oils in esterification reactions. In the literature, four models for the first steps of adsorption mechanism for acetic acid and alcohols by Brønsted acid sites (BAS) of H-zeolites have been postulated (i.e. alcohol adsorption, acetic acid adsorption either by carboxylic OH or C=O and a co-adsorbed methanol and acetic acid complex). The mechanism of the first step of esterification has been clarified in H-Beta zeolite (SiO_2/Al_2O_3 = 38) with IR investigations coupled with DFT calculations at M06e2X/6-31G(D) level.[328] In the study, though it was not possible to discriminate between stepwise or co-adsorption, it was revealed that acetic acid is molecularly adsorbed by the carbonyl group on the catalyst BAS and with the OH group oriented to the Al-O-Si bridge. The complexes where the acetic acid is adsorbed by the carbonyl group are clearly the most stable ones as indicated by DFT calculations.

Another research field where the definition of microporous catalysts BAS is of utmost importance is the cracking of alkanes. A combined NMR and computational study to elucidate the BAS in ZSM-5 zeolite with different Si/Al ratio (namely, 16, 25, 40 and 140) has been recently adopted.[425] The concentrations of BAS and Lewis acid site (LAS) of the catalysts were quantified by IR spectroscopic measurements using pyridine. ^1H MAS NMR spectra provided quantitative information about different proton species, while ^1H DQ MAS NMR spectra elucidated the inter-nuclear proximity between the same or different ^1H species. ^{13}C MAS NMR spectra revealed a more pronounced polarization of adsorbed acetone and alkanes (i.e. C3-C5) in zeolites proximal BAS with subsequent cracking at higher turnover rates than isolated BAS. Apparent activation energies were found similar on the catalysts with different concentrations of isolated and adjacent BAS, while apparent activation entropies become less negative at higher BAS concentrations. Kinetic experiments in

conjunction with adsorption measurement and DFT calculations proved that cracking rates at these Al-site pairs are mainly due to more positive intrinsic activation entropies, thus suggesting that the protonation transition state occurs later along the reaction coordinate on adjacent BAS. In addition, adjacent BAS were found to favor cracking over dehydrogenation and central cracking over terminal cracking.

Recently, a new alternative route to produce propene from renewable feedstock is considered the direct conversion of ethene to propene (ETP), particularly when it is combined with the dehydration of ethanol/bio-ethanol to ethene be opened thereafter. In this context, a combination of IR and ssNMR has been applied to study the reaction and deactivation mechanisms of microporous catalysts.[426] Among several materials tested, dealuminated H-SSZ-13 zeolite, consisting of chabazite cages connected via 8MR windows, possessed the highest adsorption capacity for ethene and exhibited the best activity in the ETP conversion. The reaction mechanism of H-SSZ-13 during the ETP process was clarified by following the BAS evolution during the catalyst lifetime by *in situ* IR and ^{1}H SS NMR. While the number of accessible BAS decreased as revealed by IR and NMR, the number of naphthalene-based carbenium ions increased (ammonia was used as a trap to confirm the ion formation) during the highly active reaction period of the catalyst, thus indicating that these ions play a key role as catalytically active intermediates in the ETP conversion.

While conjugated carbocations like cyclic alkenyl and aromatic carbenium ions readily stabilized by BAS of solid acids can be observed by ssNMR and IR spectroscopy, the observation of short chain carbocations on solid acids due to their extremely short lifetime and high reactivity is challenging. In this context, *tert*-butyl carbocation was unambiguously identified by a combined experimental and computational approach.[427] In this work, the ^{13}C-labeled *tert*-butyl carbocation was captured by co-fed ammonia to stabilize the highly reactive species formed by *tert*-butanol dehydration at the BAS of H-ZSM-5 zeolite and its structure and host/guest interactions with the zeolite framework were determined by ^{13}C–^{13}C homonuclear and ^{13}C–^{27}Al heteronuclear correlation ssNMR and DFT theoretical calculations. The *tert*-butyl carbocation could be stabilized in the zeolite channel and the strong confinement effect of the framework significantly stabilized the cation as indicated by the calculated large vdW interaction region combined to the small repulsive region (Fig. 48). The occurrence of strong vdW interactions between the cations and the zeolite BAS were confirmed by ^{13}C–^{27}Al Symmetry based Resonance-Echo Saturation Pulse Double-Resonance (S-RESPDOR) experiments.

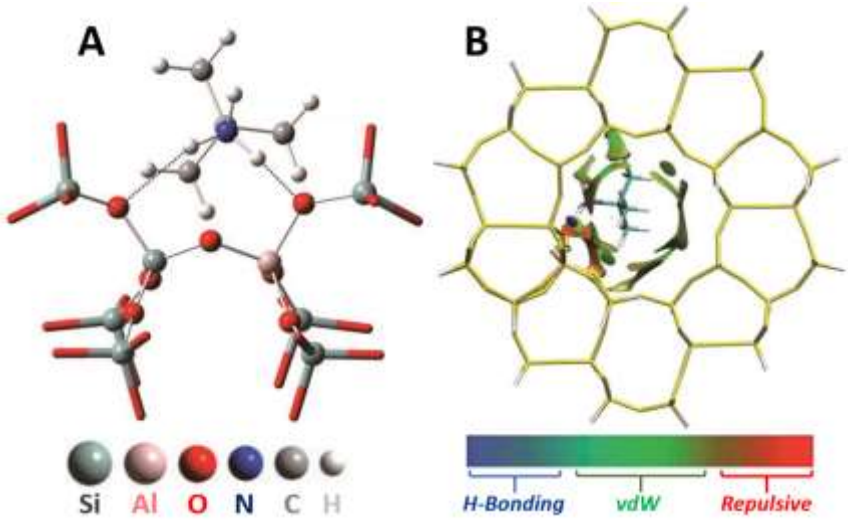

Fig. 48 (a) The local structure of the tert-butylamine cation confined in a 72T cluster model of H-ZSM-5 zeolite, in which H-bonds between the oxygen atom of the zeolite framework and the hydrogen atoms of ammonia are given. (b) Host-guest interactions between the tert-butylamine cation and the ZSM-5 zeolite framework. Reproduced with permission from ref. 427. Copyright 2016 The Royal Society of chemistry.

Recently the effect of zeolitic restricted space on occluded structure directing agents exposed to oxidation has been addressed by a combined IR-Raman and ^{13}C MAS NMR study.[428,429] The combination of these techniques allowed to observe that hexamethyleneimine restricted in MOR and $AlPO_4$-5 channels in its protonated form underwent different oxidation pathways when exposed to H_2O_2.[428] AFI topology structure allowed the oxidation of the structure directing agent to hydrocarbons and some other amines whereas the MOR one preserved hexamethyleneimine from oxidation. Both hybrid materials, as well as oxidized hybrid $AlPO_4$-5, showed interesting applications for water purification against Ni(II).

A similar investigation was extended to ferrierite (SiO_2/Al_2O_3 = 30) and sodalite (both pure silica and SiO_2/Al_2O_3 = 20) crystalized by etylene glycol.[429] Although ^{13}C MAS NMR revealed ethylene glycol in FER and SOD in the same state, sodalitic β cage prevented the organic compound against oxidation when exposed to H_2O_2 or HIO_4. A combined Raman and ^{13}C MAS NMR analysis of the oxidized hybrid FER indicated the formations of alkanes and alcohols in the presence of H_2O_2 whereas alkynes, acetals and ketals were revealed after HIO_4 treatment. The fact that the oxidation of ethylene glycol occluded in ferrierite gives oxidation products that are different from the bulk reaction and different depending on the used oxidant opens new opportunities for further research of molecular reactions on inorganic hybrids.

6. Future perspective and outlook

The examples in this review demonstrate that complete information about the structure-property relationships in layered or porous materials is hardly provided by experimental or computational approaches alone, whereas a suite of complementary multi-technique approaches is very useful for the study of pore morphology, nature, strength and concentration of active sites. Integrated multi-technique approaches involving ssNMR and FT-IR spectroscopy along with various computational techniques will become a norm for the full characterization in most of the fundamental and applied areas of 2D layered and 3D porous solids.

The advances in both the experimental (especially FT-IR and ssNMR spectroscopy) and computational techniques paved the way to describe in detail all the aspects of such solids from structure prediction to synthesis, mechanistic as well as kinetic investigation of nucleation, formation, growth and crystallization, along with structure-property relationship study and applications. Among the experimental approaches, ssNMR spectroscopy has demonstrated a high versatility, though FT-IR study of probe molecules (especially those with weak acid/base character that does not alter the chemical nature of the probed surface sites) is still the technique of choice for monitoring strength and distribution of catalytic active sites. However, there is little doubt that many new experimental ssNMR spectroscopic approaches utilizing dipole-dipole interactions, quadrupole interactions, and indirect spin-spin (j) coupling will be emerging in the near future. Improving the NMR sensitivity to probe surface structures in porous solids needs particular emphasis. In this respect, DNP surface enhanced NMR spectroscopy is a promising tool for the future. As hinted by the studies selected to exemplify the advantages of employing computational techniques, future research will be shaped by the development of novel computational strategies that are capable of taking into account the time averaging of chemical shifts for faster events and will improve the accuracy of computation based predictions.

On the other hand, the combination of ever increasing computing power and development of more efficient models and algorithms has completely changed the range of applicability of the theoretical modelling in the last decade and this trend is expected to continue in the future too. It is now common to simulate hundreds of atoms (even including dynamical averages) at the ab initio level, and up to tens of thousands of atoms with classical force fields (and these

levels can be largely overpassed with the aid of dedicated supercomputing facilities). As for the models, several new density functionals are becoming popular for applications in different fields, reaching chemical accuracy; a great improvement in the description of weak interactions has been achieved by semi-empirical corrections accounting for van der Waals interactions specifically parameterized for DFT. Finally, polarizable and chemically accurate force fields for molecular dynamics and Monte Carlo simulations are being developed also with dispersion-corrected ab initio calculations.

Although the synthesis of a variety of layered and porous solids has been reported in the recent years, a number of challenges remain. For example, layered and porous solids for single-site catalysis or chiral zeolites for asymmetric heterogeneous catalysis or thermally stable extra-large pore solids for natural product as well as heavy oil catalysis are highly desirable. Transport limitations for molecular traffic can be overcome by employment of materials with tailored hierarchical porosity. In this regard, large mesoporous solids with conventional intrinsic catalytic properties and (hydro)thermal stability would be outstanding candidates for novel applications in heterogeneous catalysis. Again, owing to the complexity of specifically designed catalysts, only a suite of combined experimental and theoretical approaches, as those described in this review, may guarantee an in-depth characterization of active surface sites.

7. Conflicts of interest

There are no conflicts to declare

8. Acknowledgement

The authors thank the students, postdoctoral co-workers and collaborators who have contributed to the development and understanding of layered and porous solids all along the last twenty years of work. Their achievements have been reached with the aid of funding from several sources: the European Union (EU) Horizon 2020 Research and Innovation Program (MULTI2HYCAT - Grant No 720783); EU under 7thFP (GLOBASOL - Grant No 309194; INNOVASOL - Grant No NMP3-SL-2009-227057); the Italian Ministry for

Education, University and Research through PRIN2008 Program (ZeoNAq - Grant No 2008BL2NWK), PRIN2015 Program (MethaPore - Grant No 2015CTEBBA; Green4Water - Grant No PRIN2015AKR4HX); Compagnia di San Paolo (HEPYCHEM and MASTERLIGHT projects); University of Piemonte Orientale A. Avogadro (Italy); Research Center for Non-Conventional Energy, Istituto ENI Donegani – Environmental Technologies (Novara, Italy).

9. References

1 J. Li, A. Corma and J. Yu, *Chem. Soc. Rev.*, 2015, **44**, 7112–7127.

2 W. J. Roth, P. Nachtigall, R. E. Morris and J. Čejka, *Chem. Rev.*, 2014, **114**, 4807–4837.

3 C.-Y. Wu, W. J. Wolf, Y. Levartovsky, H. A. Bechtel, M. C. Martin, F. D. Toste and E. Gross, *Nature*, 2017, **541**, 511–515.

4 M. Orazov and M. E. Davis, *Proc. Natl. Acad. Sci.*, 2015, **112**, 11777–11782.

5 G. P. M. Bignami, D. M. Dawson, V. R. Seymour, P. S. Wheatley, R. E. Morris and S. E. Ashbrook, *J. Am. Chem. Soc.*, 2017, **139**, 5140–5148.

6 M. H. Levitt, *Spin dynamics: basics of nuclear magnetic resonance*, John Wiley & Sons, Chichester, England; Hoboken, NJ, 2nd ed., 2008.

7 M. J. Duer, *Introduction to solid-state NMR spectroscopy*, Blackwell, Oxford, UK; Malden, MA, 2004.

8 N. B. Colthup, L. H. Daly and S. E. Wiberley, *Introduction to infrared and Raman spectroscopy*, Academic Press, Boston, 3rd ed., 1990.

9 G. Socrates, *Infrared and Raman characteristic group frequencies: tables and charts*, Wiley, Chichester, third ed., repr. as paperback., 2010.

10 C. J. Cramer, *Essentials of computational chemistry: theories and models*, Wiley, Chichester, West Sussex, England; Hoboken, NJ, 2nd ed., 2004.

11 T. Blasco, *Chem. Soc. Rev.*, 2010, **39**, 4685–4702.

12 S. Bordiga, C. Lamberti, F. Bonino, A. Travert and F. Thibault-Starzyk, *Chem. Soc. Rev.*, 2015, **44**, 7262–7341.

13 H. Koller and M. Weiß, in *Solid State NMR*, ed. J. C. C. Chan, Springer Berlin Heidelberg, Berlin, Heidelberg, 2011, vol. 306, pp. 189–227.

14 E. Brunner, H. G. Karge and H. Pfeifer, *Z. Für Phys. Chem.*, 1992, **176**, 173–183.

15 Y. Hayashi, A. Miyaji, K. Motokura, N. Asakawa and T. Baba, *J. Phys. Chem. C*, 2016, **120**, 9207–9217.

16 R. Ahlrichs, M. Bär, M. Häser, H. Horn and C. Kölmel, *Chem. Phys. Lett.*, 1989, **162**, 165–169.

17 M. J. Frisch *et al*., *Gaussian*, Gaussian, Inc., Wallingford CT, 2016.

18 K. Aidas, C. Angeli, K. L. Bak, V. Bakken, R. Bast, L. Boman, O. Christiansen, R. Cimiraglia, S. Coriani, P. Dahle, E. K. Dalskov, U. Ekström, T. Enevoldsen, J. J. Eriksen, P. Ettenhuber, B. Fernández, L. Ferrighi, H. Fliegl, L. Frediani, K. Hald, A. Halkier, C. Hättig, H. Heiberg, T. Helgaker, A. C. Hennum, H. Hettema, E. Hjertenaes, S. Høst, I.-M. Høyvik, M. F. Iozzi, B. Jansík, H. J. A. Jensen, D. Jonsson, P. Jørgensen, J. Kauczor, S. Kirpekar, T. Kjaergaard, W. Klopper, S. Knecht, R. Kobayashi, H. Koch, J. Kongsted, A. Krapp, K. Kristensen, A. Ligabue, O. B. Lutnaes, J. I. Melo, K. V. Mikkelsen, R. H. Myhre, C. Neiss, C. B. Nielsen, P. Norman, J. Olsen, J. M. H. Olsen, A. Osted, M. J. Packer, F. Pawlowski, T. B. Pedersen, P. F. Provasi, S. Reine, Z. Rinkevicius, T. A. Ruden, K. Ruud, V. V. Rybkin, P. Sałek, C. C. M. Samson, A. S. de Merás, T. Saue, S. P. A. Sauer, B. Schimmelpfennig, K. Sneskov, A. H. Steindal, K. O. Sylvester-Hvid, P. R. Taylor, A. M. Teale, E. I. Tellgren, D. P. Tew, A. J. Thorvaldsen, L. Thøgersen, O. Vahtras, M. A. Watson, D. J. D. Wilson, M. Ziolkowski and H. Ågren, *Wiley Interdiscip. Rev. Comput. Mol. Sci.*, 2014, **4**, 269–284.

19 E. J. Baerends, *ADF2017*, SCM, Vrije Universiteit, Amsterdam, The Netherlands, 2017.

20 H.-J. Werner, P. J. Knowles, G. Knizia, F. R. Manby and M. Schütz, *Wiley Interdiscip. Rev. Comput. Mol. Sci.*, 2012, **2**, 242–253.

21 V. Barone, *J. Chem. Phys.*, 2005, **122**, 014108.
22 J. Bloino, *J. Phys. Chem. A*, 2015, **119**, 5269–5287.
23 R. Dovesi, A. Erba, R. Orlando, C. M. Zicovich-Wilson, B. Civalleri, L. Maschio, M. Rérat, S. Casassa, J. Baima, S. Salustro and B. Kirtman, *Wiley Interdiscip. Rev. Comput. Mol. Sci.*, 2018, **e1360**, 1–36.
24 I. Braschi, G. Paul, G. Gatti, M. Cossi and L. Marchese, *RSC Adv.*, 2013, **3**, 7427–7437.
25 T. Charpentier, M. C. Menziani and A. Pedone, *RSC Adv.*, 2013, **3**, 10550–10578.
26 S. E. Ashbrook and S. Sneddon, *J. Am. Chem. Soc.*, 2014, **136**, 15440–15456.
27 P. Blaha, K. Schwarz, P. Sorantin and S. B. Trickey, *Comput. Phys. Commun.*, 1990, **59**, 399–415.
28 M. Bak, J. T. Rasmussen and N. C. Nielsen, *J. Magn. Reson.*, 2000, **147**, 296–330.
29 C. J. Pickard and F. Mauri, *Phys. Rev. B*, 2001, **63**, No. 245101.
30 C. Bonhomme, C. Gervais, F. Babonneau, C. Coelho, F. Pourpoint, T. Azaïs, S. E. Ashbrook, J. M. Griffin, J. R. Yates, F. Mauri and C. J. Pickard, *Chem. Rev.*, 2012, **112**, 5733–5779.
31 W. Suëtaka and J. T. Yates, *Surface infrared and Raman spectroscopy: methods and applications*, Plenum Press, New York, 1995.
32 K. I. Hadjiivanov and G. N. Vayssilov, in *Advances in Catalysis*, Elsevier, 2002, vol. 47, pp. 307–511.
33 A. Vimont, F. Thibault-Starzyk and M. Daturi, *Chem. Soc. Rev.*, 2010, **39**, 4928–4950.
34 C. Lamberti, A. Zecchina, E. Groppo and S. Bordiga, *Chem. Soc. Rev.*, 2010, **39**, 4951–5001.
35 G. Busca, *Phys. Chem. Chem. Phys.*, 1999, **1**, 723–736.
36 M. Primet, J. Bandiera, C. Naccache and M. V. Mathieu, *J. Chim. Phys.*, 1973, **67**, 535–541.
37 M. Hunger, *Catal. Rev.*, 1997, **39**, 345–393.
38 A. A. Gabrienko, I. G. Danilova, S. S. Arzumanov, A. V. Toktarev, D. Freude and A. G. Stepanov, *Microporous Mesoporous Mater.*, 2010, **131**, 210–216.
39 E. Brunner, K. Beck, M. Koch, L. Heeribout and H. G. Karge, *Microporous Mater.*, 1995, **3**, 395–399.
40 L.-E. Sandoval-Díaz, J.-A. González-Amaya and C.-A. Trujillo, *Microporous Mesoporous Mater.*, 2015, **215**, 229–243.
41 N. S. Nesterenko, F. Thibault-Starzyk, V. Montouillout, V. V. Yuschenko, C. Fernandez, J.-P. Gilson, F. Fajula and I. I. Ivanova, *Microporous Mesoporous Mater.*, 2004, **71**, 157–166.
42 I. Miletto, C. Ivaldi, G. Paul, S. Chapman, L. Marchese, R. Raja and E. Gianotti, *ChemistryOpen*, 2018, **7**, 297–301.
43 C. Paze´, A. Zecchina, S. Spera, G. Spano and F. Rivetti, *Phys. Chem. Chem. Phys.*, 2000, **2**, 5756–5760.
44 Y. Jiang, J. Huang, W. Dai and M. Hunger, *Solid State Nucl. Magn. Reson.*, 2011, **39**, 116–141.
45 Z. Wang, L. Wang, Z. Zhou, Y. Zhang, H. Li, C. Stampfl, C. Liang and J. Huang, *J. Phys. Chem. C*, 2017, **121**, 15248–15255.
46 Z. Wang, L. Wang, Y. Jiang, M. Hunger and J. Huang, *ACS Catal.*, 2014, **4**, 1144–1147.
47 J. Huang, Y. Jiang, V. R. R. Marthala, B. Thomas, E. Romanova and M. Hunger, *J. Phys. Chem. C*, 2008, **112**, 3811–3818.
48 J. Huang, N. van Vegten, Y. Jiang, M. Hunger and A. Baiker, *Angew. Chem. Int. Ed.*, 2010, **49**, 7776–7781.
49 S. Li, Z. Zhao, R. Zhao, D. Zhou and W. Zhang, *ChemCatChem*, 2017, **9**, 1494–1502.

50 G. P. Holland, B. R. Cherry and T. M. Alam, *J. Phys. Chem. B*, 2004, **108**, 16420–16426.
51 F. Yin, A. L. Blumenfeld, V. Gruver and J. J. Fripiat, *J. Phys. Chem. B*, 1997, **101**, 1824–1830.
52 D. Coster, A. L. Blumenfeld and J. J. Fripiat, *J. Phys. Chem.*, 1994, **98**, 6201–6211.
53 S. Lang, M. Benz, U. Obenaus, R. Himmelmann, M. Scheibe, E. Klemm, J. Weitkamp and M. Hunger, *Top. Catal.*, 2017, **60**, 1537–1553.
54 A. Zecchina, L. Marchese, S. Bordiga, C. Pazè and E. Gianotti, *J. Phys. Chem. B*, 1997, **101**, 10128–10135.
55 R. Otomo, T. Nishitoba, R. Osuga, Y. Kunitake, Y. Kamiya, T. Tatsumi and T. Yokoi, *J. Phys. Chem. C*, 2018, **122**, 1180–1191.
56 S. M. Maier, A. Jentys and J. A. Lercher, *J. Phys. Chem. C*, 2011, **115**, 8005–8013.
57 D. Mauder, D. Akcakayiran, S. B. Lesnichin, G. H. Findenegg and I. G. Shenderovich, *J. Phys. Chem. C*, 2009, **113**, 19185–19192.
58 G. Crépeau, V. Montouillout, A. Vimont, L. Mariey, T. Cseri and F. Maugé, *J. Phys. Chem. B*, 2006, **110**, 15172–15185.
59 D. Fărcaşiu, R. Leu and A. Corma, *J. Phys. Chem. B*, 2002, **106**, 928–932.
60 M. Diab, K. Shreteh, N. Afik, M. Volokh, S. Abramovich, U. Abdu and T. Mokari, *Adv. Sustain. Syst.*, 2018, 1800001.
61 I. Miletto, G. Paul, S. Chapman, G. Gatti, L. Marchese, R. Raja and E. Gianotti, *Chem. Eur. J.,* 2017, **23**, 9952–9961.
62 A. Erigoni, S. H. Newland, G. Paul, L. Marchese, R. Raja and E. Gianotti, *ChemCatChem*, 2016, **8**, 3161–3169.
63 Y. Chu, Z. Yu, A. Zheng, H. Fang, H. Zhang, S.-J. Huang, S.-B. Liu and F. Deng, *J. Phys. Chem. C*, 2011, **115**, 7660–7667.
64 J. H. Lunsford, W. P. Rothwell and W. Shen, *J. Am. Chem. Soc.*, 1985, **107**, 1540–1547.
65 H.-M. Kao, C.-Y. Yu and M.-C. Yeh, *Microporous Mesoporous Mater.*, 2002, **53**, 1–12.
66 J. P. Osegovic and R. S. Drago, *J. Phys. Chem. B*, 2000, **104**, 147–154.
67 M. D. Karra, K. J. Sutovich and K. T. Mueller, *J. Am. Chem. Soc.*, 2002, **124**, 902–903.
68 S. Hayashi, K. Jimura and N. Kojima, *Microporous Mesoporous Mater.*, 2014, **186**, 101–105.
69 A. Zheng, S.-B. Liu and F. Deng, *Chem. Rev.*, 2017, **117**, 12475–12531.
70 L. Peng, P. J. Chupas and C. P. Grey, *J. Am. Chem. Soc.*, 2004, **126**, 12254–12255.
71 L. Peng and C. P. Grey, *Microporous Mesoporous Mater.*, 2008, **116**, 277–283.
72 G. Ertl, Ed., *Handbook of heterogeneous catalysis: 8 volumes*, WILEY-VCH, Weinheim, 2., completely rev. and enl. ed., 2008.
73 Y. Jiang, J. Huang, W. Dai and M. Hunger, *Solid State Nucl. Magn. Reson.*, 2011, **39**, 116–141.
74 A. Zheng, S. Li, S.-B. Liu and F. Deng, *Acc. Chem. Res.*, 2016, **49**, 655–663.
75 H. Fang, A. Zheng, Y. Chu and F. Deng, *J. Phys. Chem. C*, 2010, **114**, 12711–12718.
76 G. Li, X. Yi, L. Huang, J. Jiang, Z. Yu, Z. Liu and A. Zheng, *J. Phys. Chem. C*, 2017, **121**, 16921–16931.
77 S. Li, S.-J. Huang, W. Shen, H. Zhang, H. Fang, A. Zheng, S.-B. Liu and F. Deng, *J. Phys. Chem. C*, 2008, **112**, 14486–14494.
78 A. J. Milling, Ed., *Surface characterization methods: principles, techniques, and applications*, Marcel Dekker, New York, 1999.
79 W. Zhang, D. Ma, X. Liu, X. Liu and X. Bao, *Chem. Commun.*, 1999, 1091–1092.
80 W. Zhang, S. Xu, X. Han and X. Bao, *Chem. Soc. Rev.*, 2012, **41**, 192–210.

81 J. Čejka, A. Corma and S. Zones, Eds., *Zeolites and catalysis: synthesis, reactions and applications*, Wiley-VCH, Weinheim, 2010.
82 C. Bisio, G. Martra, S. Coluccia and P. Massiani, *J. Phys. Chem. C*, 2008, **112**, 10520–10530.
83 G. Martra, S. Coluccia, P. Davit, E. Gianotti, L. Marchese, H. Tsuji and H. Hattori, *Res. Chem. Intermed.*, 1999, **25**, 77–93.
84 M. Huang and S. Kaliaguine, *J. Chem. Soc. Faraday Trans.*, 1992, **88**, 751–758.
85 X. Yi, G. Li, L. Huang, Y. Chu, Z. Liu, H. Xia, A. Zheng and F. Deng, *J. Phys. Chem. C*, 2017, **121**, 3887–3895.
86 M. Sánchez-Sánchez and T. Blasco, *Chem. Commun.*, 2000, 491–492.
87 M. Sánchez-Sánchez, T. Blasco and A. Corma, *J. Phys. Chem. C*, 2008, **112**, 16961–16967.
88 M. Sánchez-Sánchez and T. Blasco, *Catal. Today*, 2009, **143**, 293–301.
89 A. A. Tsyganenko, N. V. Zakharov and P. D. Murzin, *Catal. Today*, 2014, **226**, 73–80.
90 D. Mordenti, P. Grotz and H. Knözinger, *Catal. Today*, 2001, **70**, 83–90.
91 V. Bosacek, *J. Phys. Chem.*, 1993, **97**, 10732–10737.
92 V. Bosáek, H. Ernst, D. Freude and T. Mildner, *Zeolites*, 1997, **18**, 196–199.
93 M. Hunger, U. Schenk, B. Burger and J. Weitkamp, *Angew. Chem. Int. Ed. Engl.*, 1997, **36**, 2504–2506.
94 E. Bosch, S. Huber, J. Weitkamp and H. Knözinger, *Phys. Chem. Chem. Phys.*, 1999, **1**, 579–584.
95 J. C. Lavalley, *Catal. Today*, 1996, **27**, 377–401.
96 M. Sánchez-Sánchez, T. Blasco and F. Rey, *Phys. Chem. Chem. Phys.*, 1999, **1**, 4529–4535.
97 E. Bosch, S. Huber, J. Weitkamp and H. Knözinger, *Phys. Chem. Chem. Phys.*, 1999, **1**, 579–584.
98 Y. Zhou, Y. Jin, M. Wang, W. Zhang, J. Xie, J. Gu, H. Wen, J. Wang and L. Peng, *Chem. Eur. J.,* 2015, **21**, 15412–15420.
99 D. Barthomeuf, *Catal. Rev.*, 1996, **38**, 521–612.
100 R. Bermejo-Deval, M. Orazov, R. Gounder, S.-J. Hwang and M. E. Davis, *ACS Catal.*, 2014, **4**, 2288–2297.
101 S. Ganapathy, K. Gore, R. Kumar and J.-P. Amoureux, *Solid State Nucl. Magn. Reson.*, 2003, **24**, 184–195.
102 J. Brus, L. Kobera, W. Schoefberger, M. Urbanová, P. Klein, P. Sazama, E. Tabor, S. Sklenak, A. V. Fishchuk and J. Dědeček, *Angew. Chem. Int. Ed.*, 2015, **54**, 541–545.
103 A. Zheng, S.-B. Liu and F. Deng, *Solid State Nucl. Magn. Reson.*, 2013, **55**–**56**, 12–27.
104 W. J. Roth, B. Gil, W. Makowski, B. Marszalek and P. Eliášová, *Chem. Soc. Rev.*, 2016, **45**, 3400–3438.
105 H. Yin and Z. Tang, *Chem. Soc. Rev.*, 2016, **45**, 4873–4891.
106 U. Costantino, F. Costantino, F. Elisei, L. Latterini and M. Nocchetti, *Phys. Chem. Chem. Phys.*, 2013, **15**, 13254–13269.
107 S. Chandra, S. Kandambeth, B. P. Biswal, B. Lukose, S. M. Kunjir, M. Chaudhary, R. Babarao, T. Heine and R. Banerjee, *J. Am. Chem. Soc.*, 2013, **135**, 17853–17861.
108 A. K. Geim and I. V. Grigorieva, *Nature*, 2013, **499**, 419–425.
109 M. Tsapatsis, *AIChE J.*, 2014, **60**, 2374–2381.
110 G. Alberti, J.-M. Lehn and J. L. Atwood, Eds., *Solid-state supramolecular chemistry: two- and three-dimensional inorganic networks*, Pergamon, Oxford, first ed., 1996.
111 C. Bisio, F. Carniato, G. Paul, G. Gatti, E. Boccaleri and L. Marchese, *Langmuir*, 2011, **27**, 7250–7257.

112 F. Carniato, C. Bisio, G. Gatti, E. Boccaleri, L. Bertinetti, S. Coluccia, O. Monticelli and L. Marchese, *Angew. Chem. Int. Ed.*, 2009, **48**, 6059–6061.
113 L. Ostinelli, S. Recchia, C. Bisio, F. Carniato, M. Guidotti, L. Marchese and R. Psaro, *Chem. Asian J.,* 2012, **7**, 2394–2402.
114 F. Olivero, F. Carniato, C. Bisio and L. Marchese, *Chem. Asian J.,* 2014, **9**, 158–165.
115 S. Sene, S. Bégu, C. Gervais, G. Renaudin, A. Mesbah, M. E. Smith, P. H. Mutin, A. van der Lee, J.-M. Nedelec, C. Bonhomme and D. Laurencin, *Chem. Mater.*, 2015, **27**, 1242–1254.
116 L. Pietronero and E. Tosatti, *Physics of Intercalation Compounds: Proceedings of an International Conference Trieste, Italy, July 6-10, 1981*, Springer Berlin Heidelberg, Berlin, Heidelberg, 1981.
117 M. Ogawa and K. Kuroda, *Chem. Rev.*, 1995, **95**, 399–438.
118 R. Ma and T. Sasaki, *Acc. Chem. Res.*, 2015, **48**, 136–143.
119 C. Bisio, M. Nocchetti and F. Leroux, *Dalton Trans.*, 2018, **47**, 2838–2840.
120 S. Yang, W. Fu, Z. Zhang, H. Chen and C.-Z. Li, *J. Mater. Chem. A*, 2017, **5**, 11462–11482.
121 N.-G. Park, M. Grätzel and T. Miyasaka, Eds., *Organic-Inorganic halide perovskite photovoltaics: from fundamentals to device architectures configurations and applications*, Springer, Cham, 2016.
122 E. Diau and P. Chen, Eds., *Perovskite solar cells: principle, materials, devices*, World Scientific, New Jersey, 2017.
123 A. Thankappan and S. Thomas, *Perovskite Photovoltaics - Basic to Advances*, Elsevier Academic Press, S.l., 2018.
124 M. Guidotti, R. Psaro, N. Ravasio, M. Sgobba, F. Carniato, C. Bisio, G. Gatti and L. Marchese, *Green Chem.*, 2009, **11**, 1173–1178.
125 F. Carniato, C. Bisio, R. Psaro, L. Marchese and M. Guidotti, *Angew. Chem. Int. Ed.*, 2014, **53**, 10095–10098.
126 L. A. Utracki, M. Sepehr and E. Boccaleri, *Polym. Adv. Technol.*, 2007, **18**, 1–37.
127 Y.-C. Lee, T.-H. Lee, H.-K. Han, W. J. Go, J.-W. Yang and H.-J. Shin, *Photochem. Photobiol.*, 2010, **86**, 520–527.
128 K. V. Rao, K. K. R. Datta, M. Eswaramoorthy and S. J. George, *Angew. Chem. Int. Ed.*, 2011, **50**, 1179–1184.
129 J. H. Park, B.-W. Kim and J. H. Moon, *Electrochem. Solid-State Lett.*, 2008, **11**, B171–B173.
130 M.-C. Tsui, Y.-L. Tung, S.-Y. Tsai and C.-W. Lan, *J. Sol. Energy Eng.*, 2010, **133**, 011002–011004.
131 D. Costenaro, G. Gatti, F. Carniato, G. Paul, C. Bisio and L. Marchese, *Microporous Mesoporous Mater.*, 2012, **162**, 159–167.
132 J. T. Kloprogge, *Clays Clay Miner.*, 1999, **47**, 529–554.
133 F. Carniato, C. Bisio, G. Gatti, M. Guidotti, L. Sordelli and L. Marchese, *Chem. Asian J.*, 2011, **6**, 914–921.
134 A. J. Patil, M. Li, E. Dujardin and S. Mann, *Nano Lett.*, 2007, **7**, 2660–2665.
135 H. He, R. L. Frost, T. Bostrom, P. Yuan, L. Duong, D. Yang, Y. Xi and J. T. Kloprogge, *Appl. Clay Sci.*, 2006, **31**, 262–271.
136 M. Richard-Plouet, S. Vilminot and M. Guillot, *New J. Chem.*, 2004, **28**, 1073–1082.
137 M. Jaber and J. Miehé-Brendlé, *Microporous Mesoporous Mater.*, 2008, **107**, 121–127.
138 M. D. Alba, M. A. Castro, M. M. Orta, E. Pavón, M. C. Pazos and J. S. Valencia Rios, *Langmuir*, 2011, **27**, 9711–9718.
139 Q. Tao, Y. Fang, T. Li, D. Zhang, M. Chen, S. Ji, H. He, S. Komarneni, H. Zhang, Y. Dong and Y. D. Noh, *Appl. Clay Sci.*, 2016, **132–133**, 133–139.

140 W. Li, L. Sun, L. Pan, Z. Lan, T. Jiang, X. Yang, J. Luo, R. Li, L. Tan, S. Zhang and M. Yu, *Eur. J. Pharm. Biopharm.*, 2014, **88**, 706–717.
141 K. Sato, K. Numata, W. Dai and M. Hunger, *Appl. Phys. Lett.*, 2014, **104**, 131901–131905.
142 H. Pálková, V. Hronský, V. Bizovská and J. Madejová, *Spectrochim. Acta. A. Mol. Biomol. Spectrosc.*, 2015, **149**, 751–761.
143 S. Cadars, R. Guégan, M. N. Garaga, X. Bourrat, L. Le Forestier, F. Fayon, T. V. Huynh, T. Allier, Z. Nour and D. Massiot, *Chem. Mater.*, 2012, **24**, 4376–4389.
144 U. Kielmann, G. Jeschke and I. García-Rubio, *Materials*, 2014, **7**, 1384–1408.
145 M. Jiménez-Ruiz, E. Ferrage, M. Blanchard, J. Fernandez-Castanon, A. Delville, M. R. Johnson and L. J. Michot, *J. Phys. Chem. C*, 2017, **121**, 5029–5040.
146 V. Marry, E. Dubois, N. Malikova, J. Breu and W. Haussler, *J. Phys. Chem. C*, 2013, **117**, 15106–15115.
147 L. J. Michot, E. Ferrage, M. Jiménez-Ruiz, M. Boehm and A. Delville, *J. Phys. Chem. C*, 2012, **116**, 16619–16633.
148 M. Jiménez-Ruiz, E. Ferrage, A. Delville and L. J. Michot, *J. Phys. Chem. A*, 2012, **116**, 2379–2387.
149 V. Marry, E. Dubois, N. Malikova, S. Durand-Vidal, S. Longeville and J. Breu, *Environ. Sci. Technol.*, 2011, **45**, 2850–2855.
150 Q. Qiao, H. Yang, J.-L. Liu, S.-P. Zhao and X.-M. Ren, *Dalton Trans.*, 2014, **43**, 5427–5434.
151 S. M. Auerbach, K. A. Carrado and P. K. Dutta, Eds., *Handbook of layered materials*, M. Dekker, New York, 2004.
152 J. Martins de Souza e Silva, G. Paul, J. Bendall, C. Bisio, L. Marchese and H. O. Pastore, *Phys. Chem. Chem. Phys.*, 2013, **15**, 13434–13445.
153 S. Bordiga, P. Ugliengo, A. A. Damin, C. Lamberti, G. Spoto, A. Zecchina, G. Spano, R. Buzzoni, L. Dalloro and F. Rivetti, in *Topics in Catalysis*, Springer/Plenum Publishers, 233 Spring ST, New York, NY 10013 USA, 2001, vol. 15 (1), pp. 43–52.
154 S. Vortmann, J. Rius, S. Siegmann and H. Gies, *J. Phys. Chem. B*, 1997, **101**, 1292–1297.
155 M. F. Iozzi, C. Bisio, T. Regi-Macedo, C. Airoldi, M. Cossi and L. Marchese, *J. Mater. Chem.*, 2009, **19**, 2610–2617.
156 J. I. Corredor, A. Cota, E. Pavón, F. J. Osuna and M. D. Alba, *Appl. Clay Sci.*, 2014, **95**, 9–17.
157 A. Clearfield and G. D. Smith, *Inorg. Chem.*, 1969, **8**, 431–436.
158 G. Alberti, U. Costantino, S. Allulli and N. Tomassini, *J. Inorg. Nucl. Chem.*, 1978, **40**, 1113–1117.
159 M. B. Dines and P. M. DiGiacomo, *Inorg. Chem.*, 1981, **20**, 92–97.
160 A. Clearfield, *J. Mol. Catal.*, 1984, **27**, 251–262.
161 G. Alberti, *Acc. Chem. Res.*, 1978, **11**, 163–170.
162 A. Clearfield, Ed., *Inorganic ion exchange materials*, CRC Press, Boca Raton, Fla, 1982.
163 L. A. Vermeulen and M. E. Thompson, *Chem. Mater.*, 1994, **6**, 77–81.
164 A. Clearfield, *Curr. Opin. Solid State Mater. Sci.*, 1996, **1**, 268–278.
165 A. Clearfield and K. Demadis, Eds., *Metal phosphonate chemistry: from synthesis to applications*, RSC Publishing, Cambridge, 2012.
166 G. Alberti, M. Casciola, A. Donnadio, P. Piaggio, M. Pica and M. Sisani, *Solid State Ion.*, 2005, **176**, 2893–2898.
167 A. Díaz, B. M. Mosby, V. I. Bakhmutov, A. A. Martí, J. D. Batteas and A. Clearfield, *Chem. Mater.*, 2013, **25**, 723–728.

168 S. He, X. Liu, H. Zhao, Y. Zhu and F. Zhang, *J. Colloid Interface Sci.*, 2015, **437**, 58–64.
169 D. S. Middlemiss, A. J. Ilott, R. J. Clément, F. C. Strobridge and C. P. Grey, *Chem. Mater.*, 2013, **25**, 1723–1734.
170 J. Zhu and Y. Huang, *Inorg. Chem.*, 2009, **48**, 10186–10192.
171 J. Zhu and Y. Huang, *Can. J. Chem.*, 2011, **89**, 803–813.
172 J. Cuny, J. R. Yates, R. Gautier, E. Furet, E. Le Fur and L. Le Pollès, *Magn. Reson. Chem.*, 2010, **48**, S171–S175.
173 Z. Yan, C. W. Kirby and Y. Huang, *J. Phys. Chem. C*, 2008, **112**, 8575–8586.
174 L. Mafra, J. Rocha, C. Fernandez, G. R. Castro, S. García-Granda, A. Espina, S. A. Khainakov and J. R. García, *Chem. Mater.*, 2008, **20**, 3944–3953.
175 M. D'Amore, C. Bisio, G. Talarico, M. Cossi and L. Marchese, *Chem. Mater.*, 2008, **20**, 4980–4985.
176 A. I. Khan and D. O'Hare, *J. Mater. Chem.*, 2002, **12**, 3191–3198.
177 S. Ishihara, P. Sahoo, K. Deguchi, S. Ohki, M. Tansho, T. Shimizu, J. Labuta, J. P. Hill, K. Ariga, K. Watanabe, Y. Yamauchi, S. Suehara and N. Iyi, *J. Am. Chem. Soc.*, 2013, **135**, 18040–18043.
178 B. F. Sels, D. E. De Vos and P. A. Jacobs, *Catal. Rev.*, 2001, **43**, 443–488.
179 F. Leroux and J.-P. Besse, *Chem. Mater.*, 2001, **13**, 3507–3515.
180 V. Srivastava, *J. Chem. Sci.*, 2013, **125**, 1207–1212.
181 U. Riaz and S. M. Ashraf, *Mini-Rev. Med. Chem.*, 2013, **13**, 522–529.
182 J. Zhao, X. Fu, S. Zhang and W. Hou, *Appl. Clay Sci.*, 2011, **51**, 460–466.
183 Z. Rezvani, F. Arjomandi Rad and F. Khodam, *Dalton Trans.*, 2015, **44**, 988–996.
184 D. Yan, Y. Zhao, M. Wei, R. Liang, J. Lu, D. G. Evans and X. Duan, *RSC Adv.*, 2013, **3**, 4303–4310.
185 S. P. Lonkar, B. Kutlu, A. Leuteritz and G. Heinrich, *Appl. Clay Sci.*, 2013, **71**, 8–14.
186 E. Conterosito, V. Gianotti, L. Palin, E. Boccaleri, D. Viterbo and M. Milanesio, *Inorganica Chim. Acta*, 2018, **470**, 36–50.
187 S. S. C. Pushparaj, N. D. Jensen, C. Forano, G. J. Rees, V. Prevot, J. V. Hanna, D. B. Ravnsbæk, M. Bjerring and U. G. Nielsen, *Inorg. Chem.*, 2016, **55**, 9306–9315.
188 A. O. Sjåstad, N. H. Andersen, P. Vajeeston, J. Karthikeyan, B. Arstad, A. Karlsson and H. Fjellvåg, *Eur. J. Inorg. Chem.*, 2015, **2015**, 1775–1788.
189 C. Vaysse, L. Guerlou-Demourgues and C. Delmas, *Inorg. Chem.*, 2002, **41**, 6905–6913.
190 Y. Liu, J. Su, W. Li and J. Wu, *Inorg. Chem.*, 2005, **44**, 3890–3895.
191 Y. Wang, P. Wu, Y. Li, N. Zhu and Z. Dang, *J. Colloid Interface Sci.*, 2013, **394**, 564–572.
192 V. R. R. Cunha, P. A. D. Petersen, M. B. Gonçalves, H. M. Petrilli, C. Taviot-Gueho, F. Leroux, M. L. A. Temperini and V. R. L. Constantino, *Chem. Mater.*, 2012, **24**, 1415–1425.
193 M. A. Rocha, P. A. D. Petersen, E. Teixeira-Neto, H. M. Petrilli, F. Leroux, C. Taviot-Gueho and V. R. L. Constantino, *RSC Adv.*, 2016, **6**, 16419–16436.
194 V. R. R. Cunha, V. A. Guilherme, E. de Paula, D. R. de Araujo, R. O. Silva, J. V. R. Medeiros, J. R. S. A. Leite, P. A. D. Petersen, M. Foldvari, H. M. Petrilli and V. R. L. Constantino, *Mater. Sci. Eng. C*, 2016, **58**, 629–638.
195 A. L. Costa, A. C. Gomes, M. Pillinger, I. S. Gonçalves and J. S. Seixas de Melo, *Langmuir*, 2015, **31**, 4769–4778.
196 Y. Yuan and W. Shi, *Appl. Clay Sci.*, 2012, **67–68**, 83–90.
197 S. Arias, J. G. Eon, R. A. S. San Gil, Y. E. Licea, L. A. Palacio and A. C. Faro, *Dalton Trans*, 2013, **42**, 2084–2093.

198 T. Baskaran, J. Christopher, M. Mariyaselvakumar and A. Sakthivel, *Eur. J. Inorg. Chem.*, 2017, **2017**, 2396–2405.
199 T. Li, W. Zhang, W. Chen, H. N. Miras and Y.-F. Song, *Dalton Trans.*, 2018, **47**, 3059–3067.
200 W. Bing, L. Zheng, S. He, D. Rao, M. Xu, L. Zheng, B. Wang, Y. Wang and M. Wei, *ACS Catal.*, 2018, **8**, 656–664.
201 Y. Chen, C. Li, J. Zhou, S. Zhang, D. Rao, S. He, M. Wei, D. G. Evans and X. Duan, *ACS Catal.*, 2015, **5**, 5756–5765.
202 J. Zhao, M. Shao, D. Yan, S. Zhang, Z. Lu, Z. Li, X. Cao, B. Wang, M. Wei, D. G. Evans and X. Duan, *J. Mater. Chem. A*, 2013, **1**, 5840–5846.
203 A. Guzmán-Vargas, J. Vazquez-Samperio, M. A. Oliver-Tolentino, G. Ramos-Sánchez, J. L. Flores-Moreno and E. Reguera, *Electrocatalysis*, 2017, **8**, 383–391.
204 A. C. Thenuwara, N. H. Attanayake, J. Yu, J. P. Perdew, E. J. Elzinga, Q. Yan and D. R. Strongin, *J. Phys. Chem. B*, 2018, **122**, 847–854.
205 J. Liu, J. Wang, B. Zhang, Y. Ruan, L. Lv, X. Ji, K. Xu, L. Miao and J. Jiang, *ACS Appl. Mater. Interfaces*, 2017, **9**, 15364–15372.
206 J. Xie, X. Zhang, H. Zhang, J. Zhang, S. Li, R. Wang, B. Pan and Y. Xie, *Adv. Mater.*, 2017, **29**, 1604765.
207 S.-M. Xu, T. Pan, Y.-B. Dou, H. Yan, S.-T. Zhang, F.-Y. Ning, W.-Y. Shi and M. Wei, *J. Phys. Chem. C*, 2015, **119**, 18823–18834.
208 X. Liu, X. Zhao, Y. Zhu and F. Zhang, *Appl. Catal. B Environ.*, 2013, **140–141**, 241–248.
209 K.-I. Kobayashi, T. Kimura, H. Sawada, K. Terakura and Y. Tokura, *Nature*, 1998, **395**, 677–680.
210 A. Sakai, T. Kanno, K. Takahashi, Y. Yamada and H. Adachi, *J. Appl. Phys.*, 2010, **108**, 103706.
211 X. Chen, S. Shen, L. Guo and S. S. Mao, *Chem. Rev.*, 2010, **110**, 6503–6570.
212 R. E. Schaak and T. E. Mallouk, *Chem. Mater.*, 2002, **14**, 1455–1471.
213 C. Wang, K. Tang, D. Wang, Z. Liu, L. Wang, Y. Zhu and Y. Qian, *J. Mater. Chem.*, 2012, **22**, 11086–11092.
214 Y. Wang, X. Zhu, X. Li, L. Wang, Y. Wang, Q. Hao and K. Tang, *J. Mater. Chem. A*, 2014, **2**, 15590–15597.
215 Y. Wang, C. Wang, L. Wang, Q. Hao, X. zhu, X. Chen and K. Tang, *RSC Adv.*, 2014, **4**, 4047–4054.
216 N. Toihara, Y. Yoneyama, A. Shimada, S. Tahara and Y. Sugahara, *Dalton Trans.*, 2015, **44**, 3002–3008.
217 A. Kessentini, M. Belhouchet, J. J. Suñol, Y. Abid and T. Mhiri, *J. Mol. Struct.*, 2013, **1039**, 207–213.
218 A. Kessentini, M. Belhouchet, J. J. Suñol, Y. Abid and T. Mhiri, *J. Lumin.*, 2014, **149**, 341–347.
219 T. Dammak, H. Boughzala, A. Mlayah and Y. Abid, *J. Lumin.*, 2016, **173**, 213–217.
220 A. Fernandes, D. McKay, S. Sneddon, D. M. Dawson, S. Lawson, R. Veazey, K. R. Whittle and S. E. Ashbrook, *J. Phys. Chem. C*, 2016, **120**, 20288–20296.
221 X. Wang, J. Adhikari and L. J. Smith, *J. Phys. Chem. C*, 2009, **113**, 17548–17559.
222 A. J. Lehner, D. H. Fabini, H. A. Evans, C.-A. Hébert, S. R. Smock, J. Hu, H. Wang, J. W. Zwanziger, M. L. Chabinyc and R. Seshadri, *Chem. Mater.*, 2015, **27**, 7137–7148.
223 J. Even, L. Pedesseau, J.-M. Jancu and C. Katan, *J. Phys. Chem. Lett.*, 2013, **4**, 2999–3005.
224 A. Fraccarollo, V. Cantatore, G. Boschetto, L. Marchese and M. Cossi, *J. Chem. Phys.*, 2016, **144**, 164701.

225 T. Margossian, S. P. Culver, K. Larmier, F. Zhu, R. L. Brutchey and C. Copéret, *Chem. Commun.*, 2016, **52**, 13791–13794.
226 Y. Li and J. Yu, *Chem. Rev.*, 2014, **114**, 7268–7316.
227 X. Zhang, D. Liu, D. Xu, S. Asahina, K. A. Cychosz, K. V. Agrawal, Y. A. Wahedi, A. Bhan, S. A. Hashimi, O. Terasaki, M. Thommes and M. Tsapatsis, *Science*, 2012, **336**, 1684–1687.
228 N. Sheng, Y. Chu, S. Xin, Q. Wang, X. Yi, Z. Feng, X. Meng, X. Liu, F. Deng and F.-S. Xiao, *J. Am. Chem. Soc.*, 2016, **138**, 6171–6176.
229 V. Sacchetto, C. Bisio, D. F. Olivas Olivera, G. Paul, G. Gatti, I. Braschi, G. Berlier, M. Cossi and L. Marchese, *J. Phys. Chem. C*, 2015, **119**, 24875–24886.
230 P. Horcajada, T. Chalati, C. Serre, B. Gillet, C. Sebrie, T. Baati, J. F. Eubank, D. Heurtaux, P. Clayette, C. Kreuz, J.-S. Chang, Y. K. Hwang, V. Marsaud, P.-N. Bories, L. Cynober, S. Gil, G. Férey, P. Couvreur and R. Gref, *Nat. Mater.*, 2010, **9**, 172–178.
231 P. Nugent, Y. Belmabkhout, S. D. Burd, A. J. Cairns, R. Luebke, K. Forrest, T. Pham, S. Ma, B. Space, L. Wojtas, M. Eddaoudi and M. J. Zaworotko, *Nature*, 2013, **495**, 80–84.
232 Y. Yan, S. Yang, A. J. Blake and M. Schröder, *Acc. Chem. Res.*, 2014, **47**, 296–307.
233 J.-R. Li, J. Sculley and H.-C. Zhou, *Chem. Rev.*, 2012, **112**, 869–932.
234 S. Furukawa, J. Reboul, S. Diring, K. Sumida and S. Kitagawa, *Chem. Soc. Rev.*, 2014, **43**, 5700–5734.
235 A. Cadiau, K. Adil, P. M. Bhatt, Y. Belmabkhout and M. Eddaoudi, *Science*, 2016, **353**, 137–140.
236 Y. He, W. Zhou, G. Qian and B. Chen, *Chem. Soc. Rev.*, 2014, **43**, 5657–5678.
237 B. E. G. Lucier, S. Chen and Y. Huang, *Acc. Chem. Res.*, 2018, **51**, 319–330.
238 M. Errahali, G. Gatti, L. Tei, G. Paul, G. A. Rolla, L. Canti, A. Fraccarollo, M. Cossi, A. Comotti, P. Sozzani and L. Marchese, *J. Phys. Chem. C*, 2014, **118**, 28699–28710.
239 J. Jiang and O. M. Yaghi, *Chem. Rev.*, 2015, **115**, 6966–6997.
240 A. J. Howarth, A. W. Peters, N. A. Vermeulen, T. C. Wang, J. T. Hupp and O. K. Farha, *Chem. Mater.*, 2017, **29**, 26–39.
241 O. M. Yaghi and H. Li, *J. Am. Chem. Soc.*, 1995, **117**, 10401–10402.
242 M. Kondo, T. Yoshitomi, H. Matsuzaka, S. Kitagawa and K. Seki, *Angew. Chem. Int. Ed. Engl.*, 1997, **36**, 1725–1727.
243 G. Ferey, *Science*, 2005, **309**, 2040–2042.
244 H. Furukawa, N. Ko, Y. B. Go, N. Aratani, S. B. Choi, E. Choi, A. O. Yazaydin, R. Q. Snurr, M. O'Keeffe, J. Kim and O. M. Yaghi, *Science*, 2010, **329**, 424–428.
245 T. M. McDonald, J. A. Mason, X. Kong, E. D. Bloch, D. Gygi, A. Dani, V. Crocellà, F. Giordanino, S. O. Odoh, W. S. Drisdell, B. Vlaisavljevich, A. L. Dzubak, R. Poloni, S. K. Schnell, N. Planas, K. Lee, T. Pascal, L. F. Wan, D. Prendergast, J. B. Neaton, B. Smit, J. B. Kortright, L. Gagliardi, S. Bordiga, J. A. Reimer and J. R. Long, *Nature*, 2015, **519**, 303–308.
246 J. E. Bachman, Z. P. Smith, T. Li, T. Xu and J. R. Long, *Nat. Mater.*, 2016, **15**, 845–849.
247 X. Cui, K. Chen, H. Xing, Q. Yang, R. Krishna, Z. Bao, H. Wu, W. Zhou, X. Dong, Y. Han, B. Li, Q. Ren, M. J. Zaworotko and B. Chen, *Science*, 2016, **353**, 141–144.
248 Z. Hu, B. J. Deibert and J. Li, *Chem. Soc. Rev.*, 2014, **43**, 5815–5840.
249 X. Zhao, X. Bu, T. Wu, S.-T. Zheng, L. Wang and P. Feng, *Nat. Commun.*, 2013, **4**, 2344.
250 M. Errahali, G. Gatti, L. Tei, L. Canti, A. Fraccarollo, M. Cossi and L. Marchese, *J. Phys. Chem. C*, 2014, **118**, 10053–10060.
251 J. B. DeCoste and G. W. Peterson, *Chem. Rev.*, 2014, **114**, 5695–5727.

252 V. Guillerm, D. Kim, J. F. Eubank, R. Luebke, X. Liu, K. Adil, M. S. Lah and M. Eddaoudi, *Chem. Soc. Rev.*, 2014, **43**, 6141–6172.
253 P. J. Waller, F. Gándara and O. M. Yaghi, *Acc. Chem. Res.*, 2015, **48**, 3053–3063.
254 M. Cossi, G. Gatti, L. Canti, L. Tei, M. Errahali and L. Marchese, *Langmuir*, 2012, **28**, 14405–14414.
255 T. K. Todorova, X. Rozanska, C. Gervais, A. Legrand, L. N. Ho, P. Berruyer, A. Lesage, L. Emsley, D. Farrusseng, J. Canivet and C. Mellot-Draznieks, *Chem. Eur. J.,* 2016, **22**, 16531–16538.
256 J. D. Evans, K. E. Jelfs, G. M. Day and C. J. Doonan, *Chem. Soc. Rev.*, 2017, **46**, 3286–3301.
257 P. Silva, S. M. F. Vilela, J. P. C. Tomé and F. A. Almeida Paz, *Chem. Soc. Rev.*, 2015, **44**, 6774–6803.
258 X. Li, Y. Liu, J. Wang, J. Gascon, J. Li and B. Van der Bruggen, *Chem. Soc. Rev.*, 2017, **46**, 7124–7144.
259 E. Barea, C. Montoro and J. A. R. Navarro, *Chem. Soc. Rev.*, 2014, **43**, 5419–5430.
260 W. Lu, Z. Wei, Z.-Y. Gu, T.-F. Liu, J. Park, J. Park, J. Tian, M. Zhang, Q. Zhang, T. Gentle III, M. Bosch and H.-C. Zhou, *Chem. Soc. Rev.*, 2014, **43**, 5561–5593.
261 J. Liu, L. Chen, H. Cui, J. Zhang, L. Zhang and C.-Y. Su, *Chem. Soc. Rev.*, 2014, **43**, 6011–6061.
262 A. Schneemann, V. Bon, I. Schwedler, I. Senkovska, S. Kaskel and R. A. Fischer, *Chem. Soc. Rev.*, 2014, **43**, 6062–6096.
263 A. Schoedel, M. Li, D. Li, M. O'Keeffe and O. M. Yaghi, *Chem. Rev.*, 2016, **116**, 12466–12535.
264 Y. Cui, B. Li, H. He, W. Zhou, B. Chen and G. Qian, *Acc. Chem. Res.*, 2016, **49**, 483–493.
265 S. M. J. Rogge, A. Bavykina, J. Hajek, H. Garcia, A. I. Olivos-Suarez, A. Sepúlveda-Escribano, A. Vimont, G. Clet, P. Bazin, F. Kapteijn, M. Daturi, E. V. Ramos-Fernandez, F. X. Llabrés i Xamena, V. Van Speybroeck and J. Gascon, *Chem. Soc. Rev.*, 2017, **46**, 3134–3184.
266 K. Sakaushi and M. Antonietti, *Acc. Chem. Res.*, 2015, **48**, 1591–1600.
267 S. Das, P. Heasman, T. Ben and S. Qiu, *Chem. Rev.*, 2017, **117**, 1515–1563.
268 J.-K. Sun, M. Antonietti and J. Yuan, *Chem. Soc. Rev.*, 2016, **45**, 6627–6656.
269 P. Falcaro, R. Ricco, C. M. Doherty, K. Liang, A. J. Hill and M. J. Styles, *Chem. Soc. Rev.*, 2014, **43**, 5513–5560.
270 P. Wu, J. Ruan, L. Wang, L. Wu, Y. Wang, Y. Liu, W. Fan, M. He, O. Terasaki and T. Tatsumi, *J. Am. Chem. Soc.*, 2008, **130**, 8178–8187.
271 J. Jiang, L. Jia, B. Yang, H. Xu and P. Wu, *Chem. Mater.*, 2013, **25**, 4710–4718.
272 B. Yang, J.-G. Jiang, K. Zhang and P. Wu, *Chem. Mater.*, 2016, **28**, 5295–5303.
273 Y. Asakura, Y. Sakamoto and K. Kuroda, *Chem. Mater.*, 2014, **26**, 3796–3803.
274 Z. Zhao, W. Zhang, P. Ren, X. Han, U. Müller, B. Yilmaz, M. Feyen, H. Gies, F.-S. Xiao, D. De Vos, T. Tatsumi and X. Bao, *Chem. Mater.*, 2013, **25**, 840–847.
275 M. Opanasenko, W. O. Parker, M. Shamzhy, E. Montanari, M. Bellettato, M. Mazur, R. Millini and J. Čejka, *J. Am. Chem. Soc.*, 2014, **136**, 2511–2519.
276 X. Ouyang, S.-J. Hwang, R. C. Runnebaum, D. Xie, Y.-J. Wanglee, T. Rea, S. I. Zones and A. Katz, *J. Am. Chem. Soc.*, 2014, **136**, 1449–1461.
277 P. Eliášová, M. Opanasenko, P. S. Wheatley, M. Shamzhy, M. Mazur, P. Nachtigall, W. J. Roth, R. E. Morris and J. Čejka, *Chem. Soc. Rev.*, 2015, **44**, 7177–7206.
278 S. A. Morris, G. P. M. Bignami, Y. Tian, M. Navarro, D. S. Firth, J. Čejka, P. S. Wheatley, D. M. Dawson, W. A. Slawinski, D. S. Wragg, R. E. Morris and S. E. Ashbrook, *Nat. Chem.*, 2017, **9**, 1012–1018.

279 D. S. Firth, S. A. Morris, P. S. Wheatley, S. E. Russell, A. M. Z. Slawin, D. M. Dawson, A. Mayoral, M. Opanasenko, M. Položij, J. Čejka, P. Nachtigall and R. E. Morris, *Chem. Mater.*, 2017, **29**, 5605–5611.
280 V. Kasneryk, M. Shamzhy, M. Opanasenko, P. S. Wheatley, S. A. Morris, S. E. Russell, A. Mayoral, M. Trachta, J. Čejka and R. E. Morris, *Angew. Chem. Int. Ed.*, 2017, **56**, 4324–4327.
281 P. Wolf, M. Valla, F. Núñez-Zarur, A. Comas-Vives, A. J. Rossini, C. Firth, H. Kallas, A. Lesage, L. Emsley, C. Copéret and I. Hermans, *ACS Catal.*, 2016, **6**, 4047–4063.
282 N. Nakazawa, T. Ikeda, N. Hiyoshi, Y. Yoshida, Q. Han, S. Inagaki and Y. Kubota, *J. Am. Chem. Soc.*, 2017, **139**, 7989–7997.
283 T. Ikuno, W. Chaikittisilp, Z. Liu, T. Iida, Y. Yanaba, T. Yoshikawa, S. Kohara, T. Wakihara and T. Okubo, *J. Am. Chem. Soc.*, 2015, **137**, 14533–14544.
284 L. Zhang, K. Chen, B. Chen, J. L. White and D. E. Resasco, *J. Am. Chem. Soc.*, 2015, **137**, 11810–11819.
285 S. Prodinger, M. A. Derewinski, A. Vjunov, S. D. Burton, I. Arslan and J. A. Lercher, *J. Am. Chem. Soc.*, 2016, **138**, 4408–4415.
286 A. Vjunov, J. L. Fulton, D. M. Camaioni, J. Z. Hu, S. D. Burton, I. Arslan and J. A. Lercher, *Chem. Mater.*, 2015, **27**, 3533–3545.
287 M. B. Park, N. H. Ahn, R. W. Broach, C. P. Nicholas, G. J. Lewis and S. B. Hong, *Chem. Mater.*, 2015, **27**, 1574–1582.
288 M. B. Park, D. Jo, H. C. Jeon, C. P. Nicholas, G. J. Lewis and S. B. Hong, *Chem. Mater.*, 2014, **26**, 6684–6694.
289 D. Zhou, X. Lu, J. Xu, A. Yu, J. Li, F. Deng and Q. Xia, *Chem. Mater.*, 2012, **24**, 4160–4165.
290 R. Baran, F. Averseng, Y. Millot, T. Onfroy, S. Casale and S. Dzwigaj, *J. Phys. Chem. C*, 2014, **118**, 4143–4150.
291 N. Popovych, P. Kyriienko, S. Soloviev, R. Baran, Y. Millot and S. Dzwigaj, *Phys. Chem. Chem. Phys.*, 2016, **18**, 29458–29465.
292 V. Rac, V. Rakić, D. Stošić, O. Otman and A. Auroux, *Microporous Mesoporous Mater.*, 2014, **194**, 126–134.
293 J. Van Aelst, M. Haouas, E. Gobechiya, K. Houthoofd, A. Philippaerts, S. P. Sree, C. E. A. Kirschhock, P. Jacobs, J. A. Martens, B. F. Sels and F. Taulelle, *J. Phys. Chem. C*, 2014, **118**, 22573–22582.
294 E. Dib, J. Grand, S. Mintova and C. Fernandez, *Chem. Mater.*, 2015, **27**, 7577–7579.
295 G. Brunklaus, H. Koller and S. I. Zones, *Angew. Chem. Int. Ed.*, 2016, **55**, 14459–14463.
296 E. Dib, T. Mineva, P. Gaveau, E. Véron, V. Sarou-Kanian, F. Fayon and B. Alonso, *J. Phys. Chem. C*, 2017, **121**, 15831–15841.
297 B. Zhang, Y. Zhang, Y. Hu, Z. Shi, A. Azhati, S. Xie, H. He and Y. Tang, *Chem. Mater.*, 2016, **28**, 2757–2767.
298 S. Cadars, M. Allix, D. H. Brouwer, R. Shayib, M. Suchomel, M. N. Garaga, A. Rakhmatullin, A. W. Burton, S. I. Zones, D. Massiot and B. F. Chmelka, *Chem. Mater.*, 2014, **26**, 6994–7008.
299 J. W. Harris, W.-C. Liao, J. R. Di Iorio, A. M. Henry, T.-C. Ong, A. Comas-Vives, C. Copéret and R. Gounder, *Chem. Mater.*, 2017, **29**, 8824–8837.
300 I. I. Ivanova, Y. G. Kolyagin, I. A. Kasyanov, A. V. Yakimov, T. O. Bok and D. N. Zarubin, *Angew. Chem. Int. Ed.*, 2017, **56**, 15344–15347.
301 M. D. Oleksiak, K. Muraoka, M.-F. Hsieh, M. T. Conato, A. Shimojima, T. Okubo, W. Chaikittisilp and J. D. Rimer, *Angew. Chem. Int. Ed.*, 2017, **56**, 13366–13371.

302 W. R. Gunther, V. K. Michaelis, R. G. Griffin and Y. Román-Leshkov, *J. Phys. Chem. C*, 2016, **120**, 28533–28544.
303 J. Z. Hu, C. Wan, A. Vjunov, M. Wang, Z. Zhao, M. Y. Hu, D. M. Camaioni and J. A. Lercher, *J. Phys. Chem. C*, 2017, **121**, 12849–12854.
304 K. A. Tarach, J. Martinez-Triguero, F. Rey and K. Góra-Marek, *J. Catal.*, 2016, **339**, 256–269.
305 Z. T. Lalowicz, G. Stoch, A. Birczyński, M. Punkkinen, E. E. Ylinen, M. Krzystyniak, K. Góra-Marek and J. Datka, *Solid State Nucl. Magn. Reson.*, 2012, **45**–**46**, 66–74.
306 G. Stoch, E. E. Ylinen, A. Birczynski, Z. T. Lalowicz, K. Góra-Marek and M. Punkkinen, *Solid State Nucl. Magn. Reson.*, 2013, **49**–**50**, 33–41.
307 A. M. Szymocha, A. Birczyński, Z. T. Lalowicz, G. Stoch, M. Krzystyniak and K. Góra-Marek, *J. Phys. Chem. A*, 2014, **118**, 5359–5370.
308 A. M. Szymocha, Z. T. Lalowicz, A. Birczyński, M. Krzystyniak, G. Stoch and K. Góra-Marek, *J. Phys. Chem. A*, 2014, **118**, 5371–5380.
309 Z. T. Lalowicz, A. Birczyński and A. Krzyżak, *J. Phys. Chem. C*, 2017, **121**, 26472–26482.
310 C. Wang, Y. Chu, A. Zheng, J. Xu, Q. Wang, P. Gao, G. Qi, Y. Gong and F. Deng, *Chem. Eur. J.,* 2014, **20**, 12432–12443.
311 M. E. Potter, A. J. O'Malley, S. Chapman, J. Kezina, S. H. Newland, I. P. Silverwood, S. Mukhopadhyay, M. Carravetta, T. M. Mezza, S. F. Parker, C. R. A. Catlow and R. Raja, *ACS Catal.*, 2017, **7**, 2926–2934.
312 J. Dijkmans, M. Dusselier, D. Gabriëls, K. Houthoofd, P. C. M. M. Magusin, S. Huang, Y. Pontikes, M. Trekels, A. Vantomme, L. Giebeler, S. Oswald and B. F. Sels, *ACS Catal.*, 2015, **5**, 928–940.
313 B. Tang, W. Dai, G. Wu, N. Guan, L. Li and M. Hunger, *ACS Catal.*, 2014, **4**, 2801–2810.
314 S. Lang, M. Benz, U. Obenaus, R. Himmelmann and M. Hunger, *ChemCatChem*, 2016, **8**, 2031–2036.
315 W. Dai, C. Wang, X. Yi, A. Zheng, L. Li, G. Wu, N. Guan, Z. Xie, M. Dyballa and M. Hunger, *Angew. Chem. Int. Ed.*, 2015, **54**, 8783–8786.
316 Z. Zhao, H. Shi, C. Wan, M. Y. Hu, Y. Liu, D. Mei, D. M. Camaioni, J. Z. Hu and J. A. Lercher, *J. Am. Chem. Soc.*, 2017, **139**, 9178–9185.
317 S. Radhakrishnan, P.-J. Goossens, P. C. M. M. Magusin, S. P. Sree, C. Detavernier, E. Breynaert, C. Martineau, F. Taulelle and J. A. Martens, *J. Am. Chem. Soc.*, 2016, **138**, 2802–2808.
318 M. Moreno-González, B. Hueso, M. Boronat, T. Blasco and A. Corma, *J. Phys. Chem. Lett.*, 2015, **6**, 1011–1017.
319 C. Paolucci, A. A. Parekh, I. Khurana, J. R. Di Iorio, H. Li, J. D. Albarracin Caballero, A. J. Shih, T. Anggara, W. N. Delgass, J. T. Miller, F. H. Ribeiro, R. Gounder and W. F. Schneider, *J. Am. Chem. Soc.*, 2016, **138**, 6028–6048.
320 S. Bordiga, C. Lamberti, F. Bonino, A. Travert and F. Thibault-Starzyk, *Chem. Soc. Rev.*, 2015, **44**, 7262–7341.
321 B. C. Knott, C. T. Nimlos, D. J. Robichaud, M. R. Nimlos, S. Kim and R. Gounder, *ACS Catal.*, 2018, **8**, 770–784.
322 P. Concepción, M. Boronat, R. Millán, M. Moliner and A. Corma, *Top. Catal.*, 2017, **60**, 1653–1663.
323 T. C. Keller, M. Položij, B. Puértolas, H. V. Thang, P. Nachtigall and J. Pérez-Ramírez, *J. Phys. Chem. C*, 2016, **120**, 4954–4960.
324 I. Voleská, P. Nachtigall, E. Ivanova, K. Hadjiivanov and R. Bulánek, *Catal. Today*, 2015, **243**, 53–61.

325 A. Mikuła, M. Król, W. Mozgawa and A. Koleżyński, *Spectrochim. Acta. A. Mol. Biomol. Spectrosc.*, 2018, **195**, 62–67.
326 M. Król, W. Mozgawa and W. Jastrzębski, *J. Porous Mater.*, 2016, **23**, 1–9.
327 M. Rubeš, E. Koudelková, F. S. de Oliveira Ramos, M. Trachta, O. Bludský and R. Bulánek, *J. Phys. Chem. C*, 2018, **122**, 6128–6136.
328 G. J. Gomes, M. F. Zalazar, C. A. Lindino, F. R. Scremin, P. R. S. Bittencourt, M. B. Costa and N. M. Peruchena, *Microporous Mesoporous Mater.*, 2017, **252**, 17–28.
329 S. C. Mohan, R. Vijay Solomon, P. Venuvanalingam and K. Jothivenkatachalam, *New J. Chem.*, 2017, **41**, 9505–9512.
330 L. Gigli, R. Arletti, G. Tabacchi, M. Fabbiani, J. G. Vitillo, G. Martra, A. Devaux, I. Miletto, S. Quartieri, G. Calzaferri and E. Fois, *J. Phys. Chem. C*, 2018, **122**, 3401–3418.
331 S. R. Whittleton, A. Vicente, C. Fernandez, S. F. Rastegar, A. V. Fishchuk and S. Sklenak, *Microporous Mesoporous Mater.*, 2018, **267**, 124–133.
332 E. Dib, M. Freire, V. Pralong, T. Mineva and B. Alonso, *Acta Crystallogr. Sect. C Struct. Chem.*, 2017, **73**, 202–207.
333 M. Haouas, F. Taulelle and C. Martineau, *Prog. Nucl. Magn. Reson. Spectrosc.*, 2016, **94–95**, 11–36.
334 S. T. Wilson, B. M. Lok, C. A. Messina, T. R. Cannan and E. M. Flanigen, *J. Am. Chem. Soc.*, 1982, **104**, 1146–1147.
335 M. Hartmann and L. Kevan, *Chem. Rev.*, 1999, **99**, 635–664.
336 P. Tian, Y. Wei, M. Ye and Z. Liu, *ACS Catal.*, 2015, **5**, 1922–1938.
337 H. O. Pastore, S. Coluccia and L. Marchese, *Annu. Rev. Mater. Res.*, 2005, **35**, 351–395.
338 J. Chen, P. A. Wright, J. M. Thomas, S. Natarajan, L. Marchese, S. M. Bradley, G. Sankar, C. R. A. Catlow and P. L. Gai-Boyes, *J. Phys. Chem.*, 1994, **98**, 10216–10224.
339 M. A. Makarova, A. F. Ojo, K. Karim, M. Hunger and J. Dwyer, *J. Phys. Chem.*, 1994, **98**, 3619–3623.
340 H. Knözinger and S. Huber, *J. Chem. Soc. Faraday Trans.*, 1998, **94**, 2047–2059.
341 S. Coluccia, L. Marchese and G. Martra, *Microporous Mesoporous Mater.*, 1999, **30**, 43–56.
342 G. A. V. Martins, G. Berlier, S. Coluccia, H. O. Pastore, G. B. Superti, G. Gatti and L. Marchese, *J. Phys. Chem. C*, 2007, **111**, 330–339.
343 G. V. A. Martins, G. Berlier, C. Bisio, S. Coluccia, H. O. Pastore and L. Marchese, *J. Phys. Chem. C*, 2008, **112**, 7193–7200.
344 S. Bordiga, L. Regli, D. Cocina, C. Lamberti, M. Bjørgen and K. P. Lillerud, *J. Phys. Chem. B*, 2005, **109**, 2779–2784.
345 Z. Qu, Y. Li, S. Huang, P. Chen and X. Ma, *Sci. China Chem.*, 2017, **60**, 912–919.
346 Y. Li, J. Deng, W. Song, J. Liu, Z. Zhao, M. Gao, Y. Wei and L. Zhao, *J. Phys. Chem. C*, 2016, **120**, 14669–14680.
347 B. Alonso and C. Marichal, *Chem. Soc. Rev.*, 2013, **42**, 3808–3820.
348 D. Zhao, J. Feng, Q. Huo, N. A. Melosh, G. H. Fredrickson, B. F. Chmelka and G. D. Stucky, *Science*, 1998, **279**, 548–552.
349 D. Zhao, Q. Huo, J. Feng, B. F. Chmelka and G. D. Stucky, *J. Am. Chem. Soc.*, 1998, **120**, 6024–6036.
350 F. Carniato, G. Paul, C. Bisio, S. Caldarelli and L. Marchese, *RSC Adv.*, 2012, **2**, 1153–1160.
351 G. Paul, S. Steuernagel and H. Koller, *Chem. Commun.*, 2007, 5194–5196.
352 T. Yasmin and K. Müller, *Microporous Mesoporous Mater.*, 2015, **208**, 83–92.

353 A. S. Cattaneo, C. Ferrara, D. C. Villa, S. Angioni, C. Milanese, D. Capsoni, S. Grandi, P. Mustarelli, V. Allodi, G. Mariotto, S. Brutti and E. Quartarone, *Microporous Mesoporous Mater.*, 2016, **219**, 219–229.
354 L. M. Reid and C. M. Crudden, *Chem. Mater.*, 2016, **28**, 7605–7612.
355 M. W. A. MacLean, T. K. Wood, G. Wu, R. P. Lemieux and C. M. Crudden, *Chem. Mater.*, 2014, **26**, 5852–5859.
356 A. Azhati, S. Xie, W. Wang, A. A. Elzatahry, Y. Yan, J. Zhou, D. Al-Dhayan, Y. Zhang, Y. Tang and D. Zhao, *Chem. Mater.*, 2016, **28**, 4859–4866.
357 J. Walia, J. Crone, J. Liang, M. Niknam, C. Lemaire, R. Terry Thompson and H. Peemoeller, *Solid State Nucl. Magn. Reson.*, 2013, **49**–**50**, 26–32.
358 M. Niknam, J. Liang, J. Walia and H. Peemoeller, *Microporous Mesoporous Mater.*, 2012, **162**, 136–142.
359 B. Grünberg, A. Grünberg, H.-H. Limbach and G. Buntkowsky, *Appl. Magn. Reson.*, 2013, **44**, 189–201.
360 N. H. N. Kamarudin, A. A. Jalil, S. Triwahyono, M. R. Sazegar, S. Hamdan, S. Baba and A. Ahmad, *RSC Adv.*, 2015, **5**, 30023–30031.
361 P. Bhanja, A. Modak, S. Chatterjee and A. Bhaumik, *ACS Sustain. Chem. Eng.*, 2017, **5**, 2763–2773.
362 S. Ok, D. W. Hoyt, A. Andersen, J. Sheets, S. A. Welch, D. R. Cole, K. T. Mueller and N. M. Washton, *Langmuir*, 2017, **33**, 1359–1367.
363 K. P. Nartowski, D. Malhotra, L. E. Hawarden, J. Sibik, D. Iuga, J. A. Zeitler, L. Fábián and Y. Z. Khimyak, *Angew. Chem. Int. Ed.*, 2016, **55**, 8904–8908.
364 F. Tielens, N. Folliet, L. Bondaz, S. Etemovic, F. Babonneau, C. Gervais and T. Azaïs, *J. Phys. Chem. C*, 2017, **121**, 17339–17347.
365 T. Azaïs, G. Laurent, K. Panesar, A. Nossov, F. Guenneau, C. Sanfeliu Cano, C. Tourné-Péteilh, J.-M. Devoisselle and F. Babonneau, *J. Phys. Chem. C*, 2017, **121**, 26833–26839.
366 S. Jayanthi, S. Kababya, A. Schmidt and S. Vega, *J. Phys. Chem. C*, 2016, **120**, 2797–2806.
367 M. Barczak, M. Wierzbicka and P. Borowski, *Microporous Mesoporous Mater.*, 2018, **264**, 254–264.
368 I. del Hierro, Y. Pérez, P. Cruz and R. Juárez, *Eur. J. Inorg. Chem.*, 2017, **2017**, 3030–3039.
369 A. Kiwilsza, B. Milanowski, K. Drużbicki, L. E. Coy, M. Grzeszkowiak, M. Jarek, J. Mielcarek, J. Lulek, A. Pajzderska and J. Wąsicki, *J. Porous Mater.*, 2015, **22**, 817–829.
370 L. Mafra, T. Čendak, S. Schneider, P. V. Wiper, J. Pires, J. R. B. Gomes and M. L. Pinto, *J. Am. Chem. Soc.*, 2017, **139**, 389–408.
371 G. Gatti, D. Costenaro, C. Vittoni, G. Paul, V. Crocellà, E. Mangano, S. Brandani, S. Bordiga, M. Cossi, L. Marchese and C. Bisio, *Phys. Chem. Chem. Phys.*, 2017, **19**, 14114–14128.
372 G. Gatti, C. Vittoni, D. Costenaro, G. Paul, E. Mangano, S. Brandani, L. Marchese and C. Bisio, *Phys. Chem. Chem. Phys.*, 2017, **19**, 29449–29460.
373 D. Massiot, F. Fayon, M. Capron, I. King, S. Le Calvé, B. Alonso, J.-O. Durand, B. Bujoli, Z. Gan and G. Hoatson, *Magn. Reson. Chem.*, 2002, **40**, 70–76.
374 F. Bauer, S. Czihal, M. Bertmer, U. Decker, S. Naumov, S. Wassersleben and D. Enke, *Microporous Mesoporous Mater.*, 2017, **250**, 221–231.
375 S. A. Didas, R. Zhu, N. A. Brunelli, D. S. Sholl and C. W. Jones, *J. Phys. Chem. C*, 2014, **118**, 12302–12311.

376 N. Carlsson, H. Gustafsson, C. Thörn, L. Olsson, K. Holmberg and B. Åkerman, *Adv. Colloid Interface Sci.*, 2014, **205**, 339–360.
377 T. Siodla, I. Sobczak, M. Ziolek and F. Tielens, *Microporous Mesoporous Mater.*, 2018, **256**, 199–205.
378 S. Kwon, H. J. Kwon, J. I. Choi, K. C. Kim, J. G. Seo, J. E. Park, S. J. You, E. D. Park, S. S. Jang and H. C. Lee, *ACS Appl. Mater. Interfaces*, 2017, **9**, 31683–31690.
379 Y. Liu, F. Liu, G. Ye, N. Pu, F. Wu, Z. Wang, X. Huo, J. Xu and J. Chen, *Dalton Trans.*, 2016, **45**, 16492–16504.
380 G. Paul, G. E. Musso, E. Bottinelli, M. Cossi, L. Marchese and G. Berlier, *ChemPhysChem*, 2017, **18**, 839–849.
381 A. S. Andreev and V. Livadaris, *J. Phys. Chem. C*, 2017, **121**, 14108–14119.
382 M. F. Harrach, B. Drossel, W. Winschel, T. Gutmann and G. Buntkowsky, *J. Phys. Chem. C*, 2015, **119**, 28961–28969.
383 B. Martins Estevão, F. Cucinotta, N. Hioka, M. Cossi, M. Argeri, G. Paul, L. Marchese and E. Gianotti, *Phys. Chem. Chem. Phys.*, 2015, **17**, 26804–26812.
384 E. Gianotti, B. Martins Estevão, F. Cucinotta, N. Hioka, M. Rizzi, F. Renò and L. Marchese, *Chem. Eur. J.,* 2014, **20**, 10921–10925.
385 A. Comotti, S. Bracco and P. Sozzani, *Acc. Chem. Res.*, 2016, **49**, 1701–1710.
386 S. Bracco, A. Comotti, P. Valsesia, B. F. Chmelka and P. Sozzani, *Chem. Commun.*, 2008, 4798–4800.
387 S. Bracco, M. Beretta, A. Cattaneo, A. Comotti, A. Falqui, K. Zhao, C. Rogers and P. Sozzani, *Angew. Chem. Int. Ed.*, 2015, **54**, 4773–4777.
388 E. Weiland, M.-A. Springuel-Huet, A. Nossov and A. Gédéon, *Microporous Mesoporous Mater.*, 2016, **225**, 41–65.
389 K. Bärwinkel, M. M. Herling, M. Rieß, H. Sato, L. Li, Y. S. Avadhut, T. W. Kemnitzer, H. Kalo, J. Senker, R. Matsuda, S. Kitagawa and J. Breu, *J. Am. Chem. Soc.*, 2017, **139**, 904–909.
390 L. R. Becerra, G. J. Gerfen, R. J. Temkin, D. J. Singel and R. G. Griffin, *Phys. Rev. Lett.*, 1993, **71**, 3561–3564.
391 A. J. Rossini, A. Zagdoun, M. Lelli, A. Lesage, C. Copéret and L. Emsley, *Acc. Chem. Res.*, 2013, **46**, 1942–1951.
392 A. S. Lilly Thankamony, J. J. Wittmann, M. Kaushik and B. Corzilius, *Prog. Nucl. Magn. Reson. Spectrosc.*, 2017, **102**–**103**, 120–195.
393 D. Lee, S. Hediger and G. De Paëpe, *Solid State Nucl. Magn. Reson.*, 2015, **66**–**67**, 6–20.
394 M. Rosay, M. Blank and F. Engelke, *J. Magn. Reson.*, 2016, **264**, 88–98.
395 W. R. Grüning, A. J. Rossini, A. Zagdoun, D. Gajan, A. Lesage, L. Emsley and C. Copéret, *Phys. Chem. Chem. Phys.*, 2013, **15**, 13270–13274.
396 O. Lafon, A. S. L. Thankamony, T. Kobayashi, D. Carnevale, V. Vitzthum, I. I. Slowing, K. Kandel, H. Vezin, J.-P. Amoureux, G. Bodenhausen and M. Pruski, *J. Phys. Chem. C*, 2013, **117**, 1375–1382.
397 O. Lafon, M. Rosay, F. Aussenac, X. Lu, J. Trébosc, O. Cristini, C. Kinowski, N. Touati, H. Vezin and J.-P. Amoureux, *Angew. Chem. Int. Ed.*, 2011, **50**, 8367–8370.
398 T. Kobayashi, O. Lafon, A. S. Lilly Thankamony, I. I. Slowing, K. Kandel, D. Carnevale, V. Vitzthum, H. Vezin, J.-P. Amoureux, G. Bodenhausen and M. Pruski, *Phys. Chem. Chem. Phys.*, 2013, **15**, 5553–5562.
399 T. Kobayashi, D. Singappuli-Arachchige, Z. Wang, I. I. Slowing and M. Pruski, *Phys. Chem. Chem. Phys.*, 2017, **19**, 1781–1789.

400 P. Wolf, M. Valla, A. J. Rossini, A. Comas-Vives, F. Núñez-Zarur, B. Malaman, A. Lesage, L. Emsley, C. Copéret and I. Hermans, *Angew. Chem. Int. Ed.*, 2014, **53**, 10179–10183.
401 C. Copéret, W.-C. Liao, C. P. Gordon and T.-C. Ong, *J. Am. Chem. Soc.*, 2017, **139**, 10588–10596.
402 W. R. Gunther, V. K. Michaelis, M. A. Caporini, R. G. Griffin and Y. Román-Leshkov, *J. Am. Chem. Soc.*, 2014, **136**, 6219–6222.
403 D. P. Serrano, J. M. Escola and P. Pizarro, *Chem. Soc. Rev.*, 2013, **42**, 4004–4035.
404 J. Shi, Y. Wang, W. Yang, Y. Tang and Z. Xie, *Chem. Soc. Rev.*, 2015, **44**, 8877–8903.
405 M. Hartmann and W. Schwieger, *Chem. Soc. Rev.*, 2016, **45**, 3311–3312.
406 J. Pérez-Ramírez, C. H. Christensen, K. Egeblad, C. H. Christensen and J. C. Groen, *Chem. Soc. Rev.*, 2008, **37**, 2530–2542.
407 M. S. Holm, E. Taarning, K. Egeblad and C. H. Christensen, *Catal. Today*, 2011, **168**, 3–16.
408 M.-H. Sun, S.-Z. Huang, L.-H. Chen, Y. Li, X.-Y. Yang, Z.-Y. Yuan and B.-L. Su, *Chem. Soc. Rev.*, 2016, **45**, 3479–3563.
409 S. Mitchell, A. B. Pinar, J. Kenvin, P. Crivelli, J. Kärger and J. Pérez-Ramírez, *Nat. Commun.*, 2015, **6**, 8633.
410 K. Góra-Marek, K. Tarach, J. Tekla, Z. Olejniczak, P. Kuśtrowski, L. Liu, J. Martinez-Triguero and F. Rey, *J. Phys. Chem. C*, 2014, **118**, 28043–28054.
411 J. C. Groen, L. A. A. Peffer, J. A. Moulijn and J. Pérez-Ramírez, *Chem. Eur. J.,* 2005, **11**, 4983–4994.
412 E. Gianotti, M. Manzoli, M. E. Potter, V. N. Shetti, D. Sun, J. Paterson, T. M. Mezza, A. Levy and R. Raja, *Chem. Sci.*, 2014, **5**, 1810–1819.
413 J. Li, M. Liu, X. Guo, S. Xu, Y. Wei, Z. Liu and C. Song, *ACS Appl. Mater. Interfaces*, 2017, **9**, 26096–26106.
414 D. Verboekend, M. Milina and J. Pérez-Ramírez, *Chem. Mater.*, 2014, **26**, 4552–4562.
415 A. Sachse and J. García-Martínez, *Chem. Mater.*, 2017, **29**, 3827–3853.
416 X. Zhu, J. P. Hofmann, B. Mezari, N. Kosinov, L. Wu, Q. Qian, B. M. Weckhuysen, S. Asahina, J. Ruiz-Martínez and E. J. M. Hensen, *ACS Catal.*, 2016, **6**, 2163–2177.
417 A. J. Cramer and J. M. Cole, *J. Mater. Chem. A*, 2017, **5**, 10746–10771.
418 S. Blasioli, A. Martucci, G. Paul, L. Gigli, M. Cossi, C. T. Johnston, L. Marchese and I. Braschi, *J. Colloid Interface Sci.*, 2014, **419**, 148–159.
419 I. Braschi, A. Martucci, S. Blasioli, L. L. Mzini, C. Ciavatta and M. Cossi, *Chemosphere*, 2016, **155**, 444–452.
420 V. Sacchetto, G. Gatti, G. Paul, I. Braschi, G. Berlier, M. Cossi, L. Marchese, R. Bagatin and C. Bisio, *Phys. Chem. Chem. Phys.*, 2013, **15**, 13275–13287.
421 G. Gatti, D. F. Olivas Olivera, V. Sacchetto, M. Cossi, I. Braschi, L. Marchese and C. Bisio, *ChemPhysChem*, 2017, **18**, 2374–2380.
422 V. Sacchetto, D. F. Olivas Olivera, G. Paul, G. Gatti, I. Braschi, L. Marchese and C. Bisio, *J. Phys. Chem. C*, 2017, **121**, 6081–6089.
423 L. Gigli, R. Arletti, G. Tabacchi, E. Fois, J. G. Vitillo, G. Martra, G. Agostini, S. Quartieri and G. Vezzalini, *J. Phys. Chem. C*, 2014, **118**, 15732–15743.
424 M. Bouchoucha, F. Tielens, F. Gaslain, F. CostaTorro, S. Casale, A. Palcic, V. Valtchev, J.-F. Lambert and M. Jaber, *J. Phys. Chem. C*, 2015, **119**, 8736–8747.
425 C. Song, Y. Chu, M. Wang, H. Shi, L. Zhao, X. Guo, W. Yang, J. Shen, N. Xue, L. Peng and W. Ding, *J. Catal.*, 2017, **349**, 163–174.
426 W. Dai, X. Sun, B. Tang, G. Wu, L. Li, N. Guan and M. Hunger, *J. Catal.*, 2014, **314**, 10–20.

427 M. Huang, Q. Wang, X. Yi, Y. Chu, W. Dai, L. Li, A. Zheng and F. Deng, *Chem. Commun.*, 2016, **52**, 10606–10608.
428 S. Zhang, M. Cui, Y. Zhang, Y. Mu, T. Lv, J. Zheng, J. Zhao, X. Liu and C. Meng, *Microporous Mesoporous Mater.*, 2017, **244**, 158–163.
429 S. Zhang, M. Cui, Y. Zhang, J. Zheng, T. Lv, W. Gao, X. Liu and C. Meng, *J. Alloys Compd.*, 2017, **696**, 788–794.